Title

Numerical Algorithms based on the Immersed Boundary Method for Modeling the Dynamics of Semiflexible Filaments and the Mechanics of Actin Cortex

Author

Ntetsika, Magdalini

Publication Date

2021

Peer reviewed|Thesis/dissertation

Numerical Algorithms based on the Immersed Boundary Method for Modeling the Dynamics of Semiflexible Filaments and the Mechanics of Actin Cortex

by

Magdalini Ntetsika

A dissertation submitted in partial satisfaction of the
requirements for the degree of
Doctor of Philosophy

in

Engineering - Mechanical Engineering

in the

GRADUATE DIVISION
of the
UNIVERSITY OF CALIFORNIA, BERKELEY

Committee in charge:
Professor Panayiotis Papadopoulos, Chair
Professor James Casey
Professor Filip C. Filippou

Spring 2021

Numerical Algorithms based on the Immersed Boundary Method
for Modeling the Dynamics of Semiflexible Filaments
and the Mechanics of Actin Cortex

Abstract

Numerical Algorithms based on the Immersed Boundary Method
for Modeling the Dynamics of Semiflexible Filaments
and the Mechanics of Actin Cortex

by

Magdalini Ntetsika
Doctor of Philosophy in Engineering - Mechanical Engineering

University of California, Berkeley

Professor Panayiotis Papadopoulos, Chair

The mechanical behavior of cortical actin cytoskeleton, a network of cross-linked semiflexible actin filaments (F-actin), is of interest to biologists and engineers since it plays a key role in many fundamental cellular properties and processes, such as cell shape and motility. The dynamics of flexible filaments in low-Reynolds number viscous shear flow has also gained much interest in the last decades in a wide variety of applications involving biological systems like DNA, polymers and proteins. In this dissertation, two numerical algorithms based on the Immersed Boundary Method (IBM) are proposed and implemented for the study of the actin cortex and the dynamics of semiflexible filaments immersed in low-Reynolds flows.

A new, modified, and more computationally efficient version of the IBM that combines the Coarse-Graining Method (CGM) with IBM is developed for modeling of inextensible filaments in shear flow at low Reynolds numbers. The various two-dimensional orbit regimes of flexible filaments are studied and the results of the proposed method are validated with theoretical results and previous works, numerical and experimental, showing excellent agreement. They are subsequently used to develop a prediction model using Artificial Neural Networks (ANN) to effectively forecast the orbit regime of a filament in shear flow with different parameters.

An extension of the traditional IBM to include a stochastic stress tensor is also proposed in order to model the thermal fluctuations in the cytoplasmic fluid surrounding the actin cortex. The theoretical values for time-averaged contraction for a single inextensible filament under hydrodynamic thermal fluctuations are verified through numerical simulation. The mechanical behavior of the actin cortex and its elasticity when subjected to shear flow is investigated, illustrating a stiffening of the cross-linked network with increasing strain under shear flow, as other experimental and numerical studies have shown. By implementing the proposed extension of the IBM, the behavior and interaction of passive F-actin under thermal fluctuations is also studied in the current work, where a trend of filaments to spread out is observed.

To my parents, Lambrini and Lambros,
to Kostas,
to Matina and Konstantinos.

Contents

List of Figures

List of Tables

List of Algorithms

Acknowledgments

I would like to express my deep sense of thanks and gratitude to my advisor Professor Panos Papadopoulos. His deep understanding, clarity and presentation of Computational Mechanics motivated me to become his student and I have been very fortunate to have him as advisor and mentor. He was always supportive of my research ideas and I truly enjoyed working in a research environment that stimulates original thinking and initiative, which he created. He is a role model for me and I learned so much from his example and his qualities of rigorousness and clarity in solving research problems. Without his immense knowledge, attention to the detail and guidance I would not be able to complete my doctoral work.

I would like to thank deeply Professor Filip C. Filippou. Without his valuable help, my entrance to UC Berkeley would not be possible. I would also like to thank him for his very much appreciated comments and feedback regarding this thesis. I would like to thank Professor James Casey as well for his feedback on this thesis and for always being supportive. I would also like to thank Professor Kranthi Mandadapu from the Department of Chemical and Biomolecular Engineering for the long and useful discussions.

My doctoral work would not be possible without the constant support of my parents, my partner, and my siblings. I am grateful to my parents, Lambros and Lambrini, for always being supportive and always teaching me by their example. They are the most loving parents I can imagine and without them I would not be here today. I would like to thank my partner Kostas for his love, support and for always being there for me. With his clarity of mind he helped me navigate through some of the most difficult moments I've experienced in this journey. Lastly, I would like to thank my siblings, Matina and Konstantinos, for being the best friends I could ever ask for and for always being there for discussing all the problems I had during my Ph.D. journey.

Chapter 1

Introduction

1.1 Motivation and prior works

Cell mechanics is key to many cellular properties and processes, such as cell shape, cell motility and cell division and is also an important biomarker for probing the cell's pathological changes. Living cells display a high degree of internal mechanical and functional organization and their intracellular biopolymer scaffold, the cytoskeleton, plays a key role in that [1]. The cytoskeleton is a very dynamic and complex system far from thermodynamic equilibrium, enabling rapid adaptive organization. It is made up of three types of polymers: microtubules, actin filaments, and intermediate filaments, which are cross-linked in a network distributed throughout the cytoplasm. Microtubules, the stiffest of the three polymers, are hollow rods approximately 25 nm in diameter [1]. Actin filaments are linear polymers of globular actin subunits. They are much less stiff than microtubules, with a diameter of approximately 9 nm, however the presence of high concentrations of myosin [1], a motor protein that acts as cross-linker that binds to actin filaments, promotes the assembly of highly organized, stiff networks [2]. Intermediate filaments lie in diameter between microtubules and F-actin, and depending on the type, they have a roughly cylindrical shape about 10 nm in diameter. Although the fundamental building blocks are almost the same in every animal cell, their cytoskeleton-induced morphology differs substantially [3]. Even within single cells, the cytoskeleton organizes locally into many different structures. Therefore, the cytoskeleton's ability to organize is at the same time challenging and fascinating and lies at the heart of the structural and functional organization of living matter.

The actin cortex is the part of the cytoskeleton attached to the cell membrane in most eukaryotic cells, *i.e.* cells with clearly defined nucleus. The cortical actin cytoskeleton plays a fundamental role in cell shape, which is maintained through structural stiffness and rheology. Actin cortex, as shown in Figures 1.1 and 1.2, is a thin actomyosin network that underlies the plasma membrane, consisting of actin filaments cross-linked by actin-binding proteins and containing motor proteins that

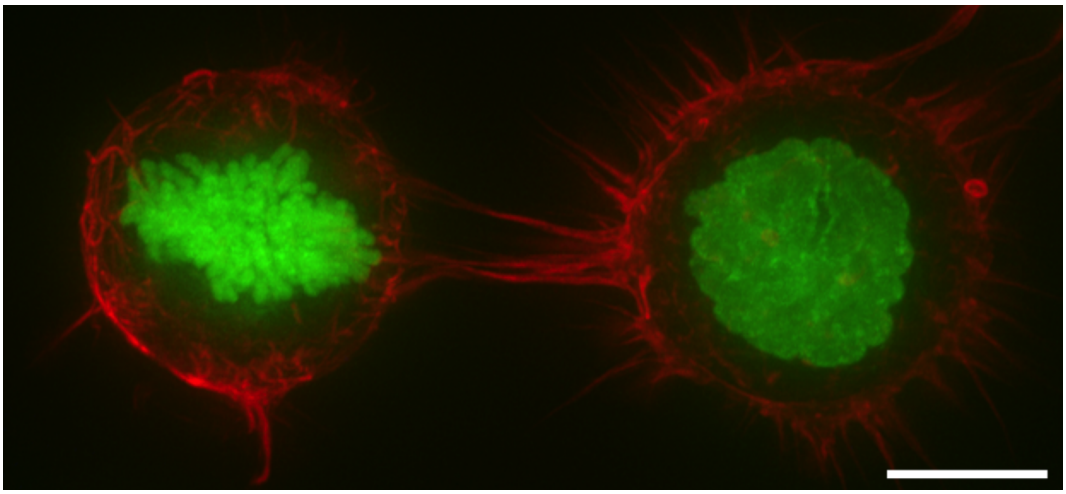

Figure 1.1: *F-actin distribution in the cell cortex [4]. F-actin is red, while Histone H2B is displayed in green. The left hand cell is in mitosis, as demonstrated by chromosome condensation, while the right hand cell is in interphase (as determined by intact cell nucleus) in a suspended state. In both cases F-actin is enriched around the cell periphery. Scale bar:* 10 μm.

generate stress within the network [5]. In order for the actin filaments to become cross-linked, they undergo thermal fluctuations to find a cross-linking partner and when cross-links between actin filaments are formed, the amplitudes of filament fluctuations are reduced, supporting the formation of additional cross-links [6]. Therefore, the degree of cross-linking in the final network is obviously dependent on the density of cross-linkers, as well as the way filaments interact with each other and the thermal noise.

Actin filaments are biopolymers with contour length long enough so that they may exhibit significant thermal bending fluctuations, in the order of approximately 1% of their contour length. However, their diameter can be as large as ten nanometers or more, giving them noteworthy bending rigidity. Thus, actin filaments are said to be semiflexible in the sense that their bending stiffness is large enough, such that the bending energetics - that favors a straight conformation - can just out-compete the entropic tendency of a chain to crumple up into a random coil [8]. Therefore, semiflexible polymers exhibit small, yet significant, thermal fluctuations around a straight conformation.

The competition between entropic and energetic effects in semiflexible polymers gives rise to many physical properties and the semiflexible nature of the actin filaments also has major implications on how they interact with each other to form cross-linked networks [9, 10]. Actin filaments are often effectively modeled as inextensible elastic fibers with finite resistance to bending, according to the so-called worm-like-chain (WLC) model introduced by Kratky and Porod [11]. More specifically, a single actin

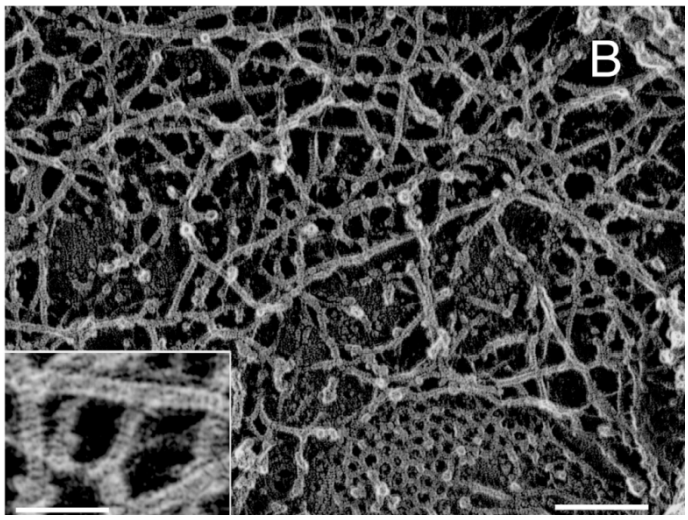

Figure 1.2: *Electron tomography image of the cytoskeletal cortex, [7]. Scale bar,* 10 *nm, inset scale bar,* 50 *nm.*

filament can respond to forces applied to it by bending, stretching or compressing, as well as to the entropy through thermal bending fluctuations. The axial force required to extend the filament is calculated in terms of a so-called force-extension relationship, which describes the longitudinal response of a single filament under entropic resistance to such extension due to the presence of thermal fluctuations that make the polymer deviate from a straight conformation. Since there are many more crumpled configurations of the polymer than the (unique) straight conformation, extending the polymer reduces the entropy and may increase the free energy. This entropic force-extension has been the basis of mechanical studies, for example, of long DNA [12].

There has been deep interest in studying the mechanical response of biological tissues the past decades, and more specifically, in understanding the mechanical properties of biopolymer networks, since they play an important role in cell motility [13, 14], the spontaneous movement of a cell from one location to another by consumption of energy, and mechanotransduction [15–17], the various mechanisms by which cells convert mechanical stimulus into electrochemical activity. Since the elasticity of eukaryotic cells and their motility is governed by the actin cortex, understanding the mechanical properties of the actin cortex is crucial for gaining insight into fundamental phenomena. Therefore, over the last few years significant work has been done in modeling the actin filaments and the cross-linked networks they form, taking also into consideration the filament-fluid interactions and the thermal noise, as done by du Roure *et al.* [18].

The major determinants of cortical mechanics are the density and lengths of the actin filaments, as well as the geometry and architecture of the network and the

density of the cross-links that bundle the actin filaments together. Experimental, as well as theoretical and numerical studies have shown that cross-linked biopolymer networks, when subjected to shear, stiffen at increasing strain [19–21]. These observations are supported by recent finite element studies of Onck [22] and Wilhelp and Frey [23]. However, in [22], apart from an initially undulated state of the filaments, the dynamic-thermal interaction of the filaments with the surrounding (cytoplasmic) fluid is completely ignored. The presence of the surrounding fluid is not taken into consideration in the computations, hence the interaction between fluid and actin filaments is ignored alltogether. Similarly in [23], even though the thermal interactions are taken into account in that study, the effect of the surrounding fluid and the two-way coupling between fluid and filaments are again completely ignored.

The investigation of the behavior of semiflexible filaments in viscous shear flows at low Reynolds numbers has also gained very much interest in the last decades, due to the relevance of its applications in areas involving biological systems like DNA [24,25], polymers [27] and proteins, but also in areas such as biotechnology that involve natural and synthetic fibers [26]. These fluid-structure interaction (FSI) problems are quite challenging because of the complex interplay of the hydrodynamic stresses with the corresponding fiber conformity, however, a two-way interaction between the immersed filaments and the surrounding fluid is important for gaining a better understanding of the underlying physical behavior.

Experimental, numerical and theoretical studies have also been conducted by researchers to study filaments in viscous shear flows. As early as 1922, Jeffery [28] studied the motion of a single rigid, neutrally buoyant, elliptical particle in a Couette flow, and, together with the experimental studies of Forgacs and Mason [29], enabled an initial understanding of the filament motion in background shear flow. Yamamoto and Matsuoka [30] proposed a method for simulating the dynamic behavior of rigid and flexible fibers in a flow field, with the fibers regarded as made up of spheres that are lined up and bonded to each neighbor. Tornberg and Shelley [31] studied the dynamics of slender filaments suspended in Stokesian fluids employing a non-local slender body theory. In most of these studies, the hydrodynamic interaction was neglected, therefore, there was limited information about the underlying FSI. The fluid was considered as a passive medium and coupling between fluid and structure was one-way.

The IBM of Peskin [32], which accounts for the two-way interaction between filament and fluid, has gained substantial popularity the past years in studying the dynamics of filaments in flow fields. Stockie [33] employed the IBM to simulated a single three-dimensional wood pulp fiber in shear flow which was an extension of the previously developed two-dimensional model in [34]. The two-dimensional orbit classes for flexible filaments placed in shear flow were successfully recreated by Kanchan and Maniyer [27], as well as by Wiens and Stockie [35], where the fiber was modeled as a Kirchhoff rod and a pseudo-compressible fluid solver was used for the simulation.

In most of these studies, where the dynamics of semiflexible inextensible filaments in viscous shear flow were studied, a very high stretching stiffness had to be used for the filaments with the IBM to approximate inextensibility, which significantly restricted the time step, increasing substantially the computational cost. Wiens and Stockie [35] used a generalized IB method which can be viewed as a type of penalty method in which the rod is only approximately inextensible. Similarly, Huang *et al.* [36] used a modified IBM with an extra inextensibility condition to strictly enforce the filament inextensibility. In practice, however, this inextensibility condition is prone to numerical errors [36] causing the filament length to vary over time. Another way, more straightforward and faster computationally, for dealing with the inextensibility of semiflexible filaments is to use the Coarse-Graining Method (CGM) [37]. This uses discrete models, where the filament is broken into a discrete number of straight segments and the elastic interaction coupling neighboring nodes/joints is described via discrete elastic connectors encoding the filament's resistance to bending. However, so far, the CGM for filaments has been used by neglecting the two-way interaction between the filament and the fluid.

Carrying out numerical simulations for such challenging FSI problems is still computational expensive in spite of the algorithmic advances and the increased performance of computers. The use of machine learning, and more specifically Artificial Neural Networks (ANN), is gaining popularity in engineering research during the past few years due to their ability to solve complex FSI problems quickly. ANN are reliable and computationally inexpensive compared to numerical methods. Miyanawala and Jaiman [38] developped a hybrid data-driven technique for unsteady fluid-structure interaction systems using convolutional neural networks. Koh, Shen and Marcos [39] used supervised learning to predict sperm sorting by magnetophoresis, Fayed *et al.* employed ANN in order to predict the flapping frequencies of a filament placed in a 2-D soap-film tunnel, and Kanchan and Maniyeri [41] used ANN developed from IBM simulations in order to predict tumbling counts for two side-by-side placed filaments in shear flow. The ability of the ANN to reproduce accurate results in a computationally efficient way, as concluded by the aforementioned works, seems promising in solving accurately complex FSI problems while improving substantially the efficiency.

1.2 Objectives and outline

The contributions and goals of the current work can be grouped into the following parts:

- A new, modified, version of the IBM that combines the CGM with IBM and is more computationally efficient than the traditional IBM is proposed for modeling inextensible filaments in shear flow at low Reynolds numbers and is used to study the various two-dimensional orbit regimes of filaments,

- A prediction model using ANN is developed to effectively forecast the orbit regime of a filament,
- An extension of the traditional IBM to include a stochastic stress tensor is proposed for modeling the thermal fluctuations in the cytoplasmic fluid surrounding the actin cortex.

The theoretical values for time-averaged contraction for a single immersed inextensible filament under hydrodynamic thermal fluctuations through numerical simulations are verified through numerical simulations. The mechanical behavior of the actin cortex and its elasticity when subjected to shear flow is investigated, and lastly, the behavior, interaction, and motion of passive F-actin filaments under hydrodynamic thermal fluctuations are studied.

This thesis is organized as follows: Chapter 2 introduces the physical characteristics and balance laws of a filament immersed in a flow of a Newtonian, incompressible fluid and of low Reynolds number. The Navier-Stokes equations for the fluid are derived and the modeling of thermal fluctuations in the flow by means of a stochastic stress tensor is discussed. The mechanical behavior of semiflexible polymers is also descibed in this chapter. In Chapter 3, the state-of-the-art of ANN is presented. In Chapter 4, the weak forms of the balance laws presented in Chapter 2 are presented, and their spatial and temporal discretizations are formulated. The CGM is discussed, as well as the two proposed numerical algorithms of the present work are also described in this chapter. In Chapter 5, the two-dimensional numerical model based on a combination of IBM and CGM is implemented to capture the hydrodynamic interaction of filaments in viscous shear flow while strictly enforcing the filament inextensibility condition, without restricting the time step required in constrast to the regular IBM. The results of the modified IBM simulations are first validated and then used to develop prediction models based on ANN, in order to predict the two-dimensional orbit classes for flexible filaments placed in shear flow with different parameters. The response of a single inextensible filament using the proposed numerical algorithms is studied in order to verify the theoretical values for time-averaged contraction under thermal fluctuations. Furthermore, the mechanical behavior and elasticity of the actin cortex when subjected to shear is studied, illustrating a stiffening of the cross-linked network with increasing strain under shear flow. Lastly, the behavior and motion of passive F-actin filaments under hydrodynamic thermal fluctuations is investigated. A summary of the findings from the work presented in this dissertation as well as potential future extensions of the current research are discussed in Chapter 6.

Chapter 2

Theoretical Background

2.1 Overview

The cytoskeleton is a network of F-actin, microtubules, and intermediate filaments, immersed in the cytosol, the main component of the cytoplasm [1]. The structural elements of the cytoskeleton are classified as filaments, that is, string-like objects whose length is much greater than their diameter. The cytosol, which consists mostly of water, is considered to be an incompressible and Newtonian fluid.

In this chapter, the physical characteristics of a filament immersed in a flow of a Newtonian, incompressible fluid are introduced. The average motion of the fluid is defined by the Navier-Stokes equations, derived in Sections 2.2.1-2.2.3. At the cell level, thermal fluctuations play an essential role in the description of the fluid flow, and are introduced in Section 2.2.4. A homogenization method is discussed in Section 2.3. Additionally, the behavior of a single semiflexible filament is described in Section 2.4, with the Euler-Bernoulli beam theory defined in Section 2.4.1. Lastly, the WLC model is derived n Section 2.4.2, in order to obtain the theoretical value for the time-averaged contraction of an inextensible filament in thermal equilibrium.

2.2 Navier-Stokes equations

The Navier-Stokes equations were developed by Claude-Louis Navier and George Gabriel Stokes in 1822, and, given some initial conditions, these equations can be used to determine the velocity field and the pressure field in a fluid. The Navier-Stokes equations can be derived from the conservation of mass and the mechanical balance of linear momentum, combined with certain assumptions about the forces and the behavior of the fluid.

Let a continuum body $\mathscr{B}$ be defined as a set of material particles, which, when considered together, endow the body with local (pointwise) physical properties that are independent of its actual size or the time over which they are measured. Also, let

a typical such particle be denoted P, while an arbitrary subset of $\mathscr{B}$ be denoted $\mathscr{S}$, as shown in Figure 2.1

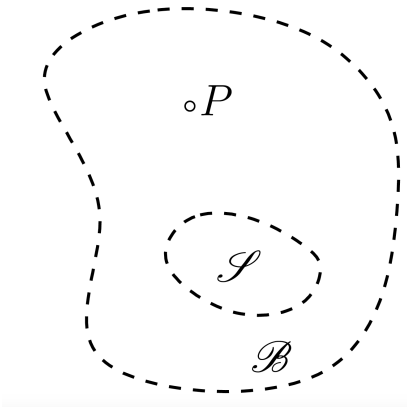

Figure 2.1: *A body $\mathscr{B}$ and its subset $\mathscr{S}$ [43]*

Let x be the point in the three-dimensional Euclidean point space $\mathcal{E}^3$ occupied by a particle P of the body $\mathscr{B}$ at time t, and let $\mathbf{x}$ be its associated position vector relative to the fixed origin O of an orthonormal basis in the three-dimensional Euclidean vector space E^3. Then, define by $\bar{\boldsymbol{\chi}}: \ (P,t) \in \mathscr{B} \times \mathbb{R} \to E^3$ the motion of $\mathscr{B}$, which is a mapping such that

$$\mathbf{x} \ = \ \bar{\boldsymbol{\chi}}(P,t) = \bar{\boldsymbol{\chi}}_t(P). \tag{2.1}$$

In the above, $\bar{\boldsymbol{\chi}}_t: \ \mathscr{B} \to \mathcal{E}^3$ is called the configuration mapping of $\mathscr{B}$ at time t. Given $\bar{\boldsymbol{\chi}}$, the body $\mathscr{B}$ may be mapped to its configuration $\mathcal{R} = \bar{\boldsymbol{\chi}}(\mathscr{B},t)$ with boundary $\partial\mathcal{R}$ at time t. Likewise, any part $\mathscr{S} \subset \mathscr{B}$ can be mapped to its configuration $\mathcal{P} = \bar{\boldsymbol{\chi}}(\mathscr{S},t)$ with boundary $\partial\mathcal{P}$ at time t, as shown in Figure 2.2.

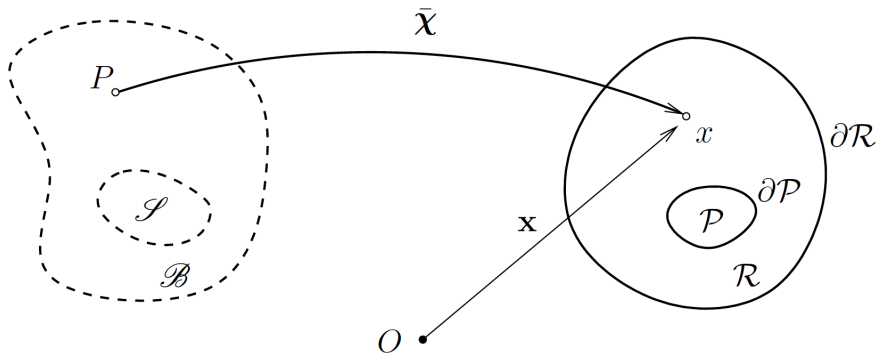

Figure 2.2: *Mapping of a body $\mathscr{B}$ to its configuration at time t [43]*

The configuration mapping $\bar{\boldsymbol{\chi}}_t$ is assumed to be invertible, which means that any point $\mathbf{x} \in \mathcal{R}$ can be uniquely associated to a particle P according to

$$P \;=\; \bar{\boldsymbol{\chi}}_t^{-1}(\mathbf{x}). \tag{2.2}$$

The motion $\bar{\boldsymbol{\chi}}$ of the body is also assumed to be twice-differentiable in time. Then, one may define the velocity of any particle P at time t according to

$$\mathbf{v} \;=\; \frac{\partial \bar{\boldsymbol{\chi}}(P,t)}{\partial t}. \tag{2.3}$$

2.2.1 Conservation of Mass

The mass density of a particle P occupying point $\mathbf{x}$ at time t in the current configuration is defined as a local measure at a given spatial position $\mathbf{x}$ and may be thought of as being derived by a limiting process as

$$\rho(\mathbf{x},t) \;=\; \lim_{\delta \to 0} \frac{\mathscr{S}_\delta}{\mathcal{P}_\delta}\ , \tag{2.4}$$

where $\mathcal{P}_\delta \subset \mathcal{E}^3$denotes a sphere of radius $\delta > 0$ centered at $\mathbf{x}$ and $\mathscr{S}_\delta$ the part of the body that occupies $\mathcal{P}_\delta$ at time t, as shown in Figure 2.3.

Figure 2.3: *A limiting process used to define the mass density ρ at a point $\mathbf{x}$ in the current configuration [43]*

Consider a body $\mathscr{B}$ that occupies a region $\mathscr{R} \subset \mathcal{E}^3$ with mass $m(\mathscr{B})$ and take any arbitrary part $\mathscr{S} \subseteq \mathscr{B}$ with mass $m(\mathscr{S})$. Assuming the mass m is an absolutely continuous measure, it can be established that

$$\int_{\mathscr{B}} dm \;=\; \int_{\mathscr{R}} \rho \, dv \;=\; m(\mathscr{B})\ , \tag{2.5}$$

and

$$\int_{\mathscr{S}} dm \;=\; \int_{\mathcal{P}} \rho \, dv \;=\; m(\mathscr{S}) \; . \tag{2.6}$$

The principle of mass conservation states that the mass of any material part of the body remains constant at all time, namely that

$$\frac{d}{dt} m(\mathscr{S}) \;=\; 0 \; , \tag{2.7}$$

or, upon recalling (2.6)

$$\frac{d}{dt} \int_{\mathcal{P}} \rho \, dv \;=\; 0 \; . \tag{2.8}$$

Using the Reynolds Transport Theorem [42] in the form

$$\frac{d}{dt} \int_{\mathcal{P}} \phi \, dv \;=\; \int_{\mathcal{P}} \big(\dot{\phi} + \phi \, \mathrm{div} \, \mathbf{v} \big) dv \; , \tag{2.9}$$

where $\mathrm{div} \, \mathbf{v} = \frac{\partial v_i}{\partial x_i} \, \mathbf{e}_i \cdot \mathbf{e}_j = v_{i,i}$ is the spatial divergence of the velocity vector and $\mathbf{e}_i$ are the cartesian basis vectors, ϕ is a scalar field defined by a spatial function such that $\phi \;=\; \phi(\mathbf{x}, t)$, and $\dot{\phi}$ is the material time derivative of the scalar field ϕ defined as

$$\dot{\phi} \;=\; \frac{\partial \phi}{\partial t} + \frac{\partial \phi}{\partial \mathbf{x}} \cdot \mathbf{v} \; . \tag{2.10}$$

Equation (2.8) may be then written as

$$\int_{\mathcal{P}} \big(\dot{\rho} + \rho \, \mathrm{div} \, \mathbf{v} \big) dv \;=\; 0 \; . \tag{2.11}$$

Assuming that the integrand in (2.11) is continuous and recalling that $\mathscr{S}$ (hence, also $\mathcal{P}$) is arbitrary, it follows from the localization theorem that

$$\dot{\rho} + \rho \, \mathrm{div} \, \mathbf{v} \;=\; 0 \; , \tag{2.12}$$

which can be readily rewritten using (2.10) as

$$\frac{\partial \rho}{\partial t} + \frac{\partial \rho}{\partial \mathbf{x}} \cdot \mathbf{v} + \rho \, \mathrm{div} \, \mathbf{v} \;=\; 0 \; , \tag{2.13}$$

or, equivalently,

$$\frac{\partial \rho}{\partial t} + \mathrm{div} \big(\rho \mathbf{v} \big) \;=\; 0 \; . \tag{2.14}$$

2.2.2 Principle of linear and angular momentum balance

The principle of linear momentum balance states that the rate of change of linear momentum for any part $\mathscr{S}$ of the body that occupies region $\mathcal{P}$ with boundary $\partial\mathcal{P}$ occupied at time t equals the total external forces acting on this part, *i.e.*,

$$\frac{d}{dt}\int_{\mathscr{S}} \mathbf{v}\, dm \;=\; \int_{\mathscr{S}} \mathbf{b}\, dm + \int_{\mathscr{S}} \mathbf{t}_{(\mathbf{n})}\, d\alpha \;, \tag{2.15}$$

where $\mathbf{b} = \mathbf{b}(\mathbf{x},t)$ is the body force per unit mass and, $\mathbf{t} = \mathbf{t}(\mathbf{x},t;\mathbf{n}) = \mathbf{t}_{(\mathbf{n})}(\mathbf{x},t)$ is the contact force per unit area, alternatively referred to as the stress vector, which acts on the particles which lie on boundary surfaces and depends on the orientation of the surface through the outward unit normal $\mathbf{n}$ to the surface.
Equivalently, using (2.6), (2.15) may be rewritten as

$$\frac{d}{dt}\int_{\mathcal{P}} \rho\mathbf{v}\, dv \;=\; \int_{\mathcal{P}} \rho\mathbf{b}\, dv + \int_{\partial\mathcal{P}} \mathbf{t}_{(\mathbf{n})}\, d\alpha \;. \tag{2.16}$$

Using the Reynolds transport theorem in the form (2.9) and the conservation of mass in the form (2.11), the left-hand side of (2.16) can be written as

$$\begin{aligned}
\frac{d}{dt}\int_{\mathcal{P}} \rho\,\mathbf{v}\, dv \;&=\; \int_{\mathcal{P}} \dot{\overline{(\rho\mathbf{v})}}\, dv + \int_{\mathcal{P}} \rho\mathbf{v}\,\operatorname{div}\mathbf{v}\, dv \\
&=\; \int_{\mathcal{P}} \left(\dot{\rho}\mathbf{v} + \rho\dot{\mathbf{v}}\right) dv + \int_{\mathcal{P}} \rho\mathbf{v}\,\operatorname{div}\mathbf{v}\, dv \\
&=\; \int_{\mathcal{P}} \left[\left(\dot{\rho} + \rho\,\operatorname{div}\mathbf{v}\right)\mathbf{v} + \rho\dot{\mathbf{v}}\right] dv \\
&=\; \int_{\mathcal{P}} \rho\dot{\mathbf{v}}\, dv \;.
\end{aligned} \tag{2.17}$$

Upon using the divergence theorem and the relation between the stress vector and the Cauchy stress tensor,

$$\mathbf{t}_{(\mathbf{n})} \;=\; \mathbf{t}_i n_i \;=\; \mathbf{T}\,\mathbf{n} \;, \tag{2.18}$$

where $\mathbf{T}$ is the Cauchy stress tensor defined as

$$\mathbf{T} \;=\; \mathbf{t}_i \otimes \mathbf{e}_i \;, \tag{2.19}$$

the balance of linear momentum becomes

$$\int_{\mathcal{P}} \rho\dot{\mathbf{v}}\, dv \;=\; \int_{\mathcal{P}} \rho\mathbf{b}\, dv + \int_{\mathcal{P}} \operatorname{div}\mathbf{T}\, dv \;. \tag{2.20}$$

With the aid of the localization theorem, Equation (2.20) leads to a local form of linear momentum balance in the form

$$\rho\dot{\mathbf{v}} \;=\; \rho\mathbf{b} + \operatorname{div}\mathbf{T}\;, \tag{2.21}$$

or, using (2.16), (2.18) and the divergence theorem,

$$\int_{\mathcal{P}} \rho\dot{\mathbf{v}}\; dv \;=\; \int_{\mathcal{P}} \rho\mathbf{b}\; dv + \int_{\partial\mathcal{P}} \mathbf{t}_{(\mathbf{n})}\; d\alpha \tag{2.22}$$

$$= \int_{\mathcal{P}} \rho\mathbf{b}\; dv + \int_{\partial\mathcal{P}} \mathbf{t}_i n_i\; d\alpha \tag{2.23}$$

$$= \int_{\mathcal{P}} \rho\mathbf{b}\; dv + \int_{\mathcal{P}} \mathbf{t}_{i,i}\; dv. \tag{2.24}$$

Appealing, once more, to the localization theorem, this leads to

$$\rho\dot{\mathbf{v}} \;=\; \rho\mathbf{b} + \mathbf{t}_{i,i}\;. \tag{2.25}$$

The principle of angular momentum balance states that the rate of change of angular momentum for any part $\mathscr{S}$ of the body that occupies region $\mathcal{P}$ with boundary $\partial\mathcal{P}$ occupied at time t equals the total external forces acting on this part, *i.e.*,

$$\frac{d}{dt}\int_{\mathscr{S}} \mathbf{x}\times\mathbf{v}\; dm \;=\; \int_{\mathscr{S}} \mathbf{x}\times\mathbf{b}\; dm + \int_{\mathscr{S}} \mathbf{x}\times\mathbf{t}_{(\mathbf{n})}\; d\alpha\;, \tag{2.26}$$

or, again, by way of (2.6),

$$\frac{d}{dt}\int_{\mathcal{P}} \mathbf{x}\times\rho\mathbf{v}\; dv \;=\; \int_{\mathcal{P}} \mathbf{x}\times\rho\mathbf{b}\; dv + \int_{\partial\mathcal{P}} \mathbf{x}\times\mathbf{t}_{(\mathbf{n})}\; d\alpha\;. \tag{2.27}$$

Using the Reynolds transport theorem in the form (2.9) and the conservation of mass in the form (2.11), the left-hand side of (2.26) can be written as

$$\frac{d}{dt}\int_{\mathcal{P}} \mathbf{x}\times\rho\,\mathbf{v}\; dv \;=\; \int_{\mathcal{P}} \Big[\dot{(\overline{\mathbf{x}\times\rho\mathbf{v}})} + \big(\mathbf{x}\times\rho\mathbf{v}\big)\operatorname{div}\mathbf{v}\Big]\; dv \tag{2.28}$$

$$= \int_{\mathcal{P}} \big[\big(\dot{\mathbf{x}}\times\rho\mathbf{v} + \mathbf{x}\times\dot{\rho}\mathbf{v} + \mathbf{x}\times\rho\dot{\mathbf{v}}\big) + \big(\mathbf{x}\times\rho\mathbf{v}\operatorname{div}\mathbf{v}\big)\big]\; dv \tag{2.29}$$

$$= \int_{\mathcal{P}} \big[\mathbf{x}\times\big(\dot{\rho} + \rho\operatorname{div}\mathbf{v}\big)\mathbf{v} + \mathbf{x}\times\dot{\mathbf{v}}\big]\; dv \tag{2.30}$$

$$= \int_{\mathcal{P}} \mathbf{x}\times\rho\dot{\mathbf{v}}\; dv\;. \tag{2.31}$$

As a result, the principle of angular momentum balance may be also written as

$$\int_{\mathcal{P}} \mathbf{x}\times\rho\dot{\mathbf{v}}\; dv \;=\; \int_{\mathcal{P}} \mathbf{x}\times\rho\mathbf{b}\; dv + \int_{\partial\mathcal{P}} \mathbf{x}\times\mathbf{t}_{(\mathbf{n})}\; d\alpha\;. \tag{2.32}$$

Using Equation (2.18) and the divergence theorem,

$$\int_{\partial\mathcal{P}} \mathbf{x}\times\mathbf{t}_{(\mathbf{n})}\,d\alpha \;=\; \int_{\partial\mathcal{P}} \mathbf{x}\times\mathbf{t}_i n_i\,d\alpha \;=\; \int_{\mathcal{P}} \left(\mathbf{x}\times\mathbf{t}_i\right)_{,i}\,dv \;=\; \int_{\mathcal{P}} \left(\mathbf{e}_i\times\mathbf{t}_i + \mathbf{x}\times\mathbf{t}_{i,i}\right)_{,i}\,dv\;, \tag{2.33}$$

since $\mathbf{x} = x_i\mathbf{e}_i$. Equation (2.32) then yields

$$\int_{\mathcal{P}} \mathbf{x}\times\rho\dot{\mathbf{v}}\,dv \;=\; \int_{\mathcal{P}} \mathbf{x}\times\rho\mathbf{b}\,dv + \int_{\mathcal{P}} \left(\mathbf{e}_i\times\mathbf{t}_i + \mathbf{x}\times\mathbf{t}_{i,i}\right)\,dv\;, \tag{2.34}$$

or, upon rearranging the terms,

$$\int_{\mathcal{P}} \left[\mathbf{x}\times\left(\rho\dot{\mathbf{v}} - \rho\mathbf{b} - \mathbf{t}_{i,i}\right) + \mathbf{e}_i\times\mathbf{t}_i\right]\,dv \;=\; \mathbf{0}\;. \tag{2.35}$$

Recalling the local form of linear momentum balance in (2.25), the above equation reduces to

$$\int_{\mathcal{P}} \mathbf{e}_i\times\mathbf{t}_i\,dv \;=\; \mathbf{0}\;. \tag{2.36}$$

The localization theorem may be invoked again to conclude that

$$\mathbf{e}_i\times\mathbf{t}_i \;=\; \mathbf{0}\;. \tag{2.37}$$

Upon expressing $\mathbf{T}$ in component form as $\mathbf{T} = T_{ki}\mathbf{e}_k\otimes\mathbf{e}_i$, it follows from (2.19) that

$$\mathbf{t}_i \;=\; T_{ki}\mathbf{e}_k = \mathbf{T}\mathbf{e}_i\;. \tag{2.38}$$

Therefore, in component form, (2.37) can be expressed as

$$\mathbf{e}_i\times\left(T_{ji}\mathbf{e}_j\right) \;=\; T_{ji}\mathbf{e}_i\times\mathbf{e}_j \;=\; \mathbf{0}\;, \tag{2.39}$$

which means that $T_{ij} = T_{ji}$ or, in direct form,

$$\mathbf{T} \;=\; \mathbf{T}^T\;, \tag{2.40}$$

where $\mathbf{T}^T$ is the transpose of the Cauchy stress tensor $\mathbf{T}$. Hence, angular momentum balance requires that the Cauchy stress tensor be symmetric.

2.2.3 Navier-Stokes Equations for Newtonian, incompressible fluids

A fluid is incompressible if it can only undergo isochoric motions. A change in the density of the fluid over time would violate the volume preserving property of the fluid and, therefore, the material time derivative of the density in (2.12) can be set

equal to zero for an incompressible fluid. Dividing through by the constant ρ, the conservation of mass simplifies to

$$\operatorname{div} \mathbf{v} \;=\; 0 \;. \tag{2.41}$$

Starting from a general constitutive law for viscous fluids, i.e. fluids that exhibit some viscosity, that is, some capacity to resist shearing, and after invoking invariance under superposed rigid-body motions, it is reasonable to deduce that the Cauchy stress tensor is of the form $\mathbf{T} = \hat{\mathbf{T}}(\rho, \mathbf{D})$, where $\mathbf{D} \;=\; \frac{1}{2}\Big(\frac{\partial \mathbf{v}}{\partial \mathbf{x}} + \big(\frac{\partial \mathbf{v}}{\partial \mathbf{x}}\big)^T\Big)$ is the rate of deformation. After invoking incompressibility, the Cauchy stress tensor for incompressible Newtonian viscous fluids takes the form

$$\mathbf{T} \;=\; -p\mathbf{i} + 2\mu\mathbf{D} \;, \tag{2.42}$$

where μ is the dynamic viscosity of the fluid, p is the pressure field, and $\mathbf{i}$ is the spatial identity tensor.

Conservation of mass and balance of linear momentum can be expressed now as

$$\begin{aligned} \operatorname{div} \mathbf{v} \;&=\; 0 \;, \\ \operatorname{div}\big(-p\mathbf{i} + 2\mu\mathbf{D}\big) + \rho\mathbf{b} \;&=\; \rho\dot{\mathbf{v}} \;. \end{aligned} \tag{2.43}$$

The left-hand side of $(2.43)_2$ takes the form

$$\begin{aligned} \operatorname{div}\big(-p\mathbf{i} + 2\mu\mathbf{D}\big) + \rho\mathbf{b} \;&=\; -\operatorname{grad} p + \mu\big(\operatorname{div}\operatorname{grad}\mathbf{v} + \operatorname{grad}\operatorname{div}\mathbf{v}\big) + \rho\mathbf{b} \\ &=\; -\operatorname{grad} p + \mu\operatorname{div}\operatorname{grad}\mathbf{v} + \rho\mathbf{b} \;, \end{aligned} \tag{2.44}$$

hence the governing equations of (2.43), using also the material time derivative for $\dot{\mathbf{v}}$, become

$$\begin{aligned} \operatorname{div} \mathbf{v} \;&=\; 0 \;, \\ -\operatorname{grad} p + \mu\operatorname{div}\operatorname{grad}\mathbf{v} + \rho\mathbf{b} \;&=\; \rho\Big(\frac{\partial \mathbf{v}}{\partial t} + \frac{\partial \mathbf{v}}{\partial \mathbf{x}}\mathbf{v}\Big) \;. \end{aligned} \tag{2.45}$$

where $\operatorname{grad} p = \frac{\partial p}{\partial x_i}\mathbf{e}_i$.

The Reynolds number is a scalar measure of the relative importance of the inertial force compared to the force from viscosity of a fluid and is defined as

$$\mathrm{Re} \;=\; \frac{\rho v L}{\mu} \;, \tag{2.46}$$

where v is the flow speed and L is the characteristic linear dimension.

The flow in cytosol is of a low Reynolds number, on the order of 10^{-9}, due to the cell's small length scale which is in the order of μm as stated in [1]. For flows with low Reynolds number, the convection rate of change $\frac{\partial \mathbf{v}}{\partial \mathbf{x}}\mathbf{v}$ in (2.45) can be neglected.

However, the partial time derivative term $\frac{\partial \mathbf{v}}{\partial t}$ in (2.45) is kept for capturing the effects of the unsteady flow.

2.2.4 Hydrodynamic Fluctuations

As one approaches smaller length scales, on the order of μm, thermal fluctuations play an essential role in the description of the fluid flow. Thermal fluctuations may be included in the continuum description of the fluid by means of additional stochastic fluxes. The resulting equations of motion for the fluctuating fluid turn out to be stochastic partial differential equations. Landau and Lifshitz [44, Chapter 9] proposed such equations, which include an additional stochastic stress tensor in the Navier-Stokes equations, the so-called Landau-Lifshitz Navier-Stokes (LLNS) equations.

To account for thermal fluctuations, the Cauchy stress tensor $\mathbf{T}$ for an incompressible viscous fluid can be modified as

$$\mathbf{T} \;=\; -p\mathbf{i} + 2\mu\mathbf{D} + \tilde{\mathbf{S}} \;, \tag{2.47}$$

where p is the pressure, μ is the dynamic viscosity of the fluid, $\mathbf{D}$ is the rate-of-deformation tensor, and $\tilde{\mathbf{S}}$ stands for the stochastic stress tensor, which models the inherent molecular fluctuations in the fluid. The required stochastic properties of $\tilde{\mathbf{S}}$ have been derived by Landau and Lifshitz [44] by satisfying the fluctuation dissipation theorem [44], according to

$$\begin{aligned} < \tilde{\mathbf{S}}(\mathbf{x},t) > \;&=\; \mathbf{0} \;, \\ < \tilde{\mathbf{S}}(\mathbf{x},t) \otimes \tilde{\mathbf{S}}(\mathbf{x}',t') > \;&=\; 4k_B T\mu\delta(\mathbf{x}-\mathbf{x}')\delta(t-t')\mathbb{I} \;, \end{aligned} \tag{2.48}$$

where $\delta(\cdot)$ is the Dirac delta function, $\mathbb{I}$ is the symmetric fourth-order identity tensor, $< \cdot >$ denotes ensemble average and $\otimes$ denotes tensor product.

By way of background, recall that the ensemble average $< A(t) >$ of an observable quantity A, which is a function of a variable $\mathbf{\Gamma}$ at time t, is defined as [47]

$$< A(t) > \;=\; \int_{\gamma} A(\mathbf{\Gamma}) f(\mathbf{\Gamma},t)\, \mathrm{d}\mathbf{\Gamma} \;, \tag{2.49}$$

see, *e.g.*, [48, Chapter 3]. Here, γ is the phase space of $\mathbf{\Gamma}$ and $f(\mathbf{\Gamma},t)$ is the phase-space distribution function, defined as the probability that the system will be in state $\mathbf{\Gamma}$ at time t. The probability density function satisfies the standard consistency condition $\int_{\gamma} f(\mathbf{\Gamma},t)\, \mathrm{d}\mathbf{\Gamma} = 1$.

The Navier-Stokes equations for an incompressible, Newtonian fluid with low-Reynolds number and with the additional stochastic stress tensor to account for the thermal fluctuations can be written as

$$\begin{aligned} \mathrm{div}\ \mathbf{v} \;&=\; 0 \;, \\ -\mathrm{grad}\ p + \mu \mathrm{div}\ \mathrm{grad}\ \mathbf{v} + \mathrm{div}\ \tilde{\mathbf{S}} + \rho\mathbf{b} \;&=\; \rho\frac{\partial \mathbf{v}}{\partial t} \;. \end{aligned} \tag{2.50}$$

2.3 Homogenization Method

In this section the continuum homogenization method proposed in [45] is briefly described. It is a continuum thermomechanical homogenization method inspired by the Irving & Kirkwood [50] procedure relating the atomistic equations of motion to the balance laws of continuum mechanics. This method yields expressions for the macroscopic stress in terms of microscopic kinematic and kinetic quantities, under the fundamental assumption that continuum mechanical modeling is permissible at both scales.

2.3.1 Homogenization in spatial form

Balance laws are written in spatial form for both the microscopic and macroscopic scale, and a homogenization procedure is proposed that yields expressions for macroscopic stress as a function of microscopic quantities.

Consider a body $\mathcal{B}$ that occupies a region $\mathcal{R}$ in the spatial configuration and let each point $\mathbf{y}$ in $\mathcal{R}$ be associated in a microscopic scale with a region whose typical point is denoted by $\mathbf{x}$ as shown in Figure 2.4.

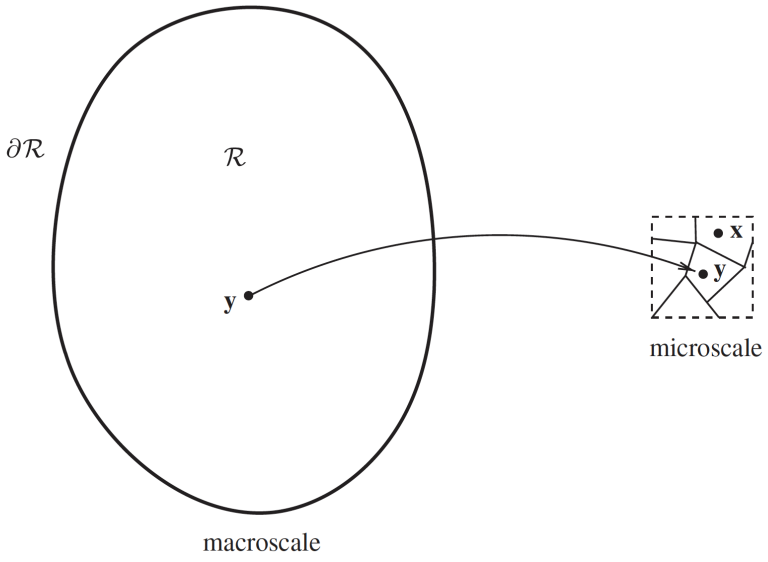

Figure 2.4: *Macroscopic and microscopic representations in the spatial configuration [45]*

The local forms of macroscopic balances of mass and linear momentum may be written as

$$\begin{aligned} \dot{\rho}^M + \rho^M \mathrm{div}_{\mathbf{y}} \mathbf{v}^M &= 0 \ , \\ \rho^M \dot{\mathbf{v}}^M &= \mathrm{div}_{\mathbf{y}} \mathbf{T}^M + \rho^M \mathbf{b}^M \ , \end{aligned} \tag{2.51}$$

where M stands for macroscopic, $\rho^M(\mathbf{y}, t)$ is the mass density, $\mathbf{v}^M(\mathbf{y}, t) = \dot{\mathbf{y}}$ is the velocity, and $\mathbf{T}^M$ is the macroscopic Cauchy stress tensor. Here, '$\mathrm{div}_{\mathbf{y}}$' denotes the divergence operator relative to $\mathbf{y}$.
Likewise, the local forms of microscopic balances of mass and linear momentum may be written as

$$\begin{aligned} \dot{\rho}^m + \rho^m \mathrm{div}_{\mathbf{x}} \mathbf{v}^m &= 0 \ , \\ \rho^m \dot{\mathbf{v}}^m &= \mathrm{div}_{\mathbf{x}} \mathbf{T}^m + \rho^m \mathbf{b}^m \ , \end{aligned} \tag{2.52}$$

where m stands for microscopic and '$\mathrm{div}_{\mathbf{x}}$' now denotes the divergence operator relative to $\mathbf{x}$.

Assuming that the pointwise macroscopic mass density and linear momentum are weighted volumetric averages of mass and linear momentum over the microscopic points around point $\mathbf{y}$, relations between microscopic and macroscopic quantities are postulated as follows

$$\begin{aligned} \rho^M(\mathbf{y}, t) &= \int_{\mathcal{R}} \rho^m(\mathbf{x}, t) g(\mathbf{y}, \mathbf{x}) \mathrm{d}v^m \ , \\ \rho^M(\mathbf{y}, t) \mathbf{v}^M(\mathbf{y}, t) &= \int_{\mathcal{R}} \rho^m(\mathbf{x}, t) \mathbf{v}^m(\mathbf{y}, t) g(\mathbf{y}, \mathbf{x}) \mathrm{d}v^m \ . \end{aligned} \tag{2.53}$$

Here, $g(\mathbf{y}, \mathbf{x})$ is a weighting function which quantifies the relative contribution of the microscopic point $\mathbf{x}$ in the definition of the pointwise quantities at $\mathbf{y}$. The weighting function $g(\mathbf{y}, \mathbf{x})$ is assumed to be continuous and to possess the following additional properties: (i) $\int_{\mathcal{R}} g(\mathbf{y}, \mathbf{x}) \mathrm{d}v^m = 1$, (ii) $l_m << \mathrm{supp}\ g << \mathcal{R}$, where 'supp' denotes the support of a function and l_m is the charateristic microstructural length, (iii) $g(\mathbf{y}, \mathbf{x}) = 0$ on $\partial\mathcal{R}$ when $\mathbf{y} \in \mathcal{R}$ and (iv) $g(\mathbf{y}, \mathbf{x})$ attains a maximum when $\mathbf{y} = \mathbf{x}$. Assumption (i) is a standard normalization condition that enforces consistency of the relations (2.53). In addition, assumptions (ii) and (iv) signify the local nature of the macroscopic quantities, whereas assumption (iii) implies that $g(\mathbf{y}, \mathbf{x})$ affects only interior averaging.

An additional assumption made here is that the function $g(\mathbf{y}, \mathbf{x})$ is invariant under superposed rigid motions. This implies that

$$g(\mathbf{Q}\mathbf{y} + \mathbf{c}, \mathbf{Q}\mathbf{x} + \mathbf{c}) = g(\mathbf{y}, \mathbf{x}) \ . \tag{2.54}$$

Choosing now $\mathbf{Q} = \mathbf{i}$ and $\mathbf{C} = -\mathbf{x}$, where $\mathbf{i}$ is the spatial identity tensor, it follows from (2.54) tha g is exclusively a function of $\mathbf{y} - \mathbf{x}$. Furthermore, because g is a scalar function of a vector argument, it can depend only on the magnitude $|\mathbf{y} - \mathbf{x}|$ (because

the direction would change arbitrarily by the choice of the rotation $\mathbf{Q}$), which implies that

$$\frac{\partial}{\partial \mathbf{x}} g(\mathbf{y},\mathbf{x}) \;=\; -\frac{\partial}{\partial \mathbf{y}} g(\mathbf{y},\mathbf{x}) \;. \tag{2.55}$$

Taking the time derivative of $(2.53)_2$ yields

$$\begin{aligned}
\overline{\dot{\rho^M \mathbf{v}^M}} \;&=\; \frac{\mathrm{d}}{\mathrm{d}t}\int_{\mathcal{R}} \rho^m \mathbf{v}^m g(\mathbf{y},\mathbf{x}) \mathrm{d}v^m \\
&=\; \int_{\mathcal{R}} \dot{\rho}^m \mathbf{v}^m g(\mathbf{y},\mathbf{x}) \mathrm{d}v^m + \int_{\mathcal{R}} \rho^m \dot{\mathbf{v}}^m g(\mathbf{y},\mathbf{x}) \mathrm{d}v^m \\
&+ \int_{\mathcal{R}} \rho^m \mathbf{v}^m \frac{\partial}{\partial \mathbf{x}} g(\mathbf{y},\mathbf{x}) \cdot \mathbf{v}^m \mathrm{d}v^m \\
&+ \int_{\mathcal{R}} \rho^m \mathbf{v}^m \frac{\partial}{\partial \mathbf{y}} g(\mathbf{y},\mathbf{x}) \cdot \mathbf{v}^M \mathrm{d}v^m + \int_{\mathcal{R}} \rho^m \mathbf{v}^m g(\mathbf{y},\mathbf{x}) \frac{\partial}{\partial \mathbf{x}} \cdot \mathbf{v}^m \mathrm{d}v^m \;.
\end{aligned} \tag{2.56}$$

Using the microscopic balances of mass and linear momentum given by $(2.51)_1$ and $(2.51)_2$, respectively, as well as the identity (2.55), equation (2.56) is reduced to

$$\begin{aligned}
\overline{\dot{\rho^M \mathbf{v}^M}} \;&=\; \int_{\mathcal{R}} \big(\mathrm{div}_{\mathbf{x}} \mathbf{T}^m + \rho^m \mathbf{b}^m\big) g(\mathbf{y},\mathbf{x}) \mathrm{d}v^m - \int_{\mathcal{R}} \mathrm{div}_{\mathbf{y}} \Big[(\rho^m (\mathbf{v}^m \otimes \mathbf{v}^m) g(\mathbf{y},\mathbf{x})\Big] \mathrm{d}v^m \\
&+ \int_{\mathcal{R}} \rho^m (\mathbf{v}^m \otimes \mathbf{v}^m) \frac{\partial}{\partial \mathbf{y}} g(\mathbf{y},\mathbf{x}) \mathrm{d}v^m \;.
\end{aligned} \tag{2.57}$$

Using the divergence theorem, the identity (2.55), property (iii) of weighting function, $(2.51)_2$ and (2.53), equation (2.57) may be reduced to

$$\begin{aligned}
\rho^M \dot{\mathbf{v}}^M \;&=\; \mathrm{div}_{\mathbf{y}} \int_{\mathcal{R}} \Big[\mathbf{T}^m - \rho^m (\mathbf{v}^m - \mathbf{v}^M) \otimes (\mathbf{v}^m - \mathbf{v}^M)\Big] g(\mathbf{y},\mathbf{x}) \; \mathrm{d}v^m \\
&+ \int_{\mathcal{R}} \rho^m \mathbf{b}^m g(\mathbf{y},\mathbf{x}) \; \mathrm{d}v^m \;.
\end{aligned} \tag{2.58}$$

which is analogous in form to the balance of macroscale linear momentum in (2.51). Comparing the two terms with the right-hand side of (2.59) and (2.51), it follows that body force at the macroscale is given by

$$\rho^M \mathbf{b}^M \;=\; \int_{\mathcal{R}} \rho^m \mathbf{b}^m g(\mathbf{y},\mathbf{x}) \; \mathrm{d}v^m \;, \tag{2.59}$$

whereas the stress tensor is defined as

$$\mathbf{T}^M \;=\; \int_{\mathcal{R}} \Big(\mathbf{T}^m - \rho^m (\mathbf{v}^m - \mathbf{v}^M) \otimes (\mathbf{v}^m - \mathbf{v}^M)\Big) g(\mathbf{y},\mathbf{x}) \; \mathrm{d}v^m \;, \tag{2.60}$$

to within a divergence-free tensor function of $(\mathbf{y}, t)$. At any given point $\mathbf{y}$ and time t,

this function may be set to zero, provided that the balance laws and assorted boundary conditions are satisfied simultaneously in both scales. Equation (2.60) shows that the macroscopic stress comprises two terms: the first is equal to the volumetric average of the microscopic stress, whereas the second is due to the momentum induced by the velocity of the microscale relative to the macroscale.

2.4 Semiflexible Polymers

A filament can respond to forces applied to it by bending, stretching or compressing. The filaments comprising the cytoskeleton are classified as being semiflexible because of their long persistence length l_p, which is comparable to the total contour length. What the persistence length means in simple terms is that a filament in thermal equilibrium in a fluid will appear rather straight over lengths that are short compared with this persistence length, and its bending can be described in mechanical terms, as for elastic rods. However, it will begin to exhibit a random, contorted shape on longer-length scales due to the significant thermally induced bending fluctuations caused by Brownian motion in the fluid, in which case its stretching and compression may involve a purely elastic or mechanical response, a purely entropic response, or a combination of the two. Figure 2.5 shows different shapes of filaments in thermal equilibrium for different length scales and persistence lengths.

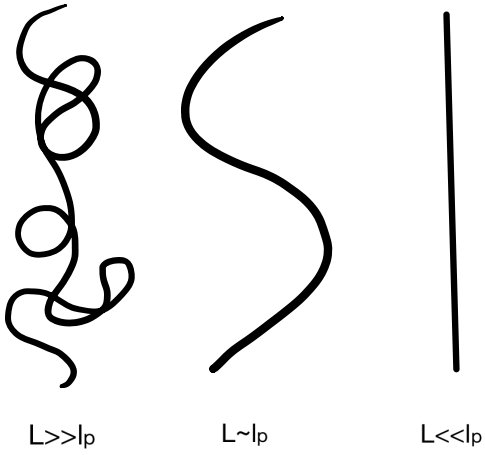

Figure 2.5: *Filament shapes in thermal equilibrium for different cases of persistence length l_p and contour length L*

2.4.1 Elastic rods

A semiflexible filament in thermal equilibrium, whose length is much greater than its width, may be represented as a continuously isotropic Euler beam on length scales shorter than the persistence length. An initially straight thin isotropic elastic rod is

considered, of initial length L, uniform circular cross-sectional area with radius a and Young's modulus E. The formation of the rod can be decomposed, at the order of linear elasticity, into compression/extension, bending and twist. In the case of a rod with free ends, the twist deformation is dissipated out of the unconstrained body. For this reason, the twist deformation is ignored in this study [46].

Let the space curve $\mathbf{r} = \mathbf{r}(s,t)$ describe the shape of the rod, where s is the arc-length coordinate in the current configuration that runs from 0 to $L(t)$. The strain along the rod is given by

$$\epsilon(s,t) = \left|\frac{\partial \mathbf{r}}{\partial s}\right| - 1 \ . \tag{2.61}$$

The strain energy E_s in the rod is then

$$E_s = \frac{\kappa_s}{2}\int_0^{L(t)} \epsilon(s,t)^2 \mathrm{d}s = \frac{\kappa_s}{2}\int_0^{L(t)} \left(\left|\frac{\partial \mathbf{r}}{\partial s}\right| - 1\right)^2 \mathrm{d}s \ , \tag{2.62}$$

where κ_s is the axial rigidity defined as $\kappa_s = EA$.

The (linearized) curvature is defined as $\kappa = \left|\frac{\partial^2 \mathbf{r}}{\partial s^2}\right|$ and the bending energy E_b is given by

$$E_b = \frac{\kappa_b}{2}\int_0^{L(t)} \kappa^2 \mathrm{d}s = \frac{\kappa_b}{2}\int_0^{L(t)} \left|\frac{\partial^2 \mathbf{r}}{\partial s^2}\right|^2 \mathrm{d}s \ , \tag{2.63}$$

where κ_b is the flexular rigidity defined as $\kappa_b = EI$, expressed in terms of the Young's modulus E and the second moment of area $I = \frac{\pi a^4}{4}$.

Consider a perturbation $\delta\mathbf{r}(s,t)$ of the curve configuration $\mathbf{r}(s,t)$. Up to terms of first order, the resulting perturbation in elastic energy will be a linear functional of the perturbation in configuration of the material and the functional can be put in the form

$$\delta E\big[\mathbf{r}(s,t)\big] = \int_0^{L(t)} -\mathbf{f}(s,t)\cdot\delta\mathbf{r}(s,t)\mathrm{d}s \ . \tag{2.64}$$

where the function $-\mathbf{f}(s,t)$ is the Fréchet derivative of E evaluated at the configuration $\mathbf{r}(s,t)$. The physical interpretation of the foregoing is that $\mathbf{f}(s,t)$ is the force density generated by the elasticity of the material [32]. This is essentially the principle of virtual work. Therefore, the generated stretching force density $\mathbf{f}_s$ can be expressed as

$$\mathbf{f}_s(s,t) = -\frac{\delta E_s}{\delta \mathbf{r}} \ . \tag{2.65}$$

A variation of the functional E_s is performed to obtain

$$
\begin{aligned}
\delta E_s &= \lim_{\epsilon\to 0}\frac{1}{\epsilon}\left[\frac{\kappa_s}{2}\int_0^L\left(\left(\left|\frac{\partial(\mathbf{r}+\epsilon\delta\mathbf{r})}{\partial s}\right|-1\right)^2-\left(\left|\frac{\partial\mathbf{r}}{\partial s}\right|-1\right)^2\right)\mathrm{d}s\right]\\
&= \lim_{\epsilon\to 0}\frac{1}{\epsilon}\left[\frac{\kappa_s}{2}\int_0^L\left(\left|\frac{\partial(\mathbf{r}+\epsilon\delta\mathbf{r})}{\partial s}\right|\cdot\left|\frac{\partial(\mathbf{r}+\epsilon\delta\mathbf{r})}{\partial s}\right|-2\left|\frac{\partial(\mathbf{r}+\epsilon\delta\mathbf{r})}{\partial s}\right|+1\right.\right.\\
&\quad\left.\left.-\left|\frac{\partial\mathbf{r}}{\partial s}\right|\cdot\left|\frac{\partial\mathbf{r}}{\partial s}\right|+2\left|\frac{\partial\mathbf{r}}{\partial s}\right|-1\right)\mathrm{d}s\right]\\
&= \lim_{\epsilon\to 0}\frac{1}{\epsilon}\left[\frac{\kappa_s}{2}\int_0^L\left(2\epsilon\frac{\partial\delta\mathbf{r}}{\partial s}\cdot\frac{\partial\mathbf{r}}{\partial s}+\epsilon^2\frac{\partial\delta\mathbf{r}}{\partial s}\cdot\frac{\partial\delta\mathbf{r}}{\partial s}-2\left|\frac{\partial\mathbf{r}}{\partial s}+\epsilon\frac{\partial\delta\mathbf{r}}{\partial s}\right|-2\left|\frac{\partial\mathbf{r}}{\partial s}\right|\right)\mathrm{d}s\right]\\
&= \kappa_s\int_0^L\left(-\frac{\partial\delta\mathbf{r}}{\partial s}\cdot\frac{\partial\mathbf{r}}{\partial s}+\frac{\frac{\partial\mathbf{r}}{\partial s}}{\left|\frac{\partial\mathbf{r}}{\partial s}\right|}\cdot\frac{\partial\delta\mathbf{r}}{\partial s}\right)\mathrm{d}s\ . \qquad (2.66)
\end{aligned}
$$

Using integration by parts (variations at the boundary neglected) it results that

$$
\delta E_s = \kappa_s\int_0^L\left[\frac{\partial^2\mathbf{r}}{\partial s^2}\cdot\delta\mathbf{r}+\frac{\partial}{\partial s}\left(\frac{\frac{\partial\mathbf{r}}{\partial s}}{\left|\frac{\partial\mathbf{r}}{\partial s}\right|}\right)\cdot\delta\mathbf{r}\right]\mathrm{d}s\ . \qquad (2.67)
$$

Therefore, from (2.65) and (2.66), the stretching force density along the rod is equal to

$$
\begin{aligned}
\mathbf{f}_s(s,t) &= \kappa_s\left[\frac{\partial^2\mathbf{r}}{\partial s^2}+\frac{\partial}{\partial s}\left(\frac{\frac{\partial\mathbf{r}}{\partial s}}{\left|\frac{\partial\mathbf{r}}{\partial s}\right|}\right)\right]\\
&= \kappa_s\frac{\partial}{\partial s}\left[\frac{\partial\mathbf{r}}{\partial s}-\frac{\frac{\partial\mathbf{r}}{\partial s}}{\left|\frac{\partial\mathbf{r}}{\partial s}\right|}\right]\\
&= \kappa_s\frac{\partial}{\partial s}\left[\left(\left|\frac{\partial\mathbf{r}}{\partial s}\right|-1\right)\frac{\frac{\partial\mathbf{r}}{\partial s}}{\left|\frac{\partial\mathbf{r}}{\partial s}\right|}\right]\ . \qquad (2.68)
\end{aligned}
$$

By invoking the principle of virtual work, the generated bending force density $\mathbf{f}_b$ can be expressed as

$$
\mathbf{f}_b(s,t) = -\frac{\delta E_b}{\delta\mathbf{r}}\ . \qquad (2.69)
$$

A variation of the functional E_b is performed and it is obtained that

$$\begin{aligned}
\delta E_b &= \lim_{\epsilon\to 0}\frac{1}{\epsilon}\left(\frac{\kappa_b}{2}\int_0^L \left(\left|\frac{\partial^2(\mathbf{r}+\epsilon\delta\mathbf{r})}{\partial s^2}\right|^2 - \left|\frac{\partial^2\mathbf{r}}{\partial s^2}\right|^2\right)\mathrm{d}s\right) \\
&\quad \lim_{\epsilon\to 0}\frac{1}{\epsilon}\left(\frac{\kappa_b}{2}\int_0^L \left(\frac{\partial^2(\mathbf{r}+\epsilon\delta\mathbf{r})}{\partial s^2}\cdot\frac{\partial^2(\mathbf{r}+\epsilon\delta\mathbf{r})}{\partial s^2} - \frac{\partial^2\mathbf{r}}{\partial s^2}\cdot\frac{\partial^2\mathbf{r}}{\partial s^2}\right)\mathrm{d}s\right) \\
&= \lim_{\epsilon\to 0}\frac{1}{\epsilon}\left(\frac{\kappa_b}{2}\int_0^L \left(\epsilon^2\frac{\partial^2\delta\mathbf{r}}{\partial s^2}\cdot\frac{\partial^2\delta\mathbf{r}}{\partial s^2} + 2\epsilon\frac{\partial^2\mathbf{r}}{\partial s^2}\cdot\frac{\partial^2\delta\mathbf{r}}{\partial s^2}\right)\mathrm{d}s\right) \\
&= \kappa_b\int_0^L \frac{\partial^2\mathbf{r}}{\partial s^2}\cdot\frac{\partial^2\delta\mathbf{r}}{\partial s^2}\mathrm{d}s\ . \qquad (2.70)
\end{aligned}$$

Using integration by parts with variations at the boundary neglected it can be shown that

$$\delta E_b = \kappa_b\int_0^L \frac{\partial^4\mathbf{r}}{\partial s^4}\cdot\delta\mathbf{r}\,\mathrm{d}s\ . \qquad (2.71)$$

Therefore, from (2.69) and (2.72), the bending force density along the rod is equal to

$$\mathbf{f}_b(s,t) = -\kappa_b\frac{\partial^4\mathbf{r}}{\partial s^4}\ . \qquad (2.72)$$

2.4.2 The worm-like chain model

Although the filaments comprising the cytoskeleton are not necessarily considered to be inextensible and can be modeled as elastic rods, as described in the previous section, in this section a model for inextensible semiflexible polymers, the worm-like chain (WLC) model [11], is discussed. The purpose behind this is to derive the theoretical value for the time-averaged contraction of a single immersed inextensible filament in thermal equilibrium. This theoretical value will be used in Section 5.3.1, where it will be verified through numerical simulation.

The WLC model assumes that the filament is inextensible, has a linear elastic bending energy and is subjected to thermal fluctuations. A homogeneous, inextensible and semiflexible filament of straight length L and circular cross section of radius α is taken to be fixed at one end. and free at the other. The domain of the filament is parametried by its arc-length and the position of a typical point is denoted $\mathbf{r}(s)$. The motion of the filament is assumed to be confined to a plane and its bending energy is given by Equation (2.63). Using the Equipartition theorem [47] one can calculate the thermal average angular correlation between distant points along the filament, for which

$$<\mathbf{t}(s)\cdot\mathbf{t}(s')> = e^{-k_BT\frac{|s-s'|}{2L}}\ , \qquad (2.73)$$

where $\mathbf{t}(s) = \frac{\partial \mathbf{r}(s)}{\partial s}$ is the (unit) tangent vector along the filament.

The persistence length l_p is a characteristic length over which the relative orientation of such two tangent vectors along the filament remain correlated, and is defined as $l_p = \frac{2\kappa_b}{k_B T}$. In simple terms, a filament in thermal equilibrium in a fluid will appear rather straight over lengths that are short compared with this persistence length, while it will begin to exhibit a random, contorted shape otherwise.

For the filament under consideration it is assumed that $L \leq l_p$, therefore it is expected to remain nearly straight, with small transverse fluctuations. Let the x-axis define the average orientation of the filament segment, and let u represent the transverse displacement taken to be a function of x and time t. The function $u(x,t)$ may be represented by a Fourier series as

$$u(x,t) = \sum_q u_q \sin(qx) \ . \tag{2.74}$$

where q are the wave vectors defined as $q = n\pi/L$, where $n = 1, 2, 3, ...$, and u_q the corresponding amplitudes. Such a representation is appropriate for the case of a nearly straight filament with boundary conditions $u = 0$ at the end, $x = 0$ and no restraint at $x = L$, as in Figure 2.6.

The local orientation and curvature of the filament are given by the slope $\frac{\partial u}{\partial x}$ and $\frac{\partial^2 u}{\partial x^2}$, respectively. In view of Equations (2.63) and (2.74), the bending energy, as discussed in [49], is given by

$$E_b = \frac{\kappa_b}{2} \int_0^{L(t)} \left(\frac{\partial^2 u}{\partial x^2} \right)^2 dx = \frac{L}{4} \sum_q \kappa_b q^4 u_q^2 \ . \tag{2.75}$$

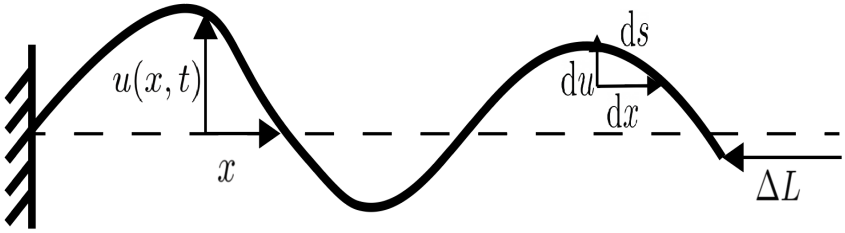

Figure 2.6: *Configuration of filament fixed at one end, where $u(x,t)$ denotes the transverse displacement from an initial straight line (dashed). The magnitude of u is exaggerated for illustration.*

Since the filament is inextensible, the total arc-length of the filament remains unchanged under the influence of the fluctuations. Thus, the arc length ds of a short segment is approximately given by $\sqrt{(dx)^2 + (du)^2} = dx\sqrt{1 + \mid \partial u/\partial x \mid^2}$. The contraction of the chain relative to its full contour length in the presence of thermal

fluctuations in u is then

$$\Delta L \;=\int_0^L\left(1-\frac{\mathrm{d}x}{\mathrm{d}s}\right)\mathrm{d}s=\int_0^L\left(1-\left[\sqrt{1+(\partial u/\partial x)^2}\right]^{-1/2}\right)\mathrm{d}s\;\doteq\frac{1}{2}\int_0^L\left(\frac{\partial u}{\partial x}\right)^2\mathrm{d}x\;, \tag{2.76}$$

where use is made of the approximation $(\sqrt{1+\alpha^2})^{-1}\doteq 1-\frac{1}{2}\alpha^2$, for any α, as well as of the absence of distinction between integrals over the arc-length and its projection on the x-axis. In view of (2.74), the contraction in $(2.76)_3$ is expressed as

$$\Delta L \;=\;\frac{1}{2}\int_0^L\sum_q u_q^2q^2\cos^2(qx)\mathrm{d}x\;=\;\frac{L}{4}\sum_q u_q^2q^2\;. \tag{2.77}$$

In the context of the present problem, if the filament is in equilibrium at temperature T, the ensemble average value $<u_q^2>$ of the amplitude-squared is then deduced in accordance with the canonical distribution [47, Chapter 6], and is expressed as

$$<u_q^2>=\;\frac{\int u_q^2e^{-\beta\frac{L}{4}\sum_q\kappa_bq^4u_q^2}\mathrm{d}u_q}{e^{-\beta\frac{L}{4}\sum_q\kappa_bq^4u_q^2}\mathrm{d}u_q}\;, \tag{2.78}$$

where $\beta=\frac{1}{k_BT}$ and the integral is taken over the phase space of u_q. Setting $q=q_i$, with q_i being the i-th mode of wavelength, one may write

$$\begin{aligned}
<u_{q_i}^2> \;&=\;\frac{\int u_{q_i}^2e^{-\beta\frac{L}{4}\sum_q\kappa_bq^4u_q^2}\mathrm{d}u_q}{\int e^{-\beta\frac{L}{4}\sum_q\kappa_bq^4u_q^2}\mathrm{d}u_q}\\
&=\;\frac{\int u_{q_i}^2e^{-\beta\frac{L}{4}\kappa_bq_i^4u_{q_i}^2}e^{-\beta\frac{L}{4}\sum_{q\neq q_i}\kappa_bq^4u_q^2}\mathrm{d}u_q}{\int e^{-\beta\frac{L}{4}\kappa_bq_i^4u_{q_i}^2}e^{-\beta\frac{L}{4}\sum_{q\neq q_i}\kappa_bq^4u_q^2}\mathrm{d}u_q}\\
&=\;\frac{\int u_{q_i}^2e^{-\beta\frac{L}{4}\kappa_bq_i^4u_{q_i}^2}\mathrm{d}u_{q_i}\int e^{-\beta\frac{L}{4}\sum_{q\neq q_i}\kappa_bq^4u_q^2}\mathrm{d}u_{q\neq q_i}}{\int e^{-\beta\frac{L}{4}\kappa_bq_i^4u_{q_i}^2}\mathrm{d}u_{q_i}\int e^{-\beta\frac{L}{4}\sum_{q\neq q_i}\kappa_bq^4u_q^2}\mathrm{d}u_{q\neq q_i}}\\
&=\;\frac{\int u_{q_i}^2e^{-\beta\frac{L}{4}\kappa_bq_i^4u_{q_i}^2}\mathrm{d}u_{q_i}}{\int e^{-\beta\frac{L}{4}\kappa_bq_i^4u_{q_i}^2}\mathrm{d}u_{q_i}}\\
&=\;\frac{4}{\kappa_bq_i^4L}\left[-\frac{\partial}{\partial\beta}\ln\left(\int e^{-\beta\frac{L}{4}\kappa_bq_i^4u_{q_i}^2}\mathrm{d}u_{q_i}\right)\right]\;,
\end{aligned} \tag{2.79}$$

where q_i stands for the i^{th} mode of wavelength, "ln" denotes the natural logarithm, and introducing the variable $y\;=\;\beta^{1/2}u_q$ it follows that:

$$\int e^{-\beta\frac{L}{4}\kappa_bq_i^4u_{q_i}^2}du_{q_i}\;=\;\beta^{-1/2}\int e^{-\beta\frac{L}{4}\kappa_bq_i^4y^2}dy\;, \tag{2.80}$$

therefore,

$$\ln\left(\int e^{-\beta\frac{L}{4}\kappa_b q_i^4 u_{q_i}^2} du_{q_i}\right) = -\frac{1}{2}\ln\beta + \ln\int e^{-\beta\frac{L}{4}\kappa_b q_i^4 y^2} dy \ , \tag{2.81}$$

and

$$-\frac{\partial}{\partial\beta}\ln\left(\int e^{-\beta\frac{L}{4}\kappa_b q_i^4 u_{q_i}^2} du_{q_i}\right) = \frac{1}{2\beta} \ . \tag{2.82}$$

Therefore, for any q, the ensemble average of the amplitude-squared is written as

$$\begin{aligned} <\mid u_q \mid^2> &= \frac{4}{\kappa_b q^4 L}\frac{1}{2\beta} \\ &= \frac{4}{\kappa_b q^4 L}\frac{k_B T}{2} \\ &= \frac{2k_B T}{\kappa_b q^4 L} \ . \end{aligned} \tag{2.83}$$

in terms of the original length L and the persistence length l_p. Likewise, using Equations (2.77) and (2.83), the ensemble average $< \Delta L >$ of the contraction ΔL is expressed as

$$\begin{aligned} < \Delta L > &= \frac{L}{4}\sum_q < u_q^2 > q^2 \\ &= \frac{L}{4}\sum_q \frac{2k_B T}{L\kappa_b q^4} q^2 \\ &= \frac{k_B T}{2}\sum_q \frac{1}{\kappa_b q^2} \ . \end{aligned} \tag{2.84}$$

It can be observed from Equation (2.84) that the ensemble average of the amplitude-squared of the bending fluctuations diminishes rapidly for higher-order modes due to the (negative) fourth-power dependence on the wave number. Also, Equation (2.84) implies that the longer the persistence length, the smaller the ensemble average of the contraction ΔL.

Equation (2.84) can be rewritten as

$$
\begin{aligned}
< \Delta L > &= \frac{k_B T}{2} \sum_q \frac{1}{\kappa_b q^2} \\
&= \frac{k_B T}{2\kappa_b} \sum_n \left(\frac{l}{n\pi} \right)^2 \\
&= \frac{k_B T L^2}{2\kappa_b \pi^2} \sum_n \frac{1}{n^2} \\
&= \frac{k_B T L^2}{2\kappa_b \pi^2} \frac{\pi^2}{6} \\
&= \frac{k_B T L^2}{12\kappa_b} \\
&= \frac{L^2}{6 l_p} \ , \qquad (2.85)
\end{aligned}
$$

since the persistence length is equal to $l_p = \frac{2\kappa_b}{k_B T}$. Similarly, Equation (2.83) may be rewritten as

$$
<| u_q |^2> = \frac{2 k_B T}{L \kappa_b q^4} = \frac{L^3}{l_p} \frac{4}{n^4 \pi^4} \ . \qquad (2.86)
$$

The probability density function f in Equation (2.49) is independent rendering the ensemble stationary. In this case, the ergodic hypothesis [47, Chapter 15] states then that the ensemble average over all accessible systems is equal to the time average over a large number of observations of a single system. That is, given any observable quantity A in a stationary ensemble, it holds that

$$
< A > = < A >_t = \frac{1}{t} \int_0^t A(\mathbf{\Gamma}(\tau)) \, \mathrm{d}\tau \ , \qquad (2.87)
$$

for large enough observation time t. Therefore, the ensemble averages $< \Delta L >$ and $<| u_q |^2>$ in Equations (2.85) and (2.86) are also time averages for a large enough observation time t.

2.5 Concluding Remarks

In this chapter, the governing equations describing a semiflexible filament immersed in the flow of a Newtonian, incompressible fluid were presented. The Navier-Stokes equations defining the fluid motion were derived. The hydrodynamic fluctuations of the fluid flow were described and a homogenization method [45] was briefly discussed. The behavior of a single semiflexible filament was described, by means of the Euler-Bernoulli beam theory. Lastly, the WLC model was derived, in order

to obtain the theoretical value for the time-averaged contraction of an inextensible filament in thermal equilibrium.

Chapter 3

Artificial Neural Networks

3.1 Overview

Artificial Neural Networks (ANN) are inspired by the way the brain operates: neurons interconnected to other neurons which form a network. A typical neural network has from a few dozen to hundreds, to even millions of artificial neurons called nodes arranged in a series of layers, each of which connects to the layers on either side. Some of these nodes, known as input nodes, are designed to receive various forms of information from the outside world that the network will attempt to learn about, recognize, or otherwise process.

In this chapter, a review of the ANN is presented. The neural networks architecture is introduced in Section 3.2, and the expressive power of ANN is discussed in Section 3.2.1. The training method for ANN is presented in Section 3.3, where the loss function and backpropagation algorithm are discussed, and, lastly, some metrics for model evaluation are described in Section 3.4.

3.2 Neural Networks Architecture

Neural networks are a class of compositional function approximators. In this chapter, the focus is on feedforward neural networks and the content presented is a review of the state-of-the-art based on the notes of Professor A. Sahai [60]. Feedforward are the networks whose computations can be modeled by a Directed Acyclic Graph (DAG) (there are also recurrent neural networks whose computation graphs have cycles). In graph theory, a DAG is a directed graph that has no cycles. That is, it consists of vertices and edges, with each edge directed from one vertex to another, such that following those directions will never form a closed loop [61]. Multilayer perceptron, as shown in Figure 3.1, is the most basic, but still commonly used class of feedforward neural networks. The circles represent nodes, and the nodes are organized into layers. A multilayer perceptron consists of input, hidden and output layers.

The first (left-most) layer in Figure 3.1 is called the input layer, the last (right-most) layer is called the output layer, and any other layers (there is only one here, but there could be multiple) are referred to as hidden layers. The dimensionality of the input and output layers is determined by the function to be computed by the network. For a function from $\mathbb{R}^d$ to $\mathbb{R}^k$, d input nodes and k output nodes are required. The number and sizes of the hidden layers are hyperparameters to be chosen by the network designer.

The layers are considered fully connected, which means that every node in the non-input layers is connected to every node in the previous layer. Each edge in the graph has an associated weight, representing the strength of the connection from the input node in one layer to the node in the next layer. Each node computes a weighted sum of its inputs, with the connection strengths being the weights, and then applies on the weighted sum a nonlinear function, the activation function.

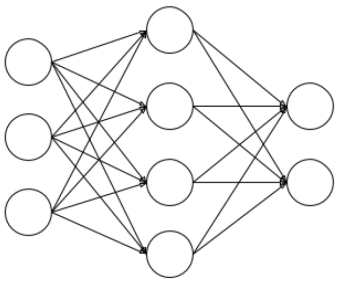

Figure 3.1: *Neural Networks architecture, where the circles represent nodes, and the nodes are organized into fully connected layers [60]*

Concretely, for a node i in layer l, if $\mathbf{w}_i \in \mathbb{R}^{n_{l-1}}$ denotes the weights, where n_{l-1} is the number of nodes in layer $l-1$, and σ_i denotes the activation function of node i, it computes the function

$$\mathbf{x} \to \sigma(\mathbf{w}_i^T \mathbf{x}) \ . \tag{3.1}$$

Let us denote the number of non-input layers by N_L, the number of units in layer $l \in 0, ..., N_L$ by n_l (where n_0 is the size of the input layer), and the activation function for layer $l \in 1, ..., N_L$ by $\sigma_l : \mathbb{R}^{n_l} \to \mathbb{R}^{n_l}$. The weights for every node in layer l can be stacked as rows into a matrix of weights $\mathbf{W}_l \in \mathbb{R}^{n_l} \times \mathbb{R}^{n_{l-1}}$. Then for layer l the computation of the output after applying the activation function on the weighted sum of the input, is given as

$$\mathbf{x} \to \boldsymbol{\sigma}_l(\mathbf{W}_l \mathbf{x}) \ . \tag{3.2}$$

Since the output of each layer is passed as input to the next layer, the function represented by the entire network can be written in a compositional manner as

$$\mathbf{x} \rightarrow \boldsymbol{\sigma}_L(\mathbf{W}_L\boldsymbol{\sigma}_{L-1}(...\boldsymbol{\sigma}_2(\mathbf{W}_2\boldsymbol{\sigma}_1(\mathbf{W}_1\mathbf{x}))...)) \ . \tag{3.3}$$

3.2.1 Expressive power and activation functions

The repeated combination of nonlinearities is what gives deep neural networks their remarkable expressive power. If the activation functions are removed (or equivalently set to the identity function) in Equation (3.3), then the function computed by the network ends up being linear in input since

$$\mathbf{x} \rightarrow \mathbf{W}_L\mathbf{W}_{L-1}...\mathbf{W}_2\mathbf{W}_1\mathbf{x} = \tilde{\mathbf{W}}\mathbf{x} \ . \tag{3.4}$$

The size of the smallest layer restricts the rank of $\tilde{\mathbf{W}}$, as

$$\text{rank}\tilde{\mathbf{W}} \leq \min \text{rank}(\mathbf{W}_l) \leq \min \ n_l \ , \tag{3.5}$$

for $l \in 1, ..., n_L$. However, despite having many layers of computation, this class of networks is not very expressive since it can only represent linear functions. Activation functions different than identity are required in order to produce a class of networks that are universal function approximators, which essentially means that given any continuous function, a network in this class can be chosen such that the output of the circuit can be made arbitrarily close to the output of the given function for all given inputs.

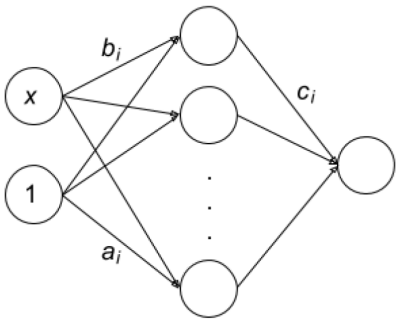

Figure 3.2: *One hidden layer neural network structure [60]*

A one hidden layer is shown in Figure 3.2, where, for simplicity, a one-dimensional input x is assumed. The weight on x to node i is b_i and a constant 1 has been also included to provide bias (the ability to shift its input), whose weight into node i is a_i. The added bias can be thought of as analogous to the role of a constant in a linear function, and the purpose of adding the bias is to customize/shift the input-to-output mapping to suit the particular needs of the problem. The neural network

universal approximation theorem, due to Kurt Hornik [62], says that neural networks are universal function approximators in the following sense.

Assume a function $\sigma\colon\ \mathbb{R} \to \mathbb{R}$ that is nonconstant, bounded, nondecreasing, and continuous, and let $S \subseteq \mathbb{R}_d$ be closed and bounded. Then for any continuous function $f\colon\ S \to \mathbb{R}$ and any $\epsilon > 0$, there exists a neural network with one hidden layer containing finitely many nodes, which can be written as

$$h(\mathbf{x}) \ = \ \sum_{i=1}^{k} c_i \sigma(a_i + \mathbf{b}_i^T \mathbf{x}) \ , \tag{3.6}$$

such that

$$|h(\mathbf{x}) - f(\mathbf{x})| \ < \ \epsilon \ , \tag{3.7}$$

for all $\mathbf{x} \in S$.

Some of the most common activation functions, which are nonconstant, bounded, nondecreasing, and continuous, and are also used in the computations of Section 5.2, are the piecewise-linear rectified linear unit (ReLU) function and the softmax function. The ReLU function, shown in Figure 3.3, is nonlinear and defined as

$$\sigma(x) \ = \ \max\{0, x\} \ . \tag{3.8}$$

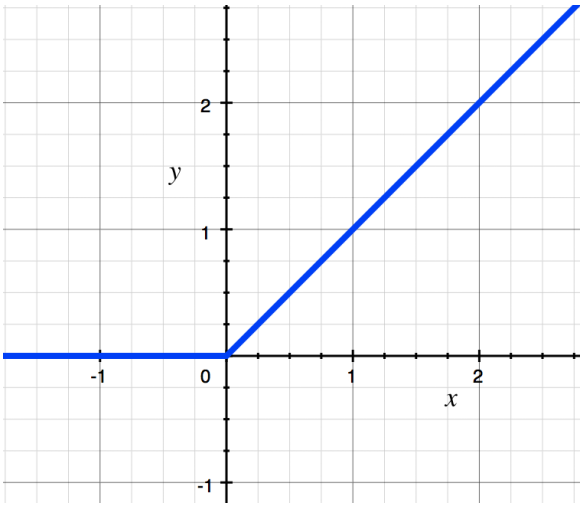

Figure 3.3: *ReLU activation function*

The softmax function $\sigma\colon\ \mathbb{R}^k \to \mathbb{R}^k$, which is usually used to produce a discrete probability distribution over k classes, is defined as

$$\sigma(\mathbf{x})_i \;=\; \frac{e^{x_i}}{\sum_{j=1}^{k} e^{x_j}} \;, \tag{3.9}$$

where $\mathbf{x} \in \mathbb{R}^k$ is the input vector, and $\sum_{j=1}^{k} e^{x_j}$ is the sum of the exponential function applied to each element of the input vector over all the k classes and is used as a normalization term, such that the components of the output vector $\sigma(\mathbf{x})$ are between 0 and 1 and add up to 1.

3.3 Training Neural Networks

In order to make the ANN learn by itself, data are given as input to the model for training purposes. During model training, the input-output pair is fixed, while the weights vary, and the network ends with the loss function. The weights are computed by minimizing the loss function. First-order optimization techniques such as gradient descent and stochastic gradient descent are effective tools for minimizing differentiable loss functions. In order to implement these techniques, the gradient of the loss function with respect to the weights need to be computed. The backpropagation algorithm takes advantage of the directed acyclic graph (DAG) nature of feedforward neural networks to calculate these derivatives efficiently.

3.3.1 Computational graphs

A network can be expressed as a finite directed acyclic graph $G = (V, E)$, sometimes called the computational graph of the network. Each vertex $v_i \in V$ represents the result of some differentiable computation. Each edge represents a computational dependency: there is an edge $(v_i, v_j) \in E$ if and only if the value computed at v_i is used to compute v_j. The set of outgoing neighbors of a node v_i is denoted by

$$\text{out}(v_i) \;=\; \{v_j \in V : (v_i, v_j) \in E\} \;. \tag{3.10}$$

Some of these vertices have special significance; there is a vertex $l \in V$, representing the loss function, which contains no outgoing edges, as shown in Figure 3.4. There is also some subset of vertices $W \subset V$ representing the trainable parameters of the network. The objective is to efficiently calculate $\frac{\partial l}{\partial w_i}$ for each $w_i \in W$.

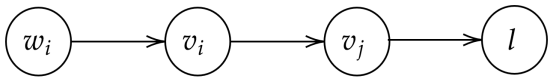

Figure 3.4: *Part of the computational graph of the network*

The chain rule allows us to write

$$\frac{\partial l}{\partial v_i} = \sum_{v_j \in \text{out}(v_i)} \frac{\partial l}{\partial v_j} \frac{\partial v_j}{\partial v_i} \,. \tag{3.11}$$

It can be observed that the value computed at v_i affects potentially all of the vertices to which it is an input, and each of those vertices affects the loss function in some way. The total contribution of v_i to the loss must be summed over these downstream effects. To get an expression for each weight, the above expression can be expanded recursively as

$$\begin{aligned}
\frac{\partial l}{\partial w_i} &= \sum_{v_j \in \text{out}(w_i)} \frac{\partial l}{\partial v_j} \frac{\partial v_j}{\partial w_i} \\
&= \sum_{v_j \in \text{out}(w_i)} \sum_{v_k \in \text{out}(v_j)} \frac{\partial l}{\partial v_k} \frac{\partial v_k}{\partial v_j} \frac{\partial v_j}{\partial w_i} \\
&\vdots \\
&= \sum_{\text{paths } v^{(1)},\ldots,v^{(k)} \text{ from } w_i \text{ to } l} \frac{\partial l}{\partial v^{(k)}} \frac{\partial v^{(k)}}{\partial v^{(k-1)}} \cdots \frac{\partial v^{(2)}}{\partial v^{(1)}} \frac{\partial v^{(1)}}{\partial w_i} \,.
\end{aligned} \tag{3.12}$$

3.3.2 Backpropagation

The backpropagation algorithm combines the chain rule with the principles of dynamic programming, dividing a large problem into simpler subproblems, solving these and storing their solutions, and combining the stored solutions to solve larger subproblems or the original problem. The weights are computed by minimizing the loss function, and, therefore, the large problem is computing $\nabla l(W)$, and the subproblems are computing the individual terms $\frac{\partial l}{\partial w_i}$. It can be observed from the chain rule in Equation (3.12) that work can be reused by computing $\frac{\partial l}{\partial v_i}$ in a "back to front" order. That is, before computing $\frac{\partial l}{\partial v_i}$, $\frac{\partial l}{\partial v_j}$ should be computed for each $v_j \in \text{out}(v_i)$. Because the computational graph is a DAG, such a topological ordering can always and efficiently be computed (in time $O(|V| + |E|)$) via a topological sort. Then computing $\frac{\partial l}{\partial v_i}$ can be easily accomplished by combining the stored values $\frac{\partial l}{\partial v_j}$ with the terms $\frac{\partial v_j}{\partial v_i}$, which can typically be computed analytically based on the knowledge of what mathematical computations each vertex performs.

To get a more concrete sense of what the $\frac{\partial v_j}{\partial v_i}$ terms look like, let us consider a standard fully-connected layer, as shown in Figure 3.5, where each vertex calculates z_j as a linear combination of the activations a_i of the previous layer, with weights w_{ji}:

$$z_j = \sum_i w_{ij} a_i \ , \tag{3.13}$$

where a_i is the result of some computation performed at the previous layer, and these z_j are likely used as inputs to vertices at later layers.

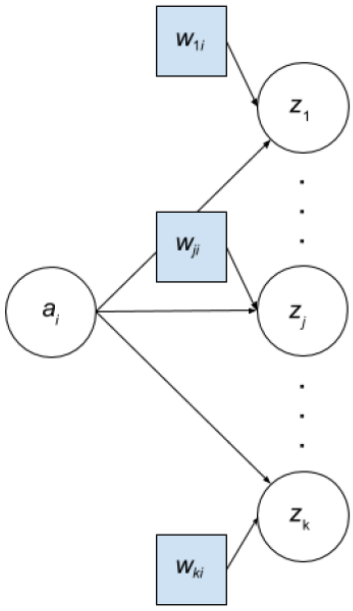

Figure 3.5: *Standard fully-connected layer [60]*

As shown in Figure 3.5, $\text{out}(w_{ij}) = \{z_{ij}\}$, and

$$\frac{\partial z_j}{\partial w_{ji}} = a_i \ , \tag{3.14}$$

so

$$\frac{\partial l}{\partial w_{ji}} = \frac{\partial l}{\partial z_j} a_i \ . \tag{3.15}$$

It can be observed that the activations a_i, that were previously computed in the forward pass, must be used. The derivatives of z_j with respect to a_i must also be computed as

$$\frac{\partial z_j}{\partial a_i} = w_{ji} \ , \tag{3.16}$$

so

$$\frac{\partial l}{\partial a_i} = \sum_{j=1}^{k} \frac{\partial l}{\partial z_j} w_{ji} \ , \tag{3.17}$$

so it can be passed backward to the earlier layer.

After taking linear combinations, nonlinearity needs to be inserted through the activation functions. In most cases, this nonlinearity is applied elementwise as

$$a_i = \sigma(z_i) \ , \tag{3.18}$$

where z_i is the value from the previous layer, and σ is the activation function. It is straightforward to see that

$$\frac{\partial a_i}{\partial z_i} = \sigma'(z_i) \ , \tag{3.19}$$

so

$$\frac{\partial l}{\partial z_i} = \frac{\partial l}{\partial a_i} \sigma'(z_i) \ . \tag{3.20}$$

3.3.3 Loss function

As stated in the previous section, the weights of the network are computed by minimizing the loss function, which is a function measuring how good the predictions are. A large loss indicates bad prediction and, therefore, poor performance of the model. The choice of the loss function depends on the type of the prediction problem in hand each time. For multi-class classification problems, which is the type of the prediction problem discussed in Section 5.2, one the most common loss functions is the cross-entropy loss function. The cross-entropy function calculates a score that summarizes the average difference between the actual and predicted probability distributions for all classes. The score is minimized and a perfect cross-entropy value is 0. The cross-entropy loss function is defined as

$$l_{CE} = -\sum_{i=1}^{k} y_i \log(\hat{y}_i) \ , \tag{3.21}$$

where k is the total number of classes, y_i is the true probability for each class i and $\hat{y}_i$ is the predicted probability for each class i.

3.4 Model evaluation metrics for classification

Evaluating the machine learning algorithm is essential. Again, the choice of the metrics for evaluation of the model depends on the type of the prediction problem in hand each time. Some of the most commonly used metrics for multi-class classification, which are also used for the evaluation of the performance of the ANN model in Section 5.2, are presented in this section.

The accuracy metric [63] for a binary classification problem is defined as

$$\begin{aligned} \text{Accuracy} &= \frac{\text{Number of correct predictions}}{\text{Total number of predictions}}, \\ &= \frac{\text{TP} + \text{TN}}{\text{TP} + \text{TN} + \text{FP} + \text{FN}}, \end{aligned} \tag{3.22}$$

where TP = True Positives, TN = True Negatives, FP = FalsePositive, and FN = False Negatives. For a multi-class classification, a categorical accuracy is defined as

$$\text{Categorical Accuracy} = \frac{\sum_{i=1}^{k}(\text{TP}_i + \text{TN}_i)}{\sum_{i=1}^{k}(\text{TP}_i + \text{TN}_i + \text{FP}_i + \text{FN}_i)}, \tag{3.23}$$

where k denotes the total number of classes.

With ANN and the use of the softmax activation function (3.9) in the output layer for a multi-class classification problem, the probabilities of each input element belonging to a class label are obtained at the end of the calculations. The decision for converting a predicted probability into a class label is known as decision threshold. Different threshold values result in different true positive rate (TPR), also known as sensitivity, and a different false positive rate (FPR) of the model and some thresholds will probably give a better result than others, depending on whether the focus is to lower the TPR or the FPR.

The TPR tells what proportion of the positive class got correctly classified and is defined as

$$\text{TPR} = \frac{\text{TP}}{\text{TP} + \text{FN}}. \tag{3.24}$$

The FPR tells what proportion of the negative class got incorrectly classified by the classifier and is defined as

$$\text{FPR} = \frac{\text{FP}}{\text{FP} + \text{TN}}. \tag{3.25}$$

The Receiver Operator Characteristic (ROC) curve [64] is an evaluation metric for classification. It is a probability curve that plots the TPR against the FPR at various decision threshold values. In the case of the multi-class classification, the ROC curve is generated for each of the class labels by classifying the class i against

all the other classes that are not class i.

The ROC curve is independent of the class distribution in the dataset and can be used to compare the performance across different classifiers, as shown in Figure 3.6.

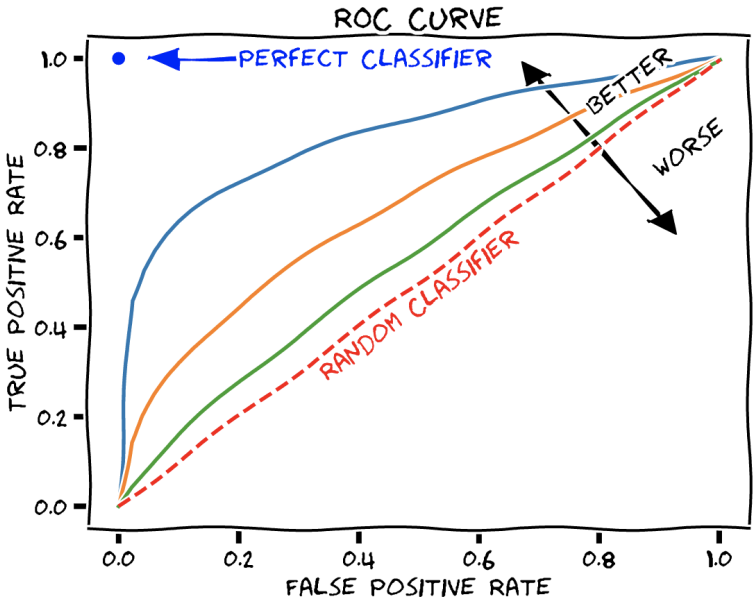

Figure 3.6: *Comparing ROC curves across classifiers [65]*

Another metric is the Area Under the Curve (AUC) which is used to measure the ability of a classifier to distinguish between classes and is used as a summary of the ROC curve. AUC is classification-threshold-invariant, *i.e.*, it measures the quality of the model's predictions irrespective of what classification threshold is selected. One way of interpreting AUC is as the probability that the model ranks a random positive example more highly than a random negative example, where for a multi-class classification positive means belonging to a specific class label. Since AUC measures how well predictions are ranked, rather than their absolute values, it can be concluded that it is scale-invariant. AUC ranges in value from 0 to 1. The higher the AUC value for a classifier, the better its ability to distinguish between positive and negative classes, *i.e.*, a model whose predictions are 100% wrong has an AUC of 0 and one whose predictions are 100 % correct has an AUC of 1.

3.5 Concluding Remarks

In this chapter, a review of the ANN was presented. The Neural Networks architecture was described in Section 3.2 and the expressive power of ANN was discussed

in Section 3.2.1. The training method for ANN was presented in Section 3.3, where the loss function and backpropagation algorithm were discussed, and, lastly, some metrics for model evaluation were described in Section 3.4.

Chapter 4

Finite Element Approximation

4.1 Overview

This chapter presents the Immersed Boundary Method (IBM) in Section 4.2, which is intended for the computer simulation of fluid-structure interaction. Its numerical solution strategy, that accounts for a two-way coupling between the immersed boundary and the fluid, is derived in Chapter 2. The IBM, as described in [32], combines the Navier-Stokes equations and the Euler beam theory. An extended IBM is proposed, which additionally accounts for the hydrodynamic thermal fluctuations in the fluid by including a stochastic stress tensor in the Navier-Stokes equations. The string form of the IBM formulation is described in Section 4.2.1 and its weak form is derived in Section 4.2.2 using a weighted-residual formulation. The spatially and temporally discretized weighted residuals are presented in Section 4.2.3. The summary of the proposed extended numerical algorithm for simulating flexible filaments immersed in a thermally fluctuating fluid is described in Section 4.2.4. Additionally, the Coarse-Graining Method (CGM) for modeling the elastohydrodynamic behavior of inextensible filaments is described in Section 4.3. The CGM models the inextensible filament by discretizing it into a number of inextensible straight segments and the elastic interaction coupling neighboring nodes/joints is described via discrete elastic connectors encoding the filament's resistance to bending. Using the linear and angular momentum balance, the equations describing the elastohydrodynamic behavior of inextensible filaments are derived and further extended to account for the two-way coupling between the inextensible filament and the fluid. Lastly, a hybrid IBM/CGM algorithm is proposed in Section 4.3.3.

4.2 Immersed Boundary Method

The IBM [32] is intended for the computer simulation of fluid-structure interaction, especially in biological fluid dynamics, where the motion of the immersed

structure can induce the fluid flow motion and vice versa. The mathematical formulation of IBM employs both Eulerian and Lagrangian variables, linked by the Dirac delta function through interaction equations. The spatial discretization of the IBM equations is based on a fixed Cartesian mesh for the Eulerian variables, and a moving curvilinear mesh for the Lagrangian variables.

4.2.1 Equations of motion

Let us consider a massless elastic curve Γ_t immersed in an incompressible, Newtonian fluid occupying a two-dimensional domain Ω. The domain Ω undergoes thermal fluctuations. The fluid and the curve constitute a coupled mechanical system. The massless curve's motion is determined by that of the fluid, but at the same time the curve exerts force on the fluid and affects its motion. The Lagrangian form of the curve is given by the function $\mathbf{y}(s,t)$ for $0 \leq s \leq L$. The IBM formulation in its strong form can be understood as an enrichment of the two-dimensional Navier-Stokes equations on a fixed Cartesian mesh for the Eulerian variables, accounting also for the forces generated by the elastic response of the immersed body. Specifically, in the absence of body forces, the initial/bounary-value problem to be solved may be formulated as:

Find $\mathbf{v} : \Omega \times (0,T] \to \mathbb{R}^2$, $p : \Omega \times (0,T] \to \mathbb{R}$ and $\mathbf{y} : [0, L(t)] \times (0,T] \to \Omega$ which satisfy

$$
\begin{aligned}
-\operatorname{grad} p + \mu \operatorname{div}\operatorname{grad}\mathbf{v} + \operatorname{div}\tilde{\mathbf{S}} + \mathbf{F} &= \rho\frac{\partial \mathbf{v}}{\partial t} && \text{in } \Omega \times (0,T]\ , \\
\operatorname{div}\mathbf{v} &= 0 && \text{in } \Omega \times (0,T]\ , \\
\mathbf{v}(\mathbf{x},t) &= \bar{\mathbf{v}} && \text{on } \partial\Omega \times (0,T]\ , \\
\mathbf{v}(\mathbf{x},0) &= \mathbf{v}_0 && \text{in } \Omega\ , \\
\mathbf{F}(\mathbf{x},t) &= \int_0^{L(t)} \mathbf{f}(s,t)\,\delta(\mathbf{x}-\mathbf{y}(s,t))\,\mathrm{d}s && \forall \mathbf{y} \in \Omega,\ t \in (0,T]\ , \\
\frac{\partial \mathbf{y}}{\partial t} &= \mathbf{v}(\mathbf{y}(s,t),t) && \forall s \in [0, L(t)],\ t \in (0,T]\ , \\
\mathbf{y}(s,0) &= \mathbf{y}_0(s) && \forall s \in [0, L(t)]\ ,
\end{aligned}
\tag{4.1}
$$

where $\tilde{\mathbf{S}}$ is the stochastic stress tensor that accounts for the thermal fluctuations in the fluid and satisfies the equations $(2.48)_1$ and $(2.48)_2$, $\bar{\mathbf{v}}$ is the time-dependent Dirichlet boundary condition for velocity on $\partial\Omega$, $\mathbf{v}_0$ and $\mathbf{y}_0$ are the prescribed initial velocity field and position for Ω and Γ_t, respectively, and $\mathbf{f}(s,t)$ is the force density that the immersed curve exerts on the fluid and is given by (2.67) and (2.72) as

$$\begin{aligned}\mathbf{f} &= \mathbf{f}_s(s,t) + \mathbf{f}_b(s,t) \\ &= \kappa_s \frac{\partial}{\partial s}\left[\left(\left|\frac{\partial \mathbf{y}}{\partial s}\right| - 1\right)\frac{\frac{\partial \mathbf{y}}{\partial s}}{\left|\frac{\partial \mathbf{y}}{\partial s}\right|}\right] - \kappa_b \frac{\partial^4 \mathbf{y}}{\partial s^4} \ . \end{aligned} \tag{4.2}$$

4.2.2 Weak Forms

The weak form of the preceding initial/boundary-value problem results from the general weighted-residual statement [51]

$$\int_{\Omega\times(0,T]} \mathbf{w} \cdot \left[-\operatorname{grad} p + \mu \operatorname{div}\operatorname{grad}\mathbf{v} + \operatorname{div}\tilde{\mathbf{S}} + \mathbf{F} - \rho\frac{\partial \mathbf{v}}{\partial t}\right] \mathrm{d}\Omega\, \mathrm{d}t + \int_{\Omega\times(0,T]} q \operatorname{div}\mathbf{v}\, \mathrm{d}\Omega\, \mathrm{d}t = 0 \ , \tag{4.3}$$

where the weighting functions $(\mathbf{w}, q)$ belong to $\mathcal{W}\times\mathcal{Q}$ with

$$\begin{aligned}\mathcal{W} &= \left\{\mathbf{w}\in H^1(\Omega) \mid \mathbf{w} = \mathbf{0} \text{ on } \partial\Omega \ , \ \mathbf{w}(\mathbf{x},0) = \mathbf{0}\right\} \ , \\ \mathcal{Q} &= \left\{q \in H^0(\Omega)\right\} \ . \end{aligned} \tag{4.4}$$

where $H^1(\Omega)$ is the Sobolev space of all vector functions with square-integrable first derivatives and $H^0(\Omega)$ is the Sobolev space of all vector functions that are square-integrable.

Equation (4.3) involves a space-time integral. Since the spatial and temporal dimensions are independent of each other, the corresponding integrals may be readily decoupled, and, after using integration by parts, the weak form becomes

$$\int_{(0,T]}\left[\int_\Omega \mathbf{w}\cdot\rho\frac{\partial\mathbf{v}}{\partial t}\,\mathrm{d}\Omega + \int_\Omega \operatorname{grad}\mathbf{w}\cdot\mu\operatorname{grad}\mathbf{v}\,\mathrm{d}\Omega - \int_\Omega p\operatorname{div}\mathbf{w}\,\mathrm{d}\Omega - \int_\Omega q\operatorname{div}\mathbf{v}\,\mathrm{d}\Omega\right]\mathrm{d}t = \int_{(0,T]}\left[\int_\Omega \mathbf{w}\cdot\mathbf{F}\,\mathrm{d}\Omega + \int_\Omega \operatorname{grad}\mathbf{w}\cdot\tilde{\mathbf{S}}\,\mathrm{d}\Omega\right]\mathrm{d}t \ . \tag{4.5}$$

The first term on the right-hand side of (4.5) becomes with $(4.1)_5$

$$\begin{aligned}\int_\Omega \mathbf{w}\cdot\mathbf{F}\,\mathrm{d}\Omega &= \int_\Omega \mathbf{w}\int_0^{L(t)} \mathbf{f}(s,t)\,\delta(\mathbf{x}-\mathbf{y}(s,t))\,\mathrm{d}s\,\mathrm{d}\Omega \\ &= \int_0^{L(t)} \mathbf{f}(s,t)\cdot\mathbf{w}(\mathbf{y}(s,t))\,\mathrm{d}s \ . \end{aligned}$$

The weighted-residual amounts to finding $(\mathbf{v}, p) \in \mathcal{V} \times \mathcal{P}$, such that the weak form holds for all $(\mathbf{w}, q) \in \mathcal{W} \times \mathcal{Q}$. The spaces of admissible displacements and pressures are

$$\begin{aligned} \mathcal{V} &= \left\{ \mathbf{v} \in H^1(\Omega) \mid \mathbf{v} = \bar{\mathbf{v}} \text{ on } \partial\Omega \,,\; \mathbf{u}(\mathbf{x}, 0) = \mathbf{u_0} \right\} \,, \\ \mathcal{P} &= \left\{ p \in H^0(\Omega) \right\} \,. \end{aligned} \tag{4.6}$$

4.2.3 Discretization

4.2.3.1 Spatial Discretization

A finite-dimensional Bubnov-Galerkin approximation of (4.5) is obtained, after defining discrete admissible fields $\mathcal{V}_h \subset \mathcal{V}$, $\mathcal{W}_h \subset \mathcal{W}$, $\mathcal{Q}_h \subset \mathcal{Q}$ and $\mathcal{P}_h \subset \mathcal{P}$, by restating the weak form as follows

$$\begin{aligned} &\int_{(0,T]} \left[\int_\Omega \mathbf{w}_h \cdot \rho \frac{\partial \mathbf{v}_h}{\partial t} \, \mathrm{d}\Omega + \int_\Omega \operatorname{grad} \mathbf{w}_h \cdot \mu \operatorname{grad} \mathbf{v}_h \, \mathrm{d}\Omega - \int_\Omega p_h \operatorname{div} \mathbf{w}_h \, \mathrm{d}\Omega \right. \\ &\left. - \int_\Omega q_h \operatorname{div} \mathbf{v}_h \, \mathrm{d}\Omega \right] dt = \int_{(0,T]} \left[\int_0^{L(t)} \mathbf{f}(s,t) \cdot \mathbf{w}_h(\mathbf{y}(s,t)) \, \mathrm{d}s + \int_\Omega \operatorname{grad} \mathbf{w}_h \cdot \tilde{\mathbf{S}} \, \mathrm{d}\Omega \right] dt \,, \end{aligned} \tag{4.7}$$

where $\mathcal{V}_h$, $\mathcal{W}_h$, $\mathcal{P}_h$ and $\mathcal{Q}_h$ are subspaces of $\mathcal{V}$, $\mathcal{W}$, $\mathcal{P}$ and $\mathcal{Q}$, respectively so that within a given finite element e with domain Ω_e, it holds that

$$\begin{aligned} \mathbf{v}^e(\mathbf{x}, t) \doteq \mathbf{v}_h^e &= \sum_{i\,=\,1}^{N_v} N_i^e(\mathbf{x}) \mathbf{v}_i^e(t) \,, \\ \mathbf{w}^e(\mathbf{x}, t) \doteq \mathbf{w}_h^e &= \sum_{i\,=\,1}^{N_v} N_i^e(\mathbf{x}) \mathbf{w}_i^e(t) \,, \\ p^e(\mathbf{x}, t) \doteq p_h^e &= \sum_{i\,=\,1}^{N_p} \Phi_i^e p_i^e(t) \,, \\ q^e(\mathbf{x}, t) \doteq q_h^e &= \sum_{i\,=\,1}^{N_p} \Phi_i^e q_i^e(t) \,, \end{aligned} \tag{4.8}$$

where N_i^e and Φ_i^e are the element interpolation functions for velocity and pressure, respectively, and N_v and N_p are the number of element nodes for velocity and pressure, respectively. Also $N_i(\mathbf{x}) = 0$ on $\partial\Omega$ and $\mathbf{v}_i(0) = \mathbf{w}_i(0) = \mathbf{0}$. Equations (4.8) can be written compactly as

$$\begin{aligned} \mathbf{v}_h &= [\mathbf{N}^e]\,[\mathbf{v}^e]\ , \\ \mathbf{w}_h &= [\mathbf{N}^e]\,[\mathbf{w}^e]\ , \\ p_h &= [\mathbf{\Phi}^e]\,[\mathbf{p}^e]\ , \\ q_h &= [\mathbf{\Phi}^e]\,[\mathbf{q}^e]\ , \end{aligned} \tag{4.9}$$

where $[\mathbf{v}^e]$, $[\mathbf{w}^e]$, $[\mathbf{p}^e]$, and $[\mathbf{q}^e]$ are vectors comprised of the element nodal values and

$$\begin{aligned} [\mathbf{N}^e] &= \begin{bmatrix} N_1^e & 0 & N_2^e & 0 & \cdots & N_{N_v}^e & 0 \\ 0 & N_1^e & 0 & N_2^e & \cdots & 0 & N_{N_v}^e \end{bmatrix}\ , \\ [\mathbf{\Phi}^e] &= \begin{bmatrix} \Phi_1^e & \Phi_2^e & \cdots & \Phi_{N_p}^e \end{bmatrix}\ . \end{aligned} \tag{4.10}$$

Upon substitution of $\mathbf{v}_h$, $\mathbf{w}_h$, p_h and q_h in the weak form (4.7), and, considerate of the arbitrariness of $[\mathbf{w}^e]$ and $[\mathbf{p}^e]$, the spatial discretization leads to a coupled linear system of equations for the solution vectors $[\mathbf{v}^e]$ and $[\mathbf{p}^e]$

$$\begin{bmatrix} [\mathbf{M}] & [\mathbf{0}] \\ [\mathbf{0}] & [\mathbf{0}] \end{bmatrix} \begin{bmatrix} [\dot{\mathbf{v}}^e] \\ [\dot{\mathbf{p}}^e] \end{bmatrix} + \begin{bmatrix} [\mathbf{K}_{vv}] & [\mathbf{K}_{vp}] \\ [\mathbf{K}_{pv}] & [\mathbf{0}] \end{bmatrix} \begin{bmatrix} [\mathbf{v}^e] \\ [\mathbf{p}^e] \end{bmatrix} = [\mathbf{F}^{IC}] + [\mathbf{F}^{th}]\ , \tag{4.11}$$

where

$$\begin{aligned} [\mathbf{M}] &= \int_{\Omega^e} [\mathbf{N}^e]^T \rho [\mathbf{N}^e]\ \mathrm{d}\Omega\ , \\ [\mathbf{K}_{vv}] &= \int_{\Omega^e} [\mathbf{B}^e]^T \mu [\mathbf{B}^e]\ \mathrm{d}\Omega\ , \\ [\mathbf{K}_{vp}] &= -\int_{\Omega^e} [\mathbf{\Delta}^e]^T [\mathbf{\Phi}^e]\ \mathrm{d}\Omega\ , \\ [\mathbf{K}_{pv}] &= -\int_{\Omega^e} [\mathbf{\Delta}^e]^T [\mathbf{\Phi}^e]\ \mathrm{d}\Omega\ , \\ [\mathbf{F}^{IC}] &= \int_0^{L(t)} [\mathbf{N}^e(\mathbf{y}(s,t)]^T [\mathbf{f}(s,t)]\ \mathrm{d}s, \\ [\mathbf{F}^{th}] &= \int_{\Omega^e} [\mathbf{B}^e]^T [\tilde{\mathbf{S}}]\ \mathrm{d}\Omega\ , \end{aligned} \tag{4.12}$$

and $[\mathbf{F}^{IC}]$ and $[\mathbf{F}^{th}]$ are the forces due to the immersed body and the thermal fluctuations of the fluid, respectively, $[\mathbf{\Delta}^e]$ is the divergence operator acting on $[\mathbf{N}^e]$ defined as

$$[\mathbf{\Delta}^e] = \begin{bmatrix} \frac{dN_1^e}{dx_1} & \frac{dN_1^e}{dx_2} & \cdots & \frac{dN_{N_v}^e}{dx_1} & \frac{dN_{N_v}^e}{dx_2} \end{bmatrix}\ , \tag{4.13}$$

and $[\mathbf{B}^e]$ is a gradient operator acting on $[\mathbf{N}^e]$ defined as

$$[\mathbf{B}^e] \;=\; \begin{bmatrix} \frac{dN_1^e}{dx_1} & 0 & \cdots & \frac{dN_{N_v}^e}{dx_1} & 0 \\ 0 & \frac{dN_1^e}{dx_2} & \cdots & 0 & \frac{dN_{N_v}^e}{dx_2} \\ \frac{dN_1^e}{dx_2} & \frac{dN_1^e}{dx_1} & \cdots & \frac{dN_{N_v}^e}{dx_2} & \frac{dN_{N_v}^e}{dx_1} \end{bmatrix} . \tag{4.14}$$

The immersed curve is divided in N equal segments. Let $s_i,\ i = 0,...,N$ with $s_0 = 0$ and $s_N = L(t)$, be $N+1$ distinct points of the interval $[0, L(t)]$. Set $h_i = \mid s_{i+1} - s_i \mid$ for $i = 0,...,N-1$, and, use the notation $\mathbf{y_i} = \mathbf{y}(s_i)$ for $i = 0,...,N$. In the asymptotic limit of small, but finite, nonzero h_i, the force due to the immersed curve $[\mathbf{F}^{IC}]$ in $(4.12)_5$ can be written via a Riemann sum as

$$\begin{aligned} [\mathbf{F}^{IC}] \;&=\; \int_0^{L(t)} [\mathbf{N}^e(\mathbf{y}(s,t)]^T [\mathbf{f}(s,t)]\ \mathrm{d}s \\ &= \int_{s_0}^{s_0+\frac{h_0}{2}} [\mathbf{N}^e(\mathbf{y}(s,t)]^T [\mathbf{f}(s,t)]\ \mathrm{d}s \\ &+ \sum_{i\,=\,1}^{N-1} \int_{s_i-\frac{h_{i-1}}{2}}^{s_i+\frac{h_i}{2}} [\mathbf{N}^e(\mathbf{y}(s,t)]^T [\mathbf{f}(s,t)]\ \mathrm{d}s + \int_{s_N-\frac{h_{N-1}}{2}}^{s_N} [\mathbf{N}^e(\mathbf{y}(s,t)]^T [\mathbf{f}(s,t)]\ \mathrm{d}s\ , \end{aligned} \tag{4.15}$$

and, assuming that at a distinct point i the term $[\mathbf{N}^e(\mathbf{y}(s,t)]^T[\mathbf{f}(s,t)] = [\mathbf{N}^e(\mathbf{y}_i)]^T[\mathbf{f}(s_i,t)]$ is constant along half of the segment ahead and half of the element behind, the force due to the immersed curve $[\mathbf{F}^{IC}]$ can be written as

$$\begin{aligned} [\mathbf{F}^{IC}] \;=\; \frac{h_0}{2}[\mathbf{N}^e(\mathbf{y}_0)]^T[\mathbf{f}(s_0,t)]\ \delta_{\mathbf{y}_0\in\Omega_e} + \sum_{i\,=\,1}^{N-1} \left(\frac{h_{i-1}}{2} + \frac{h_i}{2}\right)[\mathbf{N}^e(\mathbf{y})_i]^T[\mathbf{f}(s_i,t)]\ \delta_{\mathbf{y}_i\in\Omega_e} \\ + \frac{h_{N-1}}{2}[\mathbf{N}^e(\mathbf{y})_N]^T[\mathbf{f}(s_N,t)]\ \delta_{\mathbf{y}_N\in\Omega_e}\ , \end{aligned} \tag{4.16}$$

where $\delta_{\mathbf{y}_i\in\Omega_e}$ is equal to 1 if point $\mathbf{y}_i \in \Omega_e$, otherwise is equal to 0.

The force density of the immersed curve $\mathbf{f}(s_i,t)$, as defined in (4.2), is discretized with the Finite Difference method. The first derivative of the central finite difference approximation for unequal sub-intervals is equal to

$$\frac{\partial \mathbf{y}_i}{\partial s} \doteq \frac{\mathbf{y}_{i+1} - \mathbf{y}_{i-1}}{h_{i-1} + h_i}\ , \tag{4.17}$$

which, for equally sized discrete segments h, degenerates to the known second-order accurate central finite difference scheme $\frac{\partial \mathbf{y}_i}{\partial s} \doteq \frac{\mathbf{y}_{i+1}-\mathbf{y}_{i-1}}{2h}$.

The fourth derivative of the finite difference approximation for unequal subintervals is derived with Lagrange's interpolation formula in [52] and is equal to

$$\frac{\partial^4 \mathbf{y}_i}{\partial s^4} \doteq \frac{4}{h_i h_{i-1}(h_i + h_{i-1})}\left[\left(\frac{h_i}{h_{i-2}(h_{i-1}+h_{i-2})}\right)\mathbf{y}_{i-2} - \left(\frac{1}{h_i} + \frac{h_i}{h_{i-1}h_{i-2}}\right)\mathbf{y}_{i-1} + \left(\frac{1}{h_i + h_{i+1}} + \frac{h_i + h_{i-1}}{h_i h_{i-1}} + \frac{h_i}{h_{i-1}(h_{i-1}+h_{i-2})}\right)\mathbf{y}_i - \left(\frac{h_i + h_{i+1}}{h_i h_{i+1}}\right)\mathbf{y}_{i+1} + \left(\frac{h_i}{h_{i+1}(h_i + h_{i+1})}\right)\mathbf{y}_{i+2}\right], \tag{4.18}$$

which, for equally sized discrete segments h, degenerates to the known second-order accurate central finite difference scheme $\frac{\partial^4 \mathbf{y}_i}{\partial s^4} \doteq \frac{\mathbf{y}_{i+2} - 4\mathbf{y}_{i+1} + 6\mathbf{y}_i - 4\mathbf{y}_{i-1} + \mathbf{y}_{i-2}}{h^4}$.

There exist many choices for representing the stochastic stress tensor $\tilde{\mathbf{S}}$ in Equation $(4.1)_1$ [53]. As suggested in [54–57], a formulation for the stochastic stress tensor $\tilde{\mathbf{S}}$ that requires the fewest possible random numbers and satisfies the fluctuation dissipation theorem [44] and Equation (2.48), is expressed as

$$\tilde{\mathbf{S}} = \begin{cases} \sqrt{\frac{4k_B T\mu}{\Delta V \Delta t}}\tilde{\mathbf{R}}, & \text{if } i = j \\ \sqrt{\frac{2k_B T\mu}{\Delta V \Delta t}}\tilde{\mathbf{R}}, & \text{otherwise} \end{cases}, \tag{4.19}$$

where $\Delta V = \frac{V}{nel} = \text{vol}(\Omega_e)$, with V the volume of the fluid domain Ω, nel the total number of elements in the Eulerian spatial discretization of the fluid, and Ω_e is the domain of element e used in this (uniform) discretization. The tensor $\tilde{\mathbf{R}}$ is symmetric, by its definition as $\tilde{\mathbf{R}} = \frac{\mathbf{R}+\mathbf{R}^T}{2}$, where a realization of $\mathbf{R}$ is sampled with a stream of independent, standard normally distributed random numbers at each time step Δt for every element Ω_e of the fluid domain.

The global solution of the fields $[\mathbf{v}]$ and $[\mathbf{p}]$ results for the entire finite-element domain through an assembly of Equations (4.11) for each Ω^e. The global system of equations for the fields $[\mathbf{v}]$ and $[\mathbf{p}]$, after assembly of the total number of elements nel, is

$$\begin{bmatrix} [\mathbf{M}] & [\mathbf{0}] \\ [\mathbf{0}] & [\mathbf{0}] \end{bmatrix} \begin{bmatrix} [\dot{\mathbf{v}}] \\ [\dot{\mathbf{p}}] \end{bmatrix} + \begin{bmatrix} [\mathbf{K}_{vv}] & [\mathbf{K}_{vp}] \\ [\mathbf{K}_{pv}] & [\mathbf{0}] \end{bmatrix} \begin{bmatrix} [\mathbf{v}] \\ [\mathbf{p}] \end{bmatrix} = [\mathbf{F}^{IC}] + [\mathbf{F}^{th}], \tag{4.20}$$

with the assembled global matrices defined as

$$
\begin{aligned}
[\mathbf{M}] &= \mathop{\mathrm{A}}_{e=1}^{nel} \int_{\Omega^e} [\mathbf{N}^e]^T \rho [\mathbf{N}^e] \, \mathrm{d}\Omega \ , \\
[\mathbf{K}_{vv}] &= \mathop{\mathrm{A}}_{e=1}^{nel} \int_{\Omega^e} [\mathbf{B}^e]^T \mu [\mathbf{B}^e] \, \mathrm{d}\Omega \ , \\
[\mathbf{K}_{vp}] &= -\mathop{\mathrm{A}}_{e=1}^{nel} \int_{\Omega^e} [\boldsymbol{\Delta}^e]^T [\boldsymbol{\Phi}] \, \mathrm{d}\Omega \ , \\
[\mathbf{K}_{pv}] &= -\mathop{\mathrm{A}}_{e=1}^{nel} \int_{\Omega^e} [\boldsymbol{\Delta}^e]^T [\boldsymbol{\Phi}] \, \mathrm{d}\Omega \ , \\
[\mathbf{F}^{IC}] &= \mathop{\mathrm{A}}_{e=1}^{nel} \Big[\frac{h_0}{2} [\mathbf{N^e}(\mathbf{y}_0)]^T [\mathbf{f}(s_0,t)] \, \delta_{\mathbf{y}_0 \in \Omega_e} + \sum_{i=1}^{N-1} \Big(\frac{h_{i-1}}{2} + \frac{h_i}{2} \Big) [\mathbf{N^e}(\mathbf{y}_i)]^T [\mathbf{f}(s_i,t)] \, \delta_{\mathbf{y}_i \in \Omega_e} \\
&\quad + \frac{h_{N-1}}{2} [\mathbf{N^e}(\mathbf{y}_N)]^T [\mathbf{f}(s_N,t)] \, \delta_{\mathbf{y}_N \in \Omega_e} \Big] \ , \\
[\mathbf{F}^{th}] &= \mathop{\mathrm{A}}_{e=1}^{nel} \int_{\Omega^e} [\mathbf{B}^e]^T [\tilde{\mathbf{S}}] \, \mathrm{d}\Omega \ .
\end{aligned}
\tag{4.21}
$$

4.2.3.2 Temporal Discretization

The global system of equations in (4.20) is subsequently integrated in time with the backward Euler method, according to which the time derivative $\dot{\mathbf{v}}$ can be approximated at time t_n by a Taylor series expansion of $\mathbf{v}(t)$ around $t = t_{n+1}$ as

$$
\mathbf{v}^n = \mathbf{v}^{n+1} - \Delta t_n \dot{\mathbf{v}}^{n+1} + O(\Delta t_n^2) \ , \tag{4.22}
$$

with the simplified notation, $\mathbf{v}^n = \mathbf{v}(t_n)$ and $\dot{\mathbf{v}}^n = \dot{\mathbf{v}}(t_n)$. Upon ignoring the second-order term in $\Delta t_n = t_{n+1} - t_n$, the preceding equation leads to

$$
\dot{\mathbf{v}}^{n+1} \doteq \frac{\mathbf{v}^{n+1} - \mathbf{v}^n}{\Delta t_n} \ . \tag{4.23}
$$

Writing now the global system of equations in (4.20) at t_{n+1} and substituting $\dot{\mathbf{v}}^{n+1}$ from (4.23), results in

$$
\begin{aligned}
&\begin{bmatrix} \frac{[\mathbf{M}]}{\Delta t_n} & [\mathbf{0}] \\ [\mathbf{0}] & [\mathbf{0}] \end{bmatrix} \begin{bmatrix} [\mathbf{v}^{n+1}] \\ [\mathbf{p}^{n+1}] \end{bmatrix} + \begin{bmatrix} [\mathbf{K}_{vv}] & [\mathbf{K}_{vp}] \\ [\mathbf{K}_{pv}] & [\mathbf{0}] \end{bmatrix} \begin{bmatrix} [\mathbf{v}^{n+1}] \\ [\mathbf{p}^{n+1}] \end{bmatrix} \\
&\qquad = \begin{bmatrix} \frac{[\mathbf{M}]}{\Delta t_n} & [\mathbf{0}] \\ [\mathbf{0}] & [\mathbf{0}] \end{bmatrix} \begin{bmatrix} [\mathbf{v}^n] \\ [\mathbf{0}] \end{bmatrix} + [\mathbf{F}^{IC,n}] + [\mathbf{F}^{th,n}] \ ,
\end{aligned}
\tag{4.24}
$$

where the force term $[\mathbf{F}^{IC,n}]$ is calculated with the configuration of the immersed curve for the previous time step t_n. The immersed curve is integrated in time by means of the forward Euler method, *i.e.*,

$$\dot{\mathbf{y}}^n \doteq \frac{\mathbf{y}^{n+1} - \mathbf{y}^n}{\Delta t_n} \ , \tag{4.25}$$

where $\dot{\mathbf{y}}^n = \mathbf{v}(\mathbf{y}(s, t_{n-1}), t_n)$ is the velocity of the fluid at time step t_n interpolated at the immersed curve positions calculated at the previous time step t_{n-1} using (4.1).

4.2.4 Summary of the numerical algorithm for the extended IBM

The general process of the proposed extended numerical algorithm for simulating flexible filaments immersed in a thermally fluctuating fluid can be summarized as follows

Algorithm 1 Extended IBM algorithm

Initialize fluid field variables $[\mathbf{v}^0]$ and $[p^0]$
Initialize immersed curve position $[\mathbf{y}^0]$
Set $n = 0$
while $n < n\_step$ **do**
  Compute $[\mathbf{f}^n]$ defined in Equation (4.2) using Equations (4.17) and (4.18)
  Distribute Lagrangian interaction force $[\mathbf{F}^{IC,n}]$ to the Eulerian grid using $(4.21)_5$.
  Calculate $[\tilde{\mathbf{S}}^n]$ using Equation (4.19) for every cell of the fluid
  Compute $[\mathbf{F}^{th,n}]$ using Equation (4.21)
  Solve for $[\mathbf{v}^{n+1}]$ and $[p^{n+1}]$ based on Equation (4.24)
  Interpolate $[\mathbf{v}^{n+1}]$ at the filament positions to obtain $[\dot{\mathbf{y}}^{n+1}]$ using Equation (4.1)
  Compute the filament position $[\mathbf{y}^{n+1}]$ using Equation (4.25)
  $n \leftarrow n + 1$
end while

4.3 Coarse-grain formulation

The elastohydrodynamic behavior of extensible semiflexible filaments immersed in a fluid has been so far described in the previous sections with a continuous formulation. However, in the case of inextensible semiflexible filaments, a Lagrange multiplier for the continuum formulation would be necessary to ensure inextensibility. A nonlinear system of partial differential equations would have to be solved in

order to compute the new configuration of the inextensible semiflexible filament at every time step.

Another way, more straightforward and computationally efficient, to deal with the inextensibility of the semiflexible filaments is to use discrete models, where the filament is broken into a discrete number of straight segments and the elastic interaction coupling neighboring nodes/joints is described via discrete elastic connectors encoding the filament's resistance to bending. More specifically, the CGM [37] is used in this study, as the direct consequence of the asymptotic integration of the linear and angular momentum balance system along coarse-grained rod-like elements. The method is further extended to include an interaction force from the filament in the fluid equations to account for the two-way coupling between the immersed filament and the fluid.

4.3.1 Governing Equations

Consider an inextensible massless filament of length L immersed in an incompressible viscous fluid, and recall that the position of a point of the rod be denoted by $\mathbf{y}(s)$. The filament is embedded in a two-dimensional space associated with orthonormal basis $\{\mathbf{e}_x, \mathbf{e}_y\}$ and is subjected to external contact force $\mathbf{f}_h(s)$ per unit length due to the hydrodynamic interactions.

Assuming quasi-static loading conditions, the equilibrium equations are written as

$$\begin{aligned} \frac{\partial \mathbf{n}}{\partial s} + \mathbf{f}_h &= \mathbf{0} \,, \\ \frac{\partial \mathbf{m}}{\partial s} + \frac{\partial \mathbf{y}}{\partial s} \times \mathbf{n} &= \mathbf{0} \,, \end{aligned} \tag{4.26}$$

where $\mathbf{n}$ and $\mathbf{m}$ are the (internal) axial force and moment sustained by the filament. Integrating the force equilibrium equation $(4.26)_1$ over the entire filament leads to

$$\int_0^L \mathbf{f}_h(s)\, \mathrm{d}s = \mathbf{0} \,, \tag{4.27}$$

where it is further assumed that the boundary forces vanish, that is, $\mathbf{n}(0) = \mathbf{n}(L) = \mathbf{0}$.

Following Moreau *et al.* [37], the filament is partitioned into N straight subdomains (elements) of length $\Delta s = L/N$. The Frenet basis along the filament is given by the unit tangent and normal vectors $(\mathbf{e}_\parallel, \mathbf{e}_\perp)$, respectively, as shown in Figure 4.1. Also, the angle between $\mathbf{e}_\parallel$ and $\mathbf{e}_x$ is denoted θ. The discrete counterpart of the equilibrium equation (4.27) takes the form

$$\sum_{i=0}^{N-1} \int_{i\Delta s}^{(i+1)\Delta s} \mathbf{f}_h(s)\, \mathrm{d}s = \sum_{i=0}^{N-1} \mathbf{F}_{hi} = \mathbf{0} \,, \tag{4.28}$$

where $\mathbf{F}_{hi}$ represents the resultant external force experienced by the i-th element. For a filament free of boundary moments, that is, assuming, $\mathbf{m}(L) = \mathbf{m}(0) = \mathbf{0}$, one

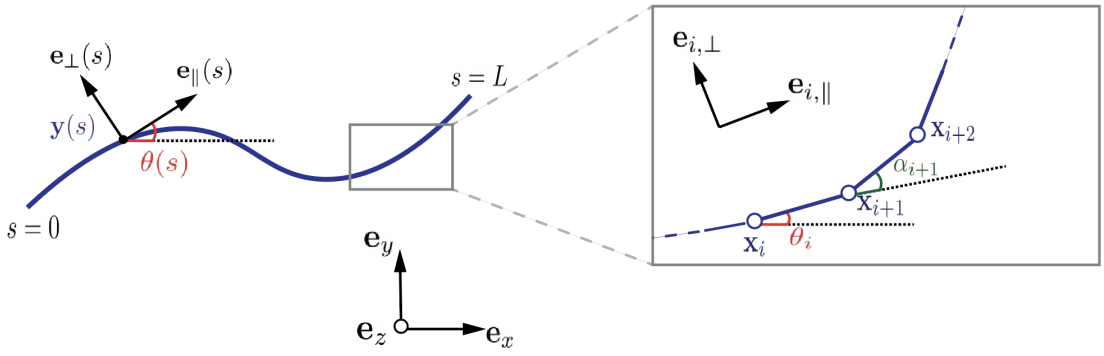

Figure 4.1: *Parametrization of the continuous and discretized filament*

may take the integral of $(4.26)_2$ over the entire filament, use integration by parts, and invoke $(4.26)_1$ and (4.28) to conclude that

$$\sum_{i=0}^{N-1} \int_{i\Delta s}^{(i+1)\Delta s} \frac{\partial \mathbf{y}(s)}{\partial s} \times \mathbf{n}(s)\, \mathrm{d}s \;=\; \sum_{i=0}^{N-1} \int_{i\Delta s}^{(i+1)\Delta s} (\mathbf{y}(s) - \mathbf{y}_0) \times \mathbf{f}_h(s)\, \mathrm{d}s$$
$$= \sum_{i=0}^{N-1} \mathbf{M}_{i,\mathbf{y}_0} \;=\; \mathbf{0}\;, \tag{4.29}$$

where $\mathbf{M}_{i,\mathbf{y}_0}$ is the moment of the external force acting on the i-th element about point $\mathbf{y}_0 = \mathbf{y}(0)$. Upon integrating Equation $(4.26)_2$ over the domain $\big((j-1)\Delta s, L\big)$, $j = 2, \ldots, N$, and taking into account (4.29), it follows that

$$\sum_{i=j}^{N} \mathbf{M}_{i,\mathbf{y}_j} \;=\; \mathbf{m}_j\;, \tag{4.30}$$

where $\mathbf{m}_j = \mathbf{m}((j-1)L/N)$, $j = 2, \ldots, N$, is the moment at the left end-point of the j-th element. Given that the moment at any point it is defined as $\mathbf{m}(s) = \kappa_b \frac{\partial \theta}{\partial s} \mathbf{e}_z$, where $\frac{\partial \theta}{\partial s}$ is the curvature and $\mathbf{e}_z = \mathbf{e}_x \times \mathbf{e}_y$, one may use the backward finite difference formula to find that

$$\mathbf{m}_j \;=\; \frac{\kappa_b}{\Delta s}(\theta_j - \theta_{j-1})\mathbf{e}_z \;=\; \frac{\kappa_b}{\Delta s}\alpha_j \mathbf{e}_z\;, \tag{4.31}$$

where $\alpha_j = \theta_j - \theta_{j-1}$, $j = 1, 2, \ldots, N$, is the angle between $\mathbf{e}_{i-1,\parallel}$ and $\mathbf{e}_{i,\parallel}$, as shown in Figure 4.1, and thus

$$\theta_i \;=\; \sum_{j\,=\,0}^{i} \alpha_j\;, \tag{4.32}$$

with $\alpha_0 = \theta_0$.

In the low-Reynolds number regime, the hydrodynamic force experienced by the filament immersed in fluid with velocity field $\mathbf{v}$ can be defined according to the

Resistive Force Theory [58] as

$$\mathbf{f}_h(s) \;=\; -\xi\,\Big[\mathbf{e}_\perp\cdot\big(\dot{\mathbf{y}}-\mathbf{v}(\mathbf{y})\big)\Big]\mathbf{e}_\perp+\eta\;\mathbf{e}_\parallel\cdot\Big[\big(\dot{\mathbf{y}}-\mathbf{v}(\mathbf{y})\big)\Big]\mathbf{e}_\parallel\;, \tag{4.33}$$

where $\mathbf{v}(\mathbf{y})$ is the fluid velocity interpolated at the filament positions, and ξ and η are the normal and tangential drag coefficients, respectively. Here, the external contact force $\mathbf{f}_h(s)$ is due to the resistance that the filament points experience as they move in the fluid.

The position $\mathbf{y}$ at time t is a point in the filament that satisfies $\mathbf{y}(s)=\mathbf{y}_0+\int_0^s\mathbf{e}_\parallel(\tau)\mathrm{d}\tau$, so that in the discrete case

$$\mathbf{y}_i \;=\; \mathbf{y}_0+\sum_{k=0}^{i-1}\mathbf{e}_{k,\parallel}\;\Delta s\;, \tag{4.34}$$

for $i=1,\dots,N$, thus $\mathbf{y}_i=\mathbf{y}((i-1)L/N)$ thus satisfying the inextensibility constraint from the outset. Here, $\mathbf{e}_{k,\parallel}$ denotes the tangent Frenet vector in the k-th element.

There are now $N+2$ parameters describing the position of the filament, that is, $(\mathbf{y}_0,\alpha_0,\dots,\alpha_{N-1})$. To determine them, there are two total force balance equations in (4.28), one torque balance in (4.29), and $N-1$ equations for the internal moment balance in (4.30), thus rendering this elastohydrodynamic system closed.

With slight abuse of notation, let $\mathbf{y}_i(s)$ denote the current position of a filament point on the i-th element, so that

$$\mathbf{y}_i(s) \;=\; \mathbf{y}_i+\big(s-(i-1)\Delta s\big)\mathbf{e}_{i,\parallel}\;. \tag{4.35}$$

The total hydrodynamic force on the i-th element is found from (4.33), with the aid of (4.28) and (4.35), to be

$$\begin{aligned}\mathbf{F}_{hi} \;=\; \int_{i\Delta s}^{(i+1)\Delta s}\mathbf{f}_h(s)\;\mathrm{d}s \;&=\; -\,\xi\Big\{\Delta s\,\Big[(\dot{\mathbf{y}}_i-\mathbf{v})\cdot\mathbf{e}_{i,\perp}\Big]+\frac{\Delta s^2}{2}\,\dot\theta_i\Big\}\,\mathbf{e}_{i,\perp}\\ &\quad+\eta\;\Delta s\,\Big[(\dot{\mathbf{y}}_i-\mathbf{v})\cdot\mathbf{e}_{i,\parallel}\Big]\mathbf{e}_{i,\parallel}\;.\end{aligned} \tag{4.36}$$

Note that, in general, $\mathbf{v}$ varies along the domain $\big(i\Delta s,(i+1)\Delta s\big)$. However, to within a small error, the velocity is assumed constant in each element. Using Equations (4.29) and (4.33), one finds that

$$\begin{aligned}\mathbf{e}_z\cdot\mathbf{M}_{i,\mathbf{y}_0} \;&=\mathbf{e}_z\cdot\int_{i\Delta s}^{(i+1)\Delta s}(\mathbf{y}(s)-\mathbf{y}_0)\times\mathbf{f}_h(s)\;\mathrm{d}s\\ &=\;-\frac{\Delta s^2}{2}\xi\Big[(\dot{\mathbf{y}}_i-\mathbf{v})\cdot\mathbf{e}_{i,\perp}\Big]+\frac{\Delta s^3}{3}\xi\;\dot\theta_i\\ &\quad+(\mathbf{y}_i-\mathbf{y}_0)\times\Big\{-\Delta s\;\eta\Big[(\dot{\mathbf{y}}_i-\mathbf{v})\cdot\mathbf{e}_{i,\parallel}\Big]\mathbf{e}_{i,\parallel}\\ &\qquad+\Big(\Delta s\;\xi\Big[(\dot{\mathbf{y}}_i-\mathbf{v})\cdot\mathbf{e}_{i,\perp}\Big]+\frac{\Delta s^2}{2}\xi\dot\theta_i\Big)\mathbf{e}_{i,\perp}\Big\}\cdot\mathbf{e}_z\;.\end{aligned} \tag{4.37}$$

Therefore, Equations (4.28-4.30), with the aid of (4.36) and (4.37), take the form

$$\begin{aligned}
\sum_{i\,=\,0}^{N-1} \mathbf{F}_{hi} &= \mathbf{0} \ , \\
\mathbf{e}_z \cdot \sum_{i\,=\,0}^{N-1} \mathbf{M}_{i,\mathbf{y}_0} &= 0 \ , \\
\mathbf{e}_z \cdot \sum_{i\,=\,k}^{N-1} \mathbf{M}_{i,\mathbf{y}_k} &= \frac{\kappa_b}{\Delta s}\alpha_k \ , \ k = 1, \ldots, N-1 \ .
\end{aligned} \tag{4.38}$$

These coarse-grained elastohydrodynamics equations, in conjunction with Equations (4.32) and (4.34), can be cast a system of ordinary differential equations of the form

$$[\mathbf{A}][\mathbf{Q}][\dot{\mathbf{Y}}] \ = \ [\mathbf{B}] + [\mathbf{A}][\mathbf{V}] \ , \tag{4.39}$$

where $[\mathbf{Y}] = [x_0 \ y_0 \ \theta_0 \ \alpha_1 \ \ldots \alpha_{N-1}]^T$ are the $N+2$ parameters with $(x_0, y_0) = \mathbf{y}_0$, and $[\mathbf{V}]$ is a vector of size $3N$, containing in the first $2N$ entries the x- and y-components of the flow velocity at the filament points $i = 0, 1, \ldots N-1$ with the remaining entries being zero.

The matrix $[\mathbf{A}]$ has dimensions $(N+2) \times 3N$ and its coefficients are given, for all $i, j = 0, \ldots, N-1$, by

$$\begin{aligned}
a_{1,i} &= \Delta s \ (-\xi \cos^2\theta_i - \eta \sin^2\theta_i) \ , \\
a_{1,N+i} &= \Delta s \ (\eta - \xi) \cos\theta_i \sin\theta_i \ , \\
a_{1,2N+i} &= \frac{\Delta s}{2} \sin\theta_i \ , \\
a_{2,i} &= \Delta s \ (\eta - \xi) \cos\theta_i \sin\theta_i \ , \\
a_{2,N+i} &= \Delta s \ (-\eta \cos^2\theta_i - \xi \sin^2\theta_i) \ , \\
a_{2,2N+i} &= -\frac{\Delta s}{2} \cos\theta_i \ , \\
a_{i+2,j} &= \begin{bmatrix} 1 & x_j - x_i & y_j - y_i \end{bmatrix} \begin{bmatrix} \frac{\Delta s^2}{2} \sin\theta_j & \Delta s \ (\eta - \xi) \cos\theta_j \sin\theta_j & \Delta s \ (\xi \cos^2\theta_j + \eta \sin^2\theta_j) \end{bmatrix}^T , \\
a_{i+2,N+j} &= \begin{bmatrix} 1 & x_j - x_i & y_j - y_i \end{bmatrix} \begin{bmatrix} -\frac{\Delta s^2}{2} \cos\theta_j & -\Delta s(\eta \cos^2\theta_j + \xi \sin^2\theta_j) & \Delta s(\xi - \eta) \cos\theta_j \sin\theta_j \end{bmatrix}^T , \\
a_{i+2,2N+j} &= \begin{bmatrix} 1 & x_j - x_i & y_j - y_i \end{bmatrix} \begin{bmatrix} -\eta\frac{\Delta s^3}{3} & -\eta\frac{\Delta s^2}{2} \cos\theta_j & -\eta\frac{\Delta s^2}{2} \sin\theta_j \end{bmatrix}^T .
\end{aligned} \tag{4.40}$$

If $j < i$, then $a_{i+2,j} = a_{i+2,N+j} = a_{i+2,2N+j} = 0$. Also, the column vector $[\mathbf{B}]$ of size $N+2$ is given by

$$[\mathbf{B}] \ = \ \begin{bmatrix} 0 & 0 & \frac{\kappa_b \alpha_0}{\Delta \mathrm{s}} & \frac{\kappa_b \alpha_1}{\Delta \mathrm{s}} & \ldots & \frac{\kappa_b \alpha_{N-1}}{\Delta \mathrm{s}} \end{bmatrix}^T . \tag{4.41}$$

In addition, matrix $[\mathbf{Q}]$ is a $3N \times (N+2)$ transformation matrix defined as

$$[\mathbf{Q}] = \left[\begin{array}{cc|ccc} 1 & 0 & & & \\ \vdots & \vdots & & [\mathbf{Q}_1] & \\ 1 & 0 & & & \\ \hline 0 & 1 & & & \\ \vdots & \vdots & & [\mathbf{Q}_2] & \\ 0 & 1 & & & \\ \hline & & 1 & 0 \quad \ldots & 0 \\ & & 1 & 1 \quad \ddots & \vdots \\ & [\mathbf{0}_{N,2}] & \vdots & \quad \ddots & 0 \\ & & 1 & \ldots \quad & 1 \end{array}\right] , \tag{4.42}$$

where $[\mathbf{Q}_1]$ and $[\mathbf{Q}_2]$ are $N \times N$ matrices whose elements are given by the general formula

$$\begin{aligned} Q_1^{i,j} &= -\Delta s \sum_{k=j}^{i-1} \sin\left(\sum_{m=1}^{k} \alpha_m\right) , \\ Q_2^{i,j} &= \Delta s \sum_{k=j}^{i-1} \cos\left(\sum_{m=1}^{k} \alpha_m\right) , \end{aligned} \tag{4.43}$$

with $Q_1^{i,j} = Q_2^{i,j} = 0$ if $i \leq j$. Also, $[\mathbf{0}_{N,2}]$ denotes an $N \times 2$ zero matrix.

The system of equations in (4.39) is integrated in time using an implicit first-order method with constant time step Δt. Writing the system of equations at time t_{n+1}, one can obtain $[\mathbf{Y}^{n+1}]$ by solving implicitly the system of equations

$$\frac{[\mathbf{A}^n][\mathbf{Q}^n]}{\Delta t}[\mathbf{Y}^{n+1}] - [\mathbf{B}^{n+1}] = \frac{[\mathbf{A}^n][\mathbf{Q}^n]}{\Delta t}[\mathbf{Y}^n] + [\mathbf{A}^n][\mathbf{V}^n] , \tag{4.44}$$

in the typical time domain $(t_n, t_{n+1}]$.

4.3.2 Interaction force and two-way coupling

To account for the two-way coupling between the filament and the fluid, an interaction force term $[\mathbf{F}^{ICh,n}]$ is included in the Navier-Stokes equations, and it is set to be equal and opposite to the hydrodynamic force $[\mathbf{F}_{hi}]$ experienced by the fiber moving with the fluid with velocity field according to the Resistive Force Theory [58] and Equation (4.33). The perpendicular and parallel drag coefficients in Equation

(4.33) for a filament of cross-sectional radius r and length $2l$ are defined, following Lighthill's classical analysis [59] as

$$\eta = \frac{8\pi\mu}{\ln(l^2/r^2)+1}\,,$$
$$\xi = \frac{4\pi\mu}{\ln(4l^2/r^2)-1}. \tag{4.45}$$

4.3.3 Summary of the numerical algorithm for the hybrid IBM/CGM

The general process of the proposed numerical algorithm for simulating flexible inextensible filaments immersed in a fluid can be summarized as follows

Algorithm 2 Hybrid IBM/CGM algorithm

Initialize fluid field variables $[\mathbf{v}^0]$ and $[p^0]$
Initialize immersed curve position $[\mathbf{y}^0]$
Set $n = 0$
while $n < n\_step$ **do**
Compute $[\mathbf{V}^n]$ by interpolating $[\mathbf{v}^n]$ at the filament positions using Equation (4.1)
Compute $[\mathbf{F}^n_{hi}] = [\mathbf{A}^n][\mathbf{V}^n]$
Compute the filament position $[\mathbf{y}^{n+1}]$ using Equations (4.44)
Compute $[\mathbf{F}^{ICh,n}] = -[\mathbf{F}^n_{hi}]$
Distribute Lagrangian interaction force $[\mathbf{F}^{ICh,n}]$ to the Eulerian grid using Equation $(4.21)_5$
Solve for $[\mathbf{v}^{n+1}]$ and $[p^{n+1}]$ based on Equation (4.24)
$n \leftarrow n+1$
end while

4.4 Concluding Remarks

In this chapter, the IBM method was described and its weak forms were developed based on the set of governing equations presented in Chapter 2. An extended version of the IBM was proposed, which additionally accounts for the hydrodynamic thermal fluctuations in the fluid by including a stochastic stress tensor in the Navier-Stokes equations. The spatial discretization of the extended IBM was formulated within the context of the finite element method for the fluid domain and the finite difference method for the immersed boundary. Temporal discretization of the governing equations was developed, and additionally, the numerical algorithm for simulating

flexible filaments immersed in a thermally fluctuating fluid was summarized. Additionally, the CGM was derived in order to describe the elastohydrodynamic behavior of inextensible semiflexible filaments and further extended to account for the two-way coupling between the inextensible filament and the fluid. Lastly, a hybrid IBM/CGM algorithm was proposed.

Chapter 5

Applications

5.1 Overview

This chapter describes the implementation of the methods in Chapter 4 using the Deal.II Finite Element Library [66] in order to investigate the orbit regime of flexible filaments in shear flow in Section 5.2 and the mechanical behavior of the actin cortex in Section 5.3. More specifically, in Section 5.2 the two-dimensional numerical model based on a combination of IBM and CGM, described in Section 4.3.2, is implemented for capturing the hydrodynamic interaction of filaments in viscous shear flow while strictly enforcing the filament inextensibility condition, without restricting the time step in contrast to the regular IBM. The results of the modified IBM simulations are first validated and then used to develop prediction models with ANN, for the two-dimensional orbit classes for flexible filaments placed in shear flow with different parameters. In Section 5.3.1, the response of a single inextensible filament is studied with the proposed numerical algorithms in order to verify that the time-averaged contraction under thermal fluctuations is in accordance with the values of Section 2.4. Furthermore, the mechanical behavior of the actin cortex under shear is studied in Section 5.3.2, illustrating a stiffening of the cross-linked network with increasing strain under shear flow. Lastly, in Section 5.3.3, the behavior and motion of passive F-actin filaments under hydrodynamic thermal fluctuations is investigated, demonstrating that filaments tend to spread out under thermal fluctuations.

5.2 Numerical simulation and prediction model development of a flexible filament in viscous shear flow using ANN

In the following study, a two-dimensional numerical algorithm based on a combination of IBM and CGM, as described in Section 4.3.2, is implemented to capture

the hydrodynamic interaction of filaments in viscous shear flow. While strictly enforcing the filament inextensibility condition, the time step required is not restricted in contrast to the regular IBM [34], [35]. The behavior of a semiflexible inextensible filament subjected to viscous shear flow is studied and a parametric analysis is conducted by varying filament length, bending rigidity and shear rate. The results of the modified IBM simulations are first validated and then used to develop predictive models based on ANN for two-dimensional orbit classes of flexible filaments placed in shear flow with different values of filament length, flexular rigidity, and shear rate.

5.2.1 Theory and Experiments

As early as 1922, Jeffery [28] studied the motion of a single ellipsoidal, rigid, neutrally buoyant particle in a Couette flow and proved that the center of the particle follows the streamlines and rotates about its center according to

$$\phi(t) \;=\; \tan^{-1}\left[r_e \tan\left(\frac{\dot{\gamma}\, r_e t}{r_e^2+1}\right)\right], \tag{5.1}$$

where ϕ is the angle that the major axis of the ellipsoid makes with the vertical, r_e is the ratio of the lengths of the major and minor axes of the ellipsoid in Figure 5.1, and $\dot{\gamma}$ is the shear rate.

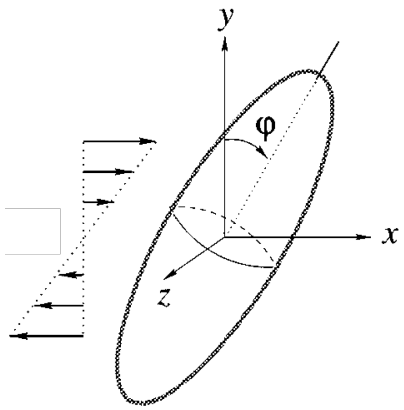

Figure 5.1: *Jeffery's ellipsoidal particle immersed in a Couette flow [34]*

The period of motion is constant and given by

$$T \;=\; \frac{2\pi}{\dot{\gamma}}\left(r_e + \frac{1}{r_e}\right), \tag{5.2}$$

while the angular displacement of a rotating ellipsoid in the (x, y)-plane according to Jeffery's Equation (5.1) is plotted in Figure 5.2 versus nondimenionalised time and $r_e = 60$. In rigid case, cylindrical fibers instead of idealized ellipsoids, Anczurowski and Mason [67] showed that Jeffery's Equation (5.1) could be used to describe the motion by replacing r_e with an equivalent ellipsoidal axis ratio $r*_e$, so as to match the selected period from experiments.

For the case of flexible filaments, experimental studies by Forgacs and Mason in [29] identified a wide range of fiber behaviors, which they separated into distinct orbit classes based on the flexibility of the fiber. A summary of two-dimensional orbits in nature is shown in Figure 5.3, since these are the only motions that can be simulated by the two-dimensional fiber model of the present study.

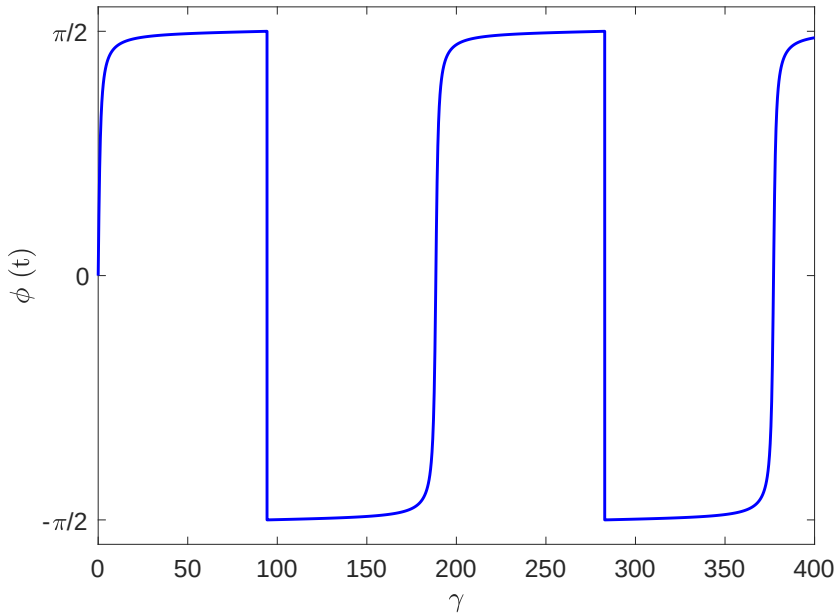

Figure 5.2: *Angular displacement of a rotating ellipsoid in the* (x, y)*-plane versus nondimenionalised time and* $r_e = 60$

Forgacs and Mason [29] conclude that the fiber motion is a function of shear rate, bending stiffness, and fiber length. As shown in Figure 5.3, there are four orbit classes in total. Rigid fibers (class I) rotate as solid cylinders, with angular velocity that reaches a maximum when the fiber is perpendicular to the shear flow. Slightly more flexible filaments behave according to springy rotation (class II), where the fiber still revolves but deforms into the shape of an arc during the spin. In the case of S-turn (class IIIA) and snake turn (class IIIB), the fiber is deformed into a more intricate curved intermediate shape, after which it straightens out once again. In the final case, the complex rotation (class IV), the fiber performs a snake-like turn but never straightens out, continuing to loop over itself.

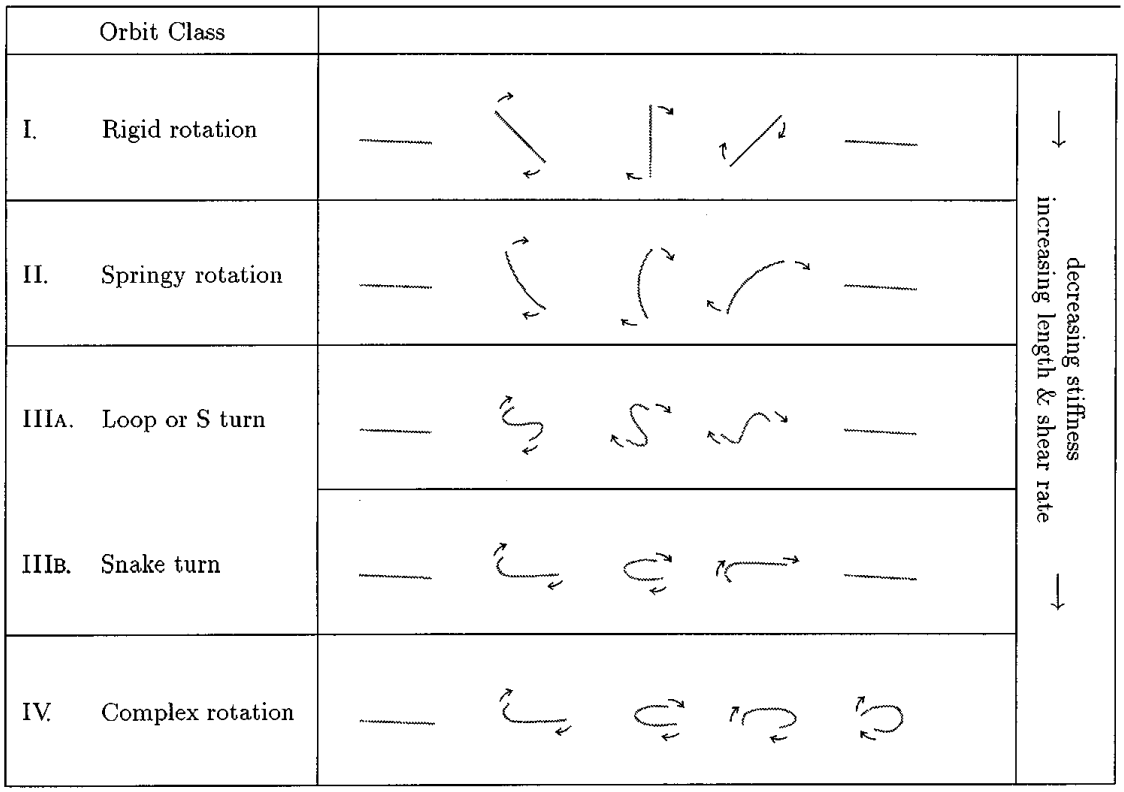

Figure 5.3: *Summary of the two-dimensional orbits in nature [34]*

5.2.2 Mathematical Description and Numerical Scheme

In the present study, a two-dimensional numerical model based on a combination of IBM and CGM, as described in Section 4.3.2, is implemented to capture the hydrodynamic interaction of filaments in viscous shear flow, while strictly enforcing the filament inextensibility condition. The immersed fibers are flexible, force-bearing filaments, submerged in an incompressible fluid. The aspect ratios of the individual fibers are very large, so that fibers are nearly one-dimensional structures. Also, the flow conditions correspond to very low Reynolds numbers.

A rectangular fluid domain, Ω, with dimensions $L_x \times L_y$, filled with an incompressible, viscous fluid is considered, as shown in Figure 5.4. The top and bottom walls are moved with constant velocity v in opposite directions, resulting in a shear flow with shearing rate $\dot{\gamma} = 2v/L_y$. Proper periodic boundary conditions are applied to the right and left boundaries.

The motion of the fluid is governed by the incompressible Navier-Stokes equations

$$\begin{aligned} -\operatorname{grad} p + \mu \operatorname{div} \operatorname{grad} \mathbf{v} + \mathbf{F} &= \rho \frac{\partial \mathbf{v}}{\partial t} , \\ \operatorname{div} \mathbf{v} &= 0, \end{aligned} \tag{5.3}$$

as described in Section 4.2.1, where, given the low Reynolds flow conditions, the convective rate of change can be neglected, keeping only the spatial time derivative term in order for capturing the effects of the unsteady flow due to the two-way coupling between the fiber and the surrounding fluid.

The motion of the fiber can be described with the CGM of Section 4.3. The force term defined in Section 4.3.2 and Equation (4.33) for the two-way coupling between the fiber and the fluid is included. The numerical algorithm used in this study for simulating flexible inextensible filaments immersed in a fluid is described in Section 4.3.2.

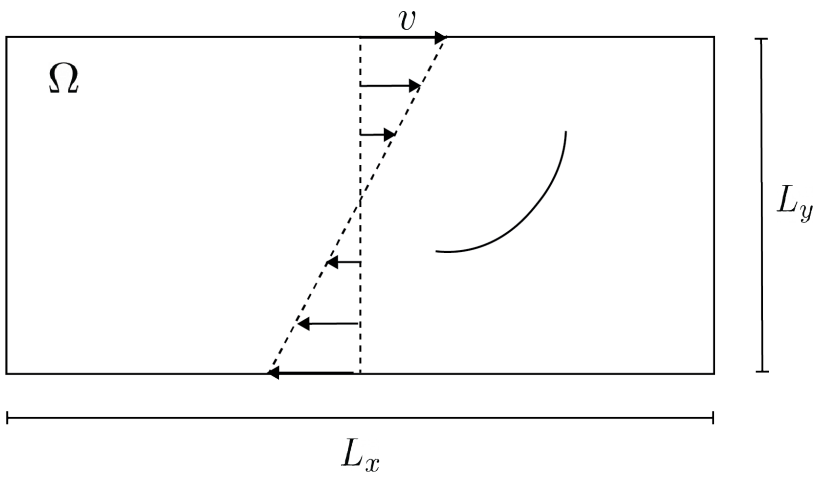

Figure 5.4: *Fiber immersed in shear flow*

5.2.3 Computational Results and Discussion

5.2.3.1 Model Validation

The numerical model described in Section 4.3 is used to describe the various filament orbit classes. Forgacs and Mason [29] with experimental studies, and Stockie with Green [34] and Wiens and Stockie [35] using numerical simulations on dynamics of the flexible filament by varying filament length, shear rate and bending rigidity, were able to successfully categorize filament deformation in shear flow into the various orbit classes presented in Figure 5.3.

The filament orbit classes with the numerical scheme of the previous section are compared with the results obtained by Stockie and Green [34] who performed a two-dimensional numerical simulation using an IBM based on a mixed Eulerian-Lagrangian finite difference scheme.

A fiber of length $0.1 - 0.3$ cm is freely placed in a rectangular fluid domain 2 cm by 0.5 cm, as shown in Figure 5.4. The fluid domain is discretized with a mesh spacing of $h = \frac{1}{64}$ cm (*i.e.*, 128×32 fluid grid points) and the fiber with $40 - 120$ points, depending on the length of the fiber which varies from $0.1 - 0.3$ cm. The physical parameters are summarized in Table 5.1. A steady velocity v in the x-direction is applied at the top and bottom boundary of the fluid domain in opposite direction

to induce shear flow. Proper periodic boundary conditions are applied to the right and left boundaries. The fluid domain is discretized using 64×64 Q2-Q1 (Taylor-Hood) elements and is solved using the Navier-Stokes equations of Section 2.2.3. The algorithm of Section 4.3.3 is used to solve the fluid-structure interaction system, with a time step $\Delta t = 10^{-3}$ s, as discussed in the next paragraph.

Parameter	Values	Units
ρ (density)	8.0	g/cm^3
μ (viscosity)	1.0	g/cm $\cdot$ s
$\dot{\gamma}$ (shear rate)	8-32	s^{-1}
L_f (fiber length)	0.1-0.3	cm
r_e (aspect ratio)	60	-
EI (bending stiffness)	1.0-5.0 $\times$ 10^{-4}	g $\cdot$ cm^3/s^2
Re (Reynolds Number)	0.1-0.25	-

Table 5.1: *Physical parameters for the problem of flexible inextensible filament immersed in a viscous shear flow*

In contrast with Stockie and Green in the [34] who had to use a very large value for the stretching coefficient in order to maintain fiber inextensibility constraint, the present numerical scheme is able to enforce the fiber inextensibility strictly. The present numerical model does not place severe restrictions on the time step for ensuring stability. In the present study, the time step Δt is set to be equal to 10^{-3}, almost 100 times larger than the one used in [34], which was in the range of $2.0 - 5.0 \times 10^{-5}$.

With the present proposed numerical scheme, the new fiber position is obtained by solving the ordinary differential equations in (4.39) given the velocity field of the fluid interpolated on the fiber points. One may observe that the proposed numerical scheme results in some minor slip of the fiber relative to the fluid that violates the no-slip condition. However, as the time step size is reduced, the slip between the fiber and the fluid tends to dissapear, as shown in Figure 5.5. Even for a large time step $\Delta t = 10^{-3}$, the slip is still small and combined with the fact that the ordinary differential equations in (4.39) are solved implicitly, this allows one to use such a large time step for the present computations without any stability problems.

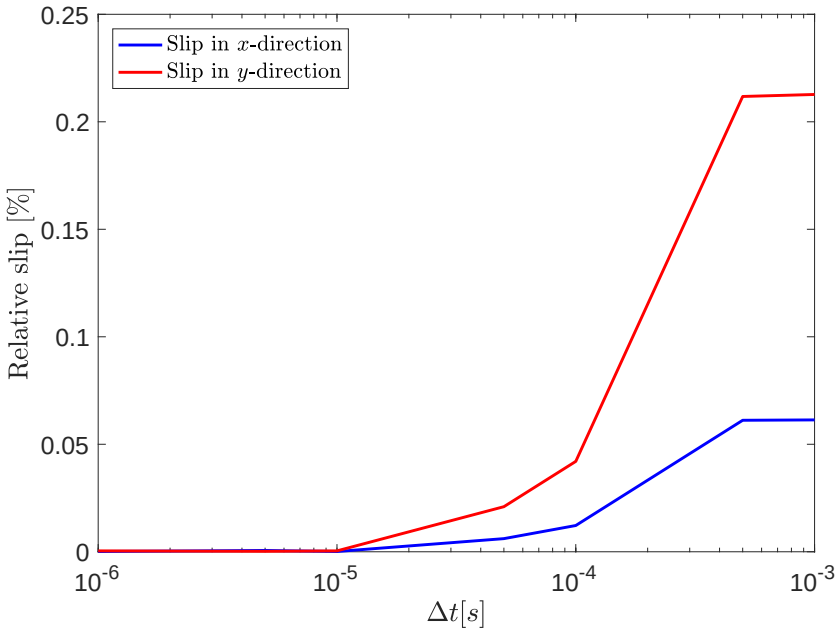

Figure 5.5: *Relative slip between fiber and fluid due to the numerical scheme as a function of time step size* Δt

As stated in the previous section, the deformation of an individual fiber is a function of the fiber length, stiffness and the fluid shear rate. It is useful, for purposes of comparison, to consider a dimensionless parameter, which is a measure of the fiber flexibility, defined in [68] for low Reynolds numbers as

$$\chi = \frac{\mu \dot{\gamma} L_f^3}{EI}, \tag{5.4}$$

which depends on these three quantities, in addition to the fluid viscosity. It is interesting to note that the fiber aspect ratio r_e does not appear in the parameter χ, which is a consequence of the fact that the fiber thickness does not play a role in two-dimensional flows. The dimensionless parameter χ will be used in the simulation in the next section to separate the various fiber orbits.

The numerical scheme is first validated by comparing qualitatively the behavior of solutions for four values of bending stiffness that reproduce the orbit classes in Figure 5.3. More specifically, numerical simulations are carried out with the proposed numerical scheme to investigate the orbit of a fiber of four different values of dimensionless bending stiffness K_b, between 0.004 and 0.5. The time sequences from the simulations are given in Figure 5.6 and are qualitatively compared with the time sequences of the Stockie and Green in [34] (see Figure 6 of [34]).

The other parameters were selected to much those used by Stockie and Green in [34], *i.e.*, $\dot{\gamma} = 10$ and $L_f = 0.1$. The fiber was initially given a small curvature and inclined at a slight angle to the flow, similar with [34]. The snapshots of fiber deformation for different values of χ in Figure 5.6 show an excellent qualitative similarity when compared with the results of Stockie and Green in [34], confirming the validity of the developed model.

For high bending stiffness $K_b = 0.6$ and, therefore low χ, the filament behaves rigidly, remaining straight throughout its motion. As χ increases and K_b decreases, the filament undergoes slight bending at the center showing a springy deformation. Further reduction in bending rigidity causes the filament to buckle about its center, undergoing a snake turn and at even smaller values of K_b, a complex rotation.

By comparing the snapshots in Figure 5.6 up to time $t = 0.09$ s, it can be observed that the flexible fibers complete their first half-rotation in significantly shorter time than the rigid fibers, a behavior that has been also observed in experiments [29]. To further investigate this observation, the angle ϕ, made by the vertical and the straight line joining the endpoints of the filament, is analyzed for various cases of filament deformation. The filament is initially inclined at 10^o, and therefore, the angle ϕ fromed by it with respect to the vertical is equal to 80^o. Figure 5.7 compares the angle ϕ for two cases of filament deformation, rigid and complex, with respect to time. The flexible filament rotates faster than the rigid filament as seen in Figure 5.7. After completing the loop, the filaments in the first three orbits, *i.e.* rigid, spring and C-shape, spend an extended period of time near the horizontal, as Figure 5.8 shows, which compares the angle ϕ made by a filament for a rigid, springy and C-shape deformation case with respect to time.

After a great deal of time, the filaments of the first three orbits eventually pass through the horizontal and essentially begin a second loop, identical to the first. However, the period of rotation decreases as the filament stiffness decreases. The period of rotation is significantly smaller for the complex case, as Figure 5.9 shows, where the orientation angle ϕ versus time for two cases of filament deformation, rigid and complex, is plotted. As seen in Figure 5.9, the flexible filament begins another turn around $t = 0.6$ s, while the rigid filament still remains nearly horizontal.

In order to compare more quantitatively the results of the proposed numerical scheme with the theoretical predictions in terms of the amount of time the fiber spends at each orientation angle during a rotation loop, the probability distribution of the orientation angle for a flexible filament (springy case) is further investigated for a shear rate equal to $\dot{\gamma} = 32\ \text{s}^{-1}$. The probability distribution of ϕ was estimated from the results for a period of time comprising at least four complete loops and is plotted in Figure 5.10. Similar to Stockie and Green in [34], given a set of observed orientation angles ϕ^n at discrete times t_n for $n = 1, 2, ..., M$, then the

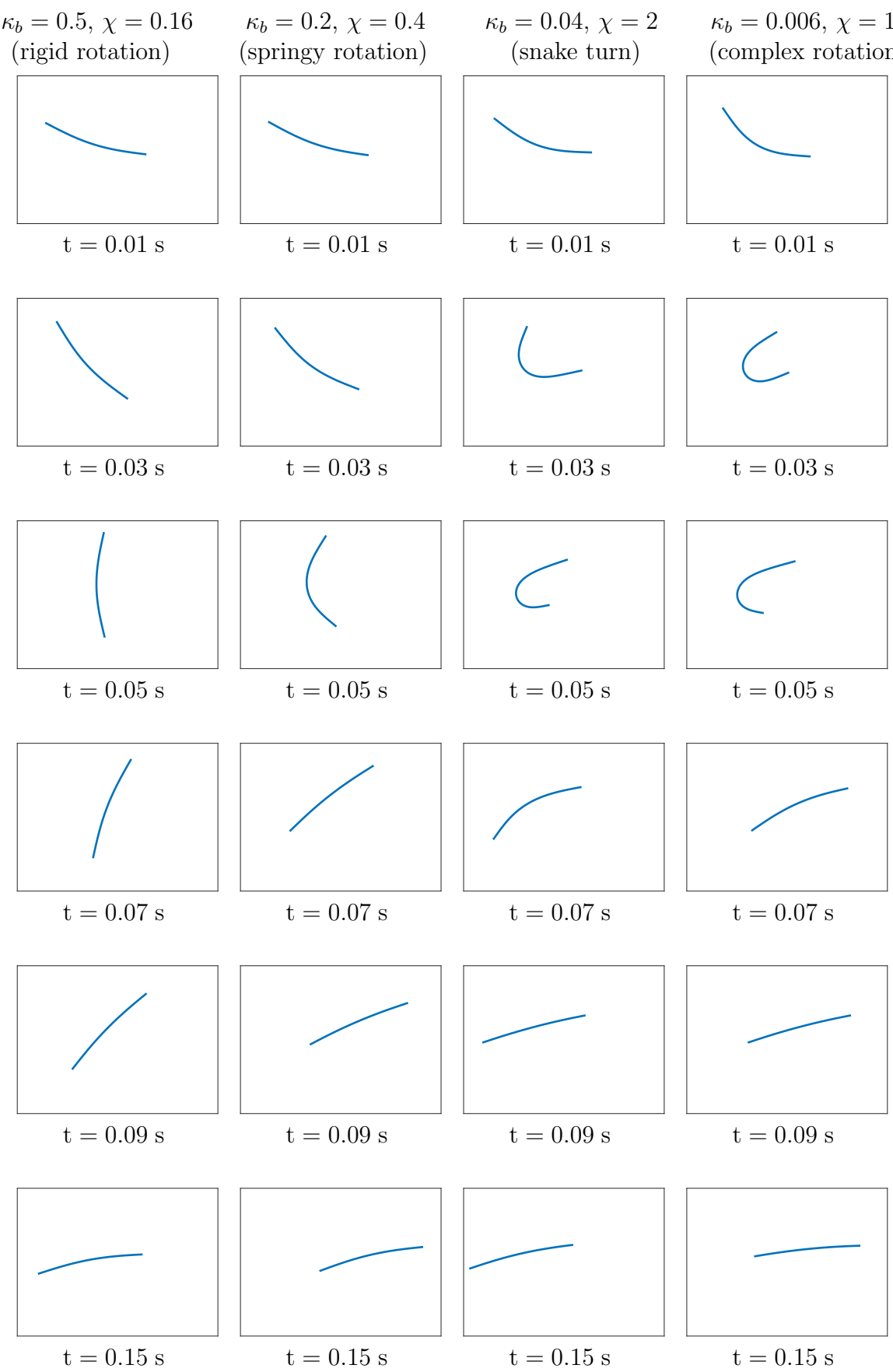

Figure 5.6: Time sequences of orbits - qualitative validation with Stockie and Green

probability that ϕ lies between two angles ϕ_0 and $\phi_0 + \Delta$ is estimated using the formula

$$\text{Prob}(\phi \in [\phi_0, \phi_0 + \Delta]) \doteq \frac{\#\{\phi^n \in [\phi_0, \phi_0 + \Delta]\}}{M}. \tag{5.5}$$

where # denotes the number of observed orientation angles.

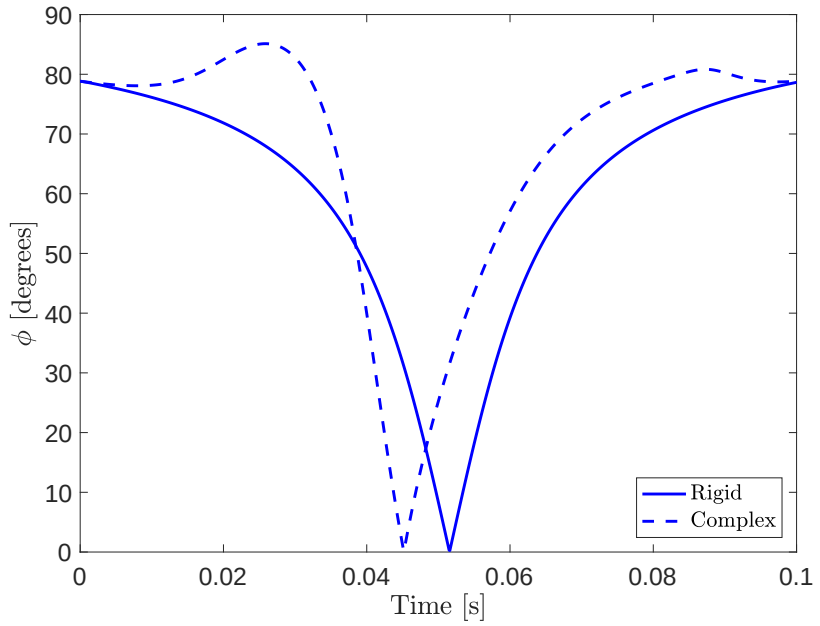

Figure 5.7: *Comparison of angle (ϕ) for rigid and flexible filament (Complex orbit)*

Figure 5.10 plots the corresponding distribution of Equation (5.1) as dotted curve. An equivalent ellipsoidal axis ratio r_e* was selected, that corresponds to the average period observed for the computed orbit. As expected from the theory, the filament spends the majority of its time near the horizontal and, both the size and shape of the simulation's distribution is similar to the prediction from Jeffery's equation. A slight offset of the curve near the peak is however observed, which is in agreement with the observations made by Stockie and Green in [34]. [34] concludes that the observed skewness, which is due to the tendency of the fiber to remain at an angle slightly above the horizontal plane, is created by the interaction between fiber and fluid, which is not included in Jeffery's equation.

All these observations are in excellent agreement with those by Stockie and Green [34]. Thus, the present numerical scheme demonstrates its qualitative ability to simulate the two-dimensional filament dynamics in shear flow as observed in previous experimental and numerical studies.

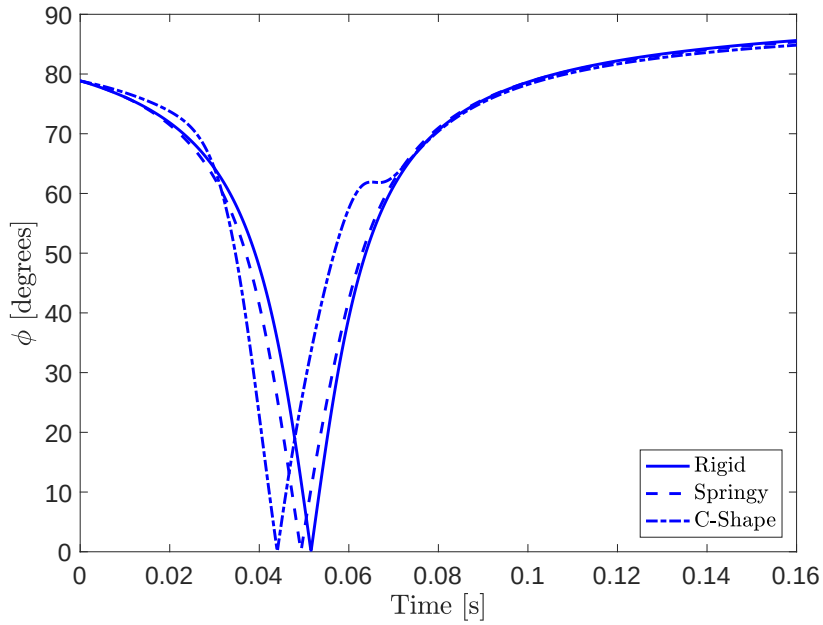

Figure 5.8: *Comparison of angle (ϕ) for different orbit classes*

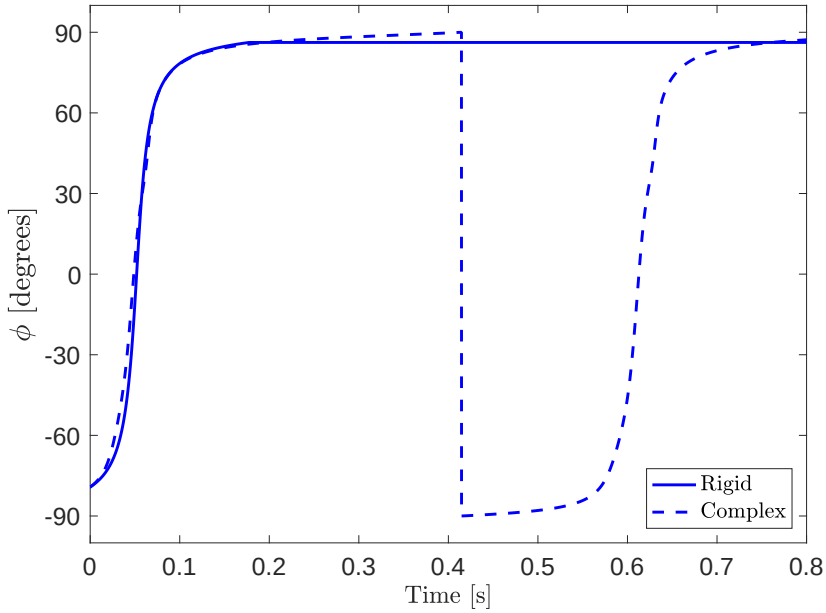

Figure 5.9: *Comparison of angle (ϕ) and period of rotation for a rigid and a flexible filament (Complex orbit)*

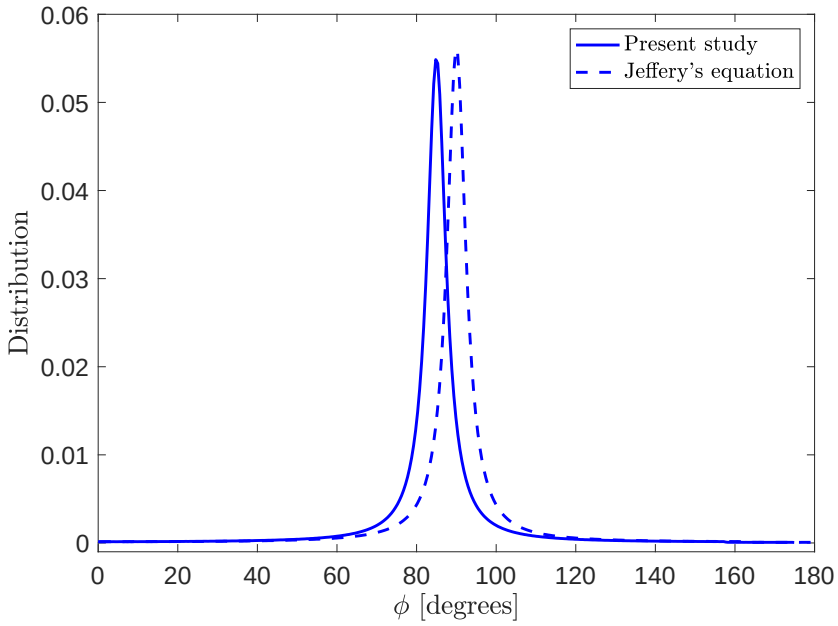

Figure 5.10: *Distribution of time spent at various angles throughout the motion of a fiber undergoing springy rotation for* $G = 32$. *The solid curve represent the computed orientation angles and the dotted curve is the corresponding theoretical prediction from Jeffery's Equation* (5.1).

5.2.3.2 Filament orbit classes

A parametric analysis is performed for three different filament lengths ($L_f = 0.1, 0.2, 0.3$), three different values of shear rates ($\dot{\gamma} = 10, 16, 32$), and 16 different values of bending rigidity, resulting in a total of 144 parametric test cases. The resulting orbit classifications are plotted in Figures 5.12 - 5.14 in terms of the nondimensional flexibility measure χ and the bending stiffness K_b.

Based on the exterior angle α, defined as the angle between the tangent lines at the endpoints of the fiber in Figure 5.11, each computed orbit is classified as belonging to either the Rigid class, the Springy class, the C-shape class or the Complex class. According to the criterion developed in [34], the filament is considered rigid if $175^o < \alpha < 180^o$, springy if $90^o < \alpha < 175^o$, C-shape for $90^o < \alpha < 30^o$, and complex if complex for $\alpha < 30^o$.

In Figure 5.12, along with the present simulation results for a filament of length $L_f = 0.1$, the experimental results of Forgacs and Mason [29] and the numerical results of Stockie and Green [34] are also included in the classification plot for comparison.

Figure 5.11: *Definition of the exterior angle α, measured between the ends of a flexible fiber*

In Figure 5.12, the black solid points show the experimental results of Forgacs and Mason [29], the open points indicate numerical results of Stockie and Green [34] and the colored solid points are the results of the present study. It can be concluded that the results of the present study are in excellent agreement with the experimental results of Forgacs and Mason [29] and the numerical results of Stockie and Green [34]. The vertical solid lines indicate the transition between different filament orbit regimes. The transition from rigid orbit to springy to C-shape to complex is happening at $\chi = 0.16, 1.6, 10.6$, respectively, consistent with the criterion of Stockie and Green [34], as well as with the numerical results by Kanchan and Maniyeri in [27].

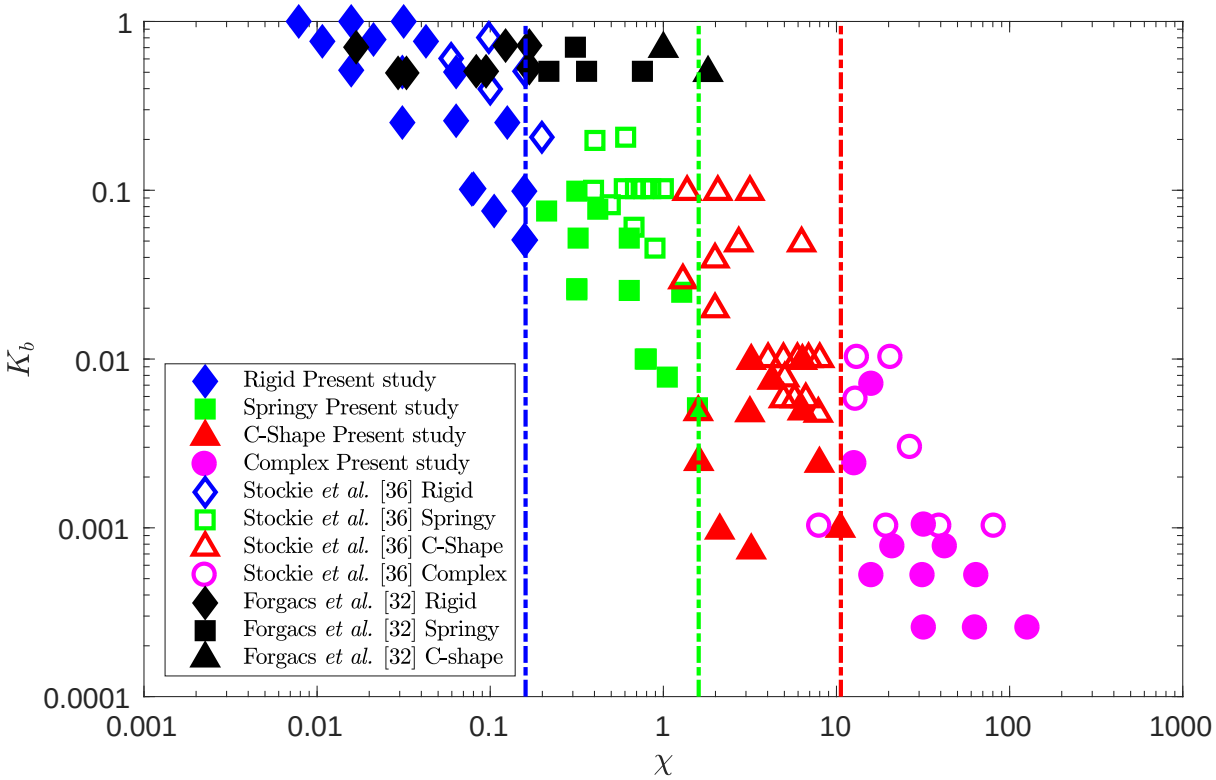

Figure 5.12: *Classification of flexible filament deformations for filament length L_f = 0.1 cm into various orbit classes with bending stiffness and χ*

These results demonstrate the ability of the proposed modified IBM to simulate the motion of flexible filaments in low-Reynolds number shear flows, allowing for more computationally efficient simulations (about 100 times faster compared with previous numerical studies [34] and [27]), without compromising the accuracy of the results.

Figure 5.13 shows the classification of the orbits for a filament length of $L_f = 0.2$ and it can be observed that the C-shape and complex regimes are pronounced compared with the rigid case, with a large band of orbits lying in the C-shape zone. Figure 5.14 shows the classification of filament orbits for length $L_f = 0.3$. As observed, only a few cases lie in the rigid zone, with the largest number of filament orbits lying in the C-shape and complex regime.

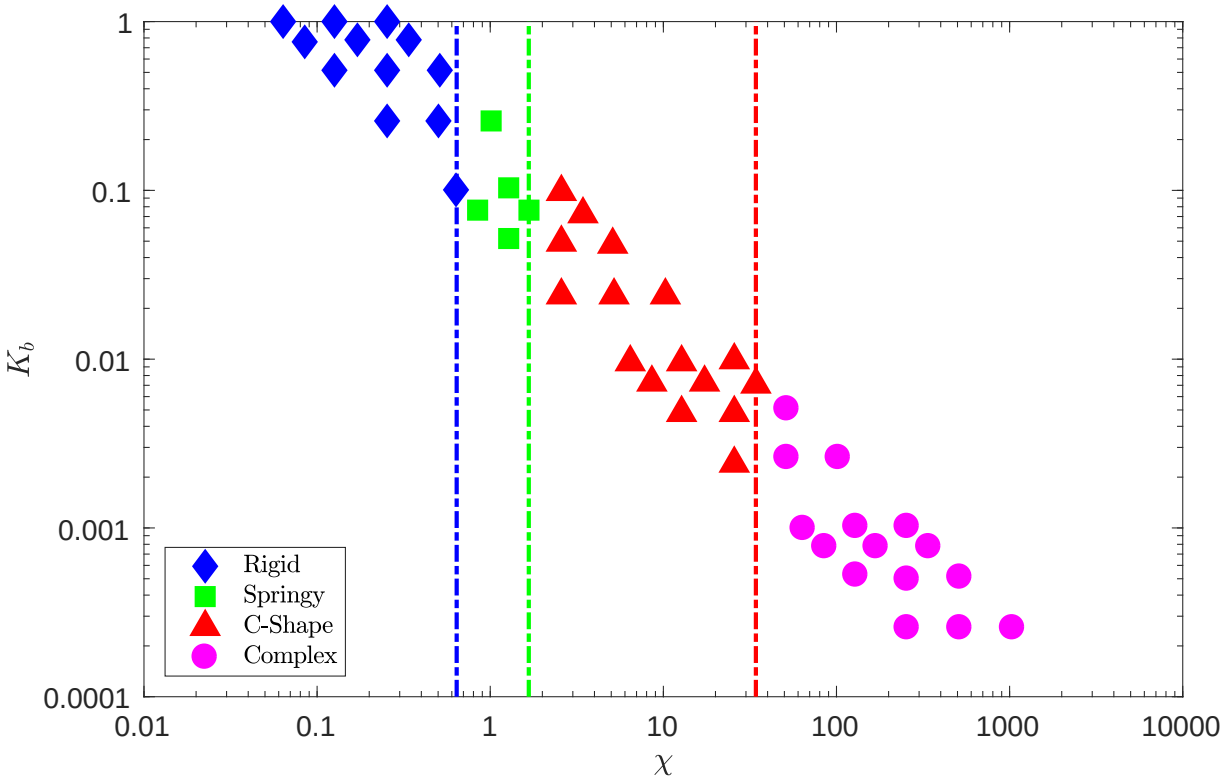

Figure 5.13: *Classification of flexible filament deformations for filament length* $L_f = 0.2$ *cm into various orbit classes with bending stiffness and* χ

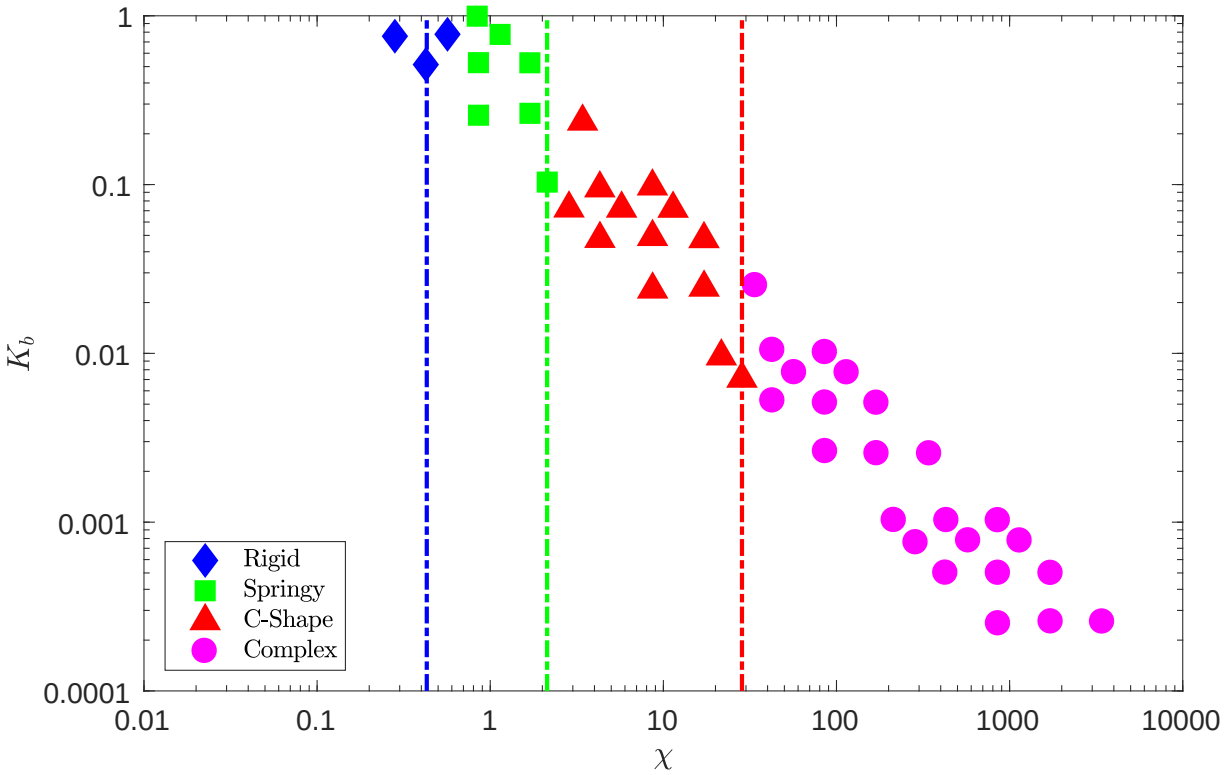

Figure 5.14: *Classification of flexible filament deformations for filament length* $L_f = 0.3$ *cm into various orbit classes with bending stiffness and* χ

5.2.4 ANN prediction

The parametric study in Section 5.2.3.2 was carried out to study the effects of filament length, shear rate and bending rigidity on filament orbit regimes and confirmed that the nondimensionalised flexibility measure χ is a descriptive measure of filament flexibility and classification. In this section, a prediction model using ANN is developed to effectively forecast the orbit regime of a filament for a wide range of parametric variables, using as data the results from the simulations in subsection 5.2.3.2.

The open-source neural-network Python library Keras [69] was used for the implementation of the ANN, along with the Scikit-learn, the open-source Python library for data analysis [70]. A total of 144 simulation data with the proposed modified IBM

were used in the ANN classification model, with the input variables being the filament length, shear rate and bending rigidity of the filament, and the output variable being the orbit regime of the filament. The orbit regimes are the same as those in the parametric study 5.2.3.2, 4 classes in total - Rigid, Springy, C-shape and Complex. The entire data were divided into training data and testing data - 80% of the simulation data is used for training and 20% is used for testing. The input variables were normalized with the MinMaxScaler in Equation (5.6) [70] which scales and translates each feature individually such that it falls in the given range of the training set, e.g. between zero and one. The transformation is given by

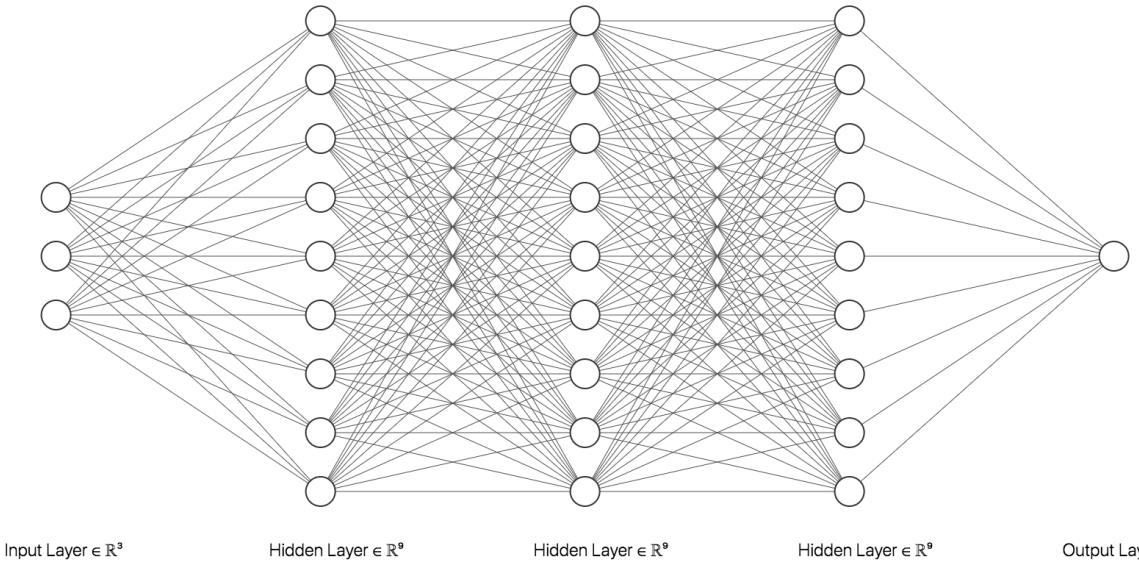

Figure 5.15: *The multi-layer network architecture 3-[9]-1 for the present study. The multi-layer network consists of an input layer with three nodes corresponding to the three input variables, three hidden layers with nine nodes per layer, and an output layer with one node for the predicted orbit class.*

$$
\begin{aligned}
X^f_{std} &= \frac{X^f - \min(X^f)}{\max(X^f) - \min(X^f)}, \\
X^f_{scaled} &= X^f_{std} * (\max(X^f) - \min(X^f)) + \min(X^f),
\end{aligned} \tag{5.6}
$$

where X^f refers to each feature.

An optimized number of three hidden layers with nine nodes per layer was selected. The multi-layer network architecture is shown in Figure 5.15. The number of layers and the number of nodes in each layer are model hyperparameters that, in general, cannot be determined analytically. To configure the optimum number of layers

and nodes, a trial-and-error approach is used. Using a 10-fold cross validation [63], the optimum number of hidden layers and nodes was selected based on the metric of accuracy (Equation (3.22)), discussed in Section 3.4, between the sample data and trained network data. The accuracy metric seems to serve well the present study since the class labels are sufficiently balanced.

The ReLU function (Equation (3.8)) is used for the hidden layers and the softmax function (Equation (3.9)) is used for the output layer. The loss function for the optimization of the model was the categorical cross-entropy loss function, described in Section 3.3.3.

Figure 5.16 depicts the cross-entropy loss over epochs for the training and testing dataset, and Figure 5.17 shows the classification accuracy over epochs. An epoch refers to one cycle through the full training dataset [71]. One epoch means that each sample in the training dataset has had the opportunity to update the internal model parameters and the number of epochs is a hyperparameter that defines the number of times that the learning algorithm will work through the entire training dataset. The line plots for both cross-entropy and accuracy show good convergence behavior of the model, where the training process stops when cross-entropy loss gets close to zero.

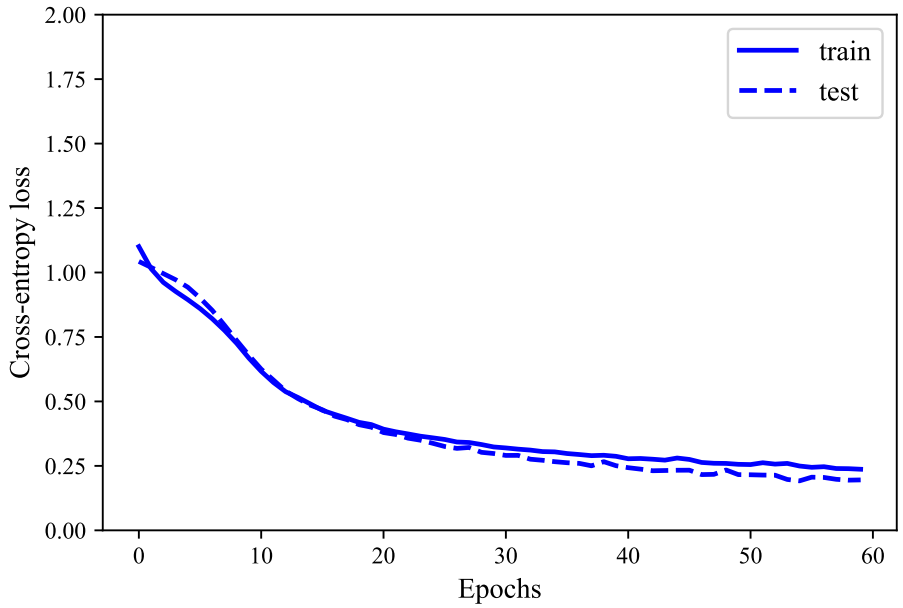

Figure 5.16: *Cross-entropy loss vs. epochs for the training and testing dataset*

In this case, it can be seen that the model performed well, achieving a classification accuracy of 91.3% on the training dataset and 93.1% on the test dataset. Since the performance for both the training and the testing datasets is very good, the ANN model shows no sign of overfitting or underfitting. Using a larger dataset is always better, however in order to increase the dataset, a large number of simulation

results with the modified IBM would be necessary, which increases significantly the computational cost.

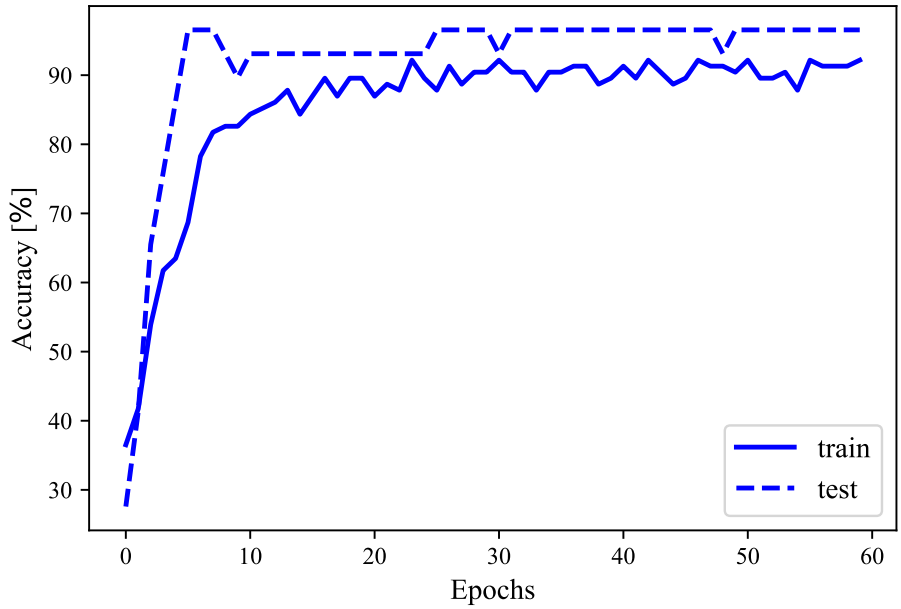

Figure 5.17: *Accuracy over epochs for the training and testing dataset*

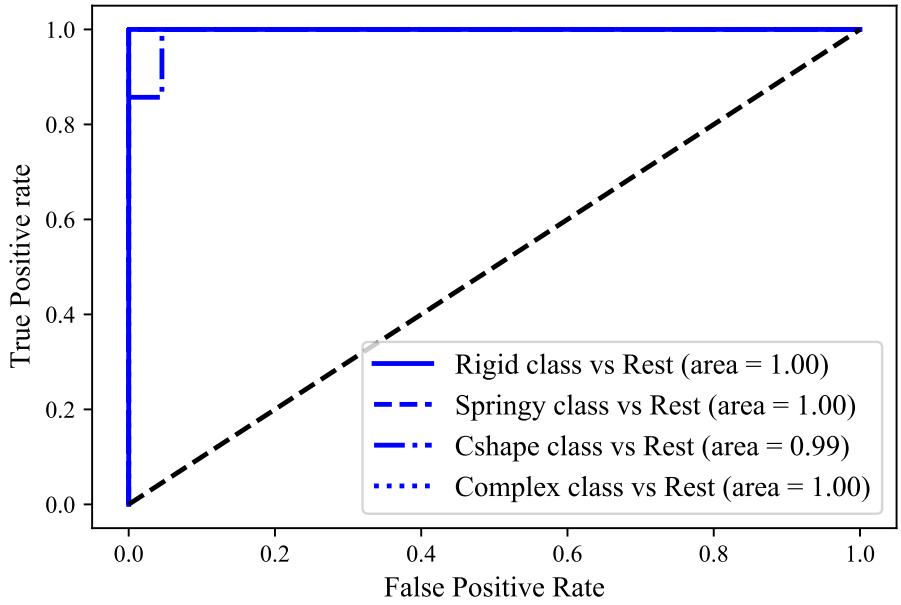

Figure 5.18: *ROC curves on the testing dataset and AUC values. The ROC curves overlap for almost all the cases since almost perfect classification is achieved. The black dashed line corresponds to the base case of a random classifier (see Section 3.4 and Figure 3.6).*

To evaluate further the prediction accuracy of the ANN classification model, the ROC curve and AUC, both discussed in Section 3.4, are used. As seen in Figure 5.18, the proposed ANN model gives excellent prediction on the testing dataset, indicating that the ANN configuration in Figure 5.15 can be effectively used to predict the orbit regimes of filaments in shear flow considering a wide range of input parameters.

5.3 Mechanical behavior of the actin cortex

The actin filaments are semiflexible polymers that interact with the surrounding cytoplasmic fluid through bending and stretching and undergo thermal fluctuations due to their small size scale. The purpose of this section is to investigate the mechanical properties of actin cortex, the partially cross-linked network of actin filaments frequently found near the periphery of cell, through numerical simulations, which could potentially provide more insight into fundamental phenomena.

5.3.1 Single filament

The actin cortex, the network of entangled, branched, and/or cross-linked actin filaments, as shown in Figure 5.19, is often the principal determinant of cell elasticity and mechanical stability. In order to understand these complex structures, quantitative models are employed for the structure, interactions, and mechanical response of the formed networks.

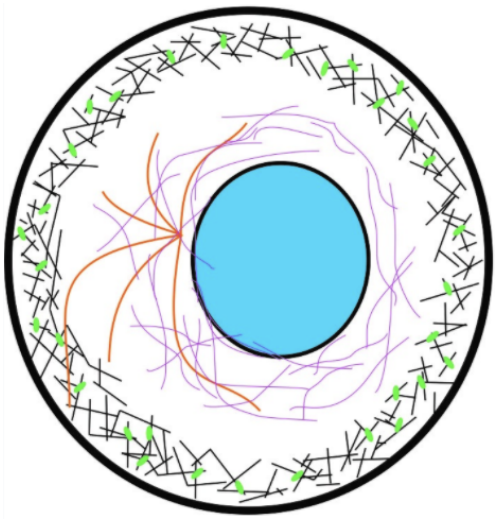

Figure 5.19: *Actin cortex in the eukaryotic cell [72], located next to the cell periphery*

This section focuses on the response of a single filament and aims to verify through numerical simulations the theoretical values obtained in Section 2.4. The biopolymers that comprise the cytoskeleton consist of aggregates of large globular proteins that are bound together rather weakly, as compared with most synthetic, covalently bonded polymers. Nevertheless, they can be surprisingly strong, due to their relatively large diameter, which makes their bending rigidity the most basic aspect determining their mechanical behavior on the cellular scale. Even with this mechanical resistance to bending, however, cytoskeletal filaments can still exhibit significant thermally induced bending fluctuations because of Brownian motion in the surrounding fluid.

As already discussed in Section 2.4, the persistence length is defined as $l_p = \frac{2\kappa_b}{k_B T}$. Actin filaments, due to their relatively large bending stiffness, have long persistence length compared to their total contour length, which basically means that the an actin filament in thermal equilibrium in a fluid will appear rather straight. In Section 2.4, the ensemble averaged contraction $< \Delta L >$ of an inextensible filament relative to its full contour length in the presence of thermal fluctuations was derived in Equations (2.84) and (2.85).

In this section, simulations of an inextensible filament immersed in a fluid domain with thermal noise were conducted in order to verify that, after a sufficient amount of time, the obtained averaged contraction $< \Delta L >_t$ of the filament approaches the theoretical value derived in Section 2.4.

The inextensible filament is modeled by means of the CGM, described in Section 4.3. The filament has contour length of $L = 5$ μm (typical lengths range from 100 nm to a few microns [73]) and is initially straight and fixed at one end, as shown in the Figure 2.6. Its bending rigidity is taken equal to $\kappa_b = 10^{-19}$ Nm. The filament is immersed in a fluid domain which has temperature of $T = 300$ K, dynamic viscosity $\mu = 0.001$ Pa $\cdot$ s, and fluid density $\rho = 1000$ kg/m^3, since cytosol is composed mainly of water. The fluid domain is of size 10^{-5} μm $\times$ 10^{-5} μm and solved using the Navier-Stokes equations derived in Section 2.2.3 and periodic boundary conditions. For the computations, a time step $\Delta t = 10^{-5}$ s is used. The filament is discretized by 10 linear elements, while the fluid domain is discretized with 40×40 Q2-Q1 (Taylor-Hood) elements. In order to solve for the fluid-structure interaction system, the algorithm described in Section 4.2.4 was employed, with only Step 2 being modified, in order to account for the inextensibility of the filament using the CGM, described in Section 4.3.

Figure 5.20 depicts the results of the simulation described above. The ensemble averaged contraction $< \Delta L >_t$ is plotted as a function of the number of time steps. It can be concluded from the plot that after around $6 * 10^6$ time steps, $< \Delta L >_t$ converges to the theoretical value according to the formula of Equation (2.85), which gives $< \Delta L >_{theoretical} \doteq 3.45 * 10^{-13}$. The one obtained from the simulations converges to the value of $3.31 * 10^{-13}$, which deviates only $\frac{<\Delta L>_{theoretical} - <\Delta L>_t}{<\Delta L>_{theoretical}} = 4\%$ from the theoretical one. Therefore, given the agreement of the simulation results with the

theoretical values, this comparison may serve as validation of the algorithm used in this study to simulate the fluid-structure interaction of the immersed filaments under thermal fluctuations.

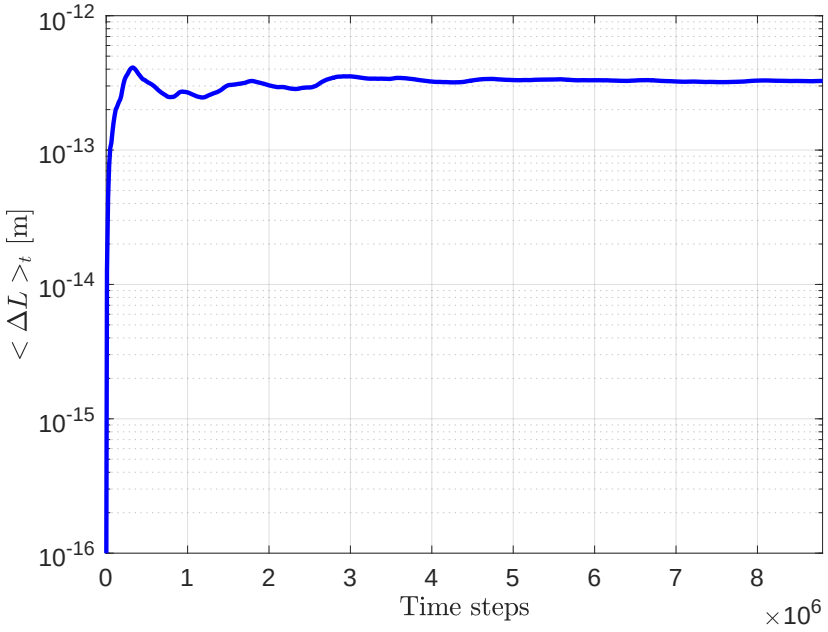

Figure 5.20: *Time average (log scale) of inextensible filament's contraction* $< \Delta L >_t$ *as a function of time steps under thermal fluctuations*

5.3.2 Mechanical behavior of Actin Cortex under simple shear

In this section, the elasticity of the actin cortex when subjected to shear is studied. More specifically, the observation of strain stiffening supported by previous numerical studies is further investigated. In the herein study, the surrounding, thermally fluctuating, cytoplasmic fluid is modeled, with the immersed actin filaments and the fluid constituting a two-way coupled mechanical system by means of the extended IBM, described in Section 4.2.

A two-dimensional model of a cross-linked network of actin filaments immersed in a thermally fluctuating fluid is considered, as shown in Figure 5.21. The network is generated by placing filaments of length L at uniformly random positions into a square cell of dimension W at uniformly random orientations. The filaments are modeled as elastic rods characterized by the equations of Section 2.4.1 and each filament is discretized by 10 linear finite elements. The stretching and bending stiffness of the filaments, as well as the rest of parameters, are summarized in Table 5.2. Representative values for the diameter of F-actin filaments and its Young's Modulus were used according to [74]. The fluid domain is of size $4 * 10^{-5}$ μm $\times$ $4 * 10^{-5}$ μm and solved using the Navier-Stokes equations derived in Section 2.2.3. A steady velocity in the

x-direction is applied at the top boundary of the fluid domain to induce shear flow, while the velocity at the bottom boundary is set equal to zero in both directions, and proper periodic boundary conditions are applied to the right and left boundaries. The fluid domain has temperature of $T = 300$ K, dynamic viscosity $\mu = 0.001$ Pa $\cdot$ s, and fluid density $\rho = 1000$ kg/m^3, since cytosol is composed mainly of water, and it is discretized using 64×64 Q2-Q1 (Taylor-Hood) elements. The algorithm described in Section 4.2.4 was employed in order to solve the fluid-structure interaction system, with a time step $\Delta t = 10^{-6}$ s, which is constrained to be one order of magnitude smaller than the time step used in Section 5.3.1 due to the existence of stiff cross links in the filament network.

Symbol	Name	Values
L	Contour length of actin filament	10 μm
E	Young's Modulus of actin filament	10^9 Pa
d	Cross-sectional diameter of actin filament	6 nm
k_s	Stretching stiffness of actin filament	$2.8 \cdot 10^{-8}$ N
k_b	Bending stiffness of actin filament	$6.4 \cdot 10^{-26}$ Nm
$\bar{\rho}$	Line density of actin filament network	13
W	Side length of square fluid domain	40 μm
κ_B	Boltzmann constant	$1.38 * 10^{-23}$ J/K
T	Temperature	300 K

Table 5.2: *Parameter values*

The filaments are undulated in the initial configuration and their shape is consistent with a thermal distribution of 10 transverse normal modes of the type $b_n \sin(\frac{n\,x\pi}{L})$, where the amplitudes b_n follow a normal distribution with zero mean and standard deviation $\sqrt{\frac{2}{l_p\,L}}\left(\frac{L}{n\pi}\right)^2$, where l_p is the persistence length, given in Table 5.2. The points were filaments overlap in the initial configuration are considered to be cross-links. In the calculations, the cross-links are assumed to be stiff, so that both rotation

and the displacement of the two filaments at the cross-link are equal. The cross-links are also assumed to be permanent, so that cross-links alterations are not considered.

The density of the network is characterized by the line density ρ, *i.e.*, the total length of filaments in the unit divided by the cell area, which is defined as $\rho = \frac{NL}{W^2}$, where N is the number of filaments and L the contour length of each filament. The dimensionless density is defined as $\bar{\rho} = \rho L$. In the calculations, a density of $\bar{\rho} = 13$ is used (representative for actin microfilaments), which is well above the percolation threshold of $\bar{\rho} = 5.7$ [23]. Figure 5.21 shows an example of a randomly generated network of density $\bar{\rho} = 13$ in its initial configuration.

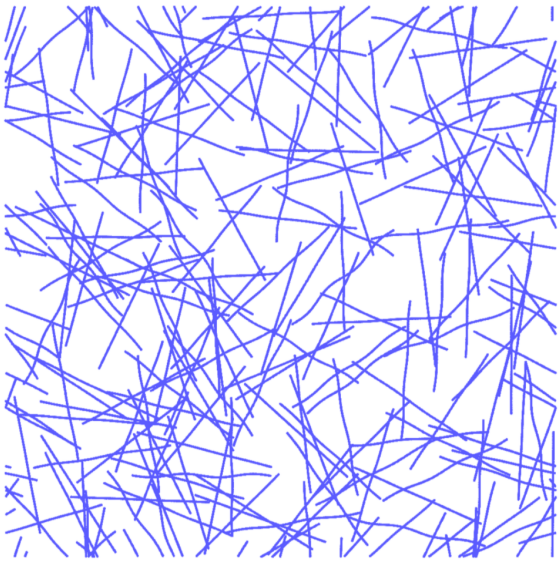

Figure 5.21: *Network configuration of undulated actin filaments with* $\bar{\rho} = 13$

The term unit cell will be used from now on in this study to describe the two-dimensional system of actin cortex immersed in the thermally fluctuating cytoplasmic fluid. The average shear stress of the unit cell is calculated by using the homogenization method described in Section 2.3 and (2.60). The results for a network of filaments with $\bar{\rho} = 13$, as shown in Figure 5.21, are shown in Figure 5.22, where the average shear stress $\bar{\tau}$ of the unit cell is plotted against the strain γ. A gradual decrease in the average shear stress of the system is observed initially as the actin filaments start to rearrange under the shear flow, all the way up to the point that the filaments get stabilized in orientation. After that point, the actin filaments start to enlogate, and therefore, to contribute with their stretching stiffness to the increase of the average shear stress of the system, thus observing a stiffening of the system at increasing strain.

Figure 5.23 shows the homogenized dynamic viscosity of the unit cell against the strain γ. Initially, the dynamic viscosity is equal to the viscosity of the cytoplasmic fluid, $\mu = 0.001$ Pa $\cdot$ s, and starts to gradually decrease while the actin filaments

rearrange under the shear flow. Once eventually the actin network get to a more stable configuration, the homogenized dynamic viscosity of the system starts to increase, until it gets twice the dynamic viscosity of the cytoplasmic fluid.

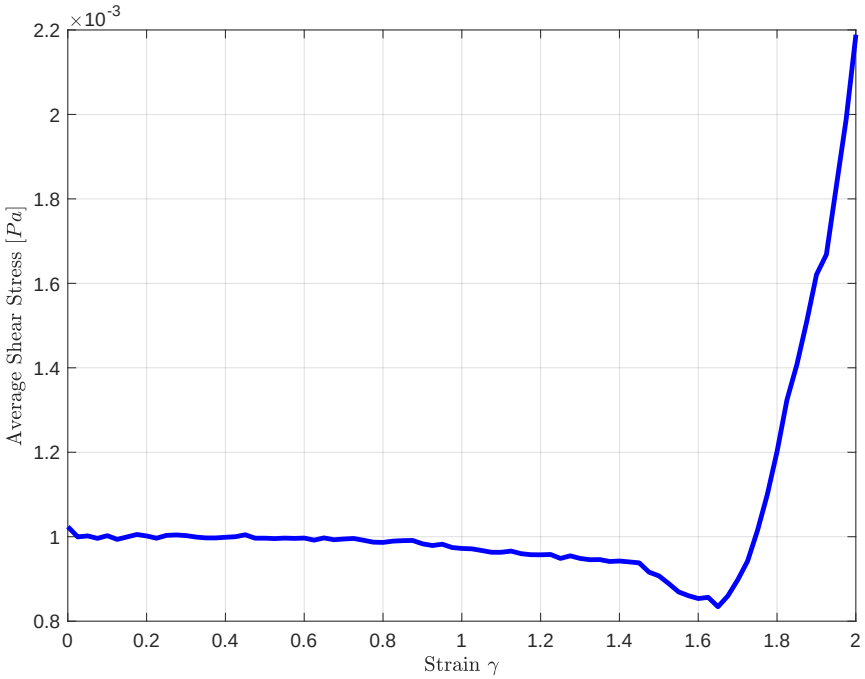

Figure 5.22: *Average shear stress $\bar{\tau}$ versus strain γ for the unit cell*

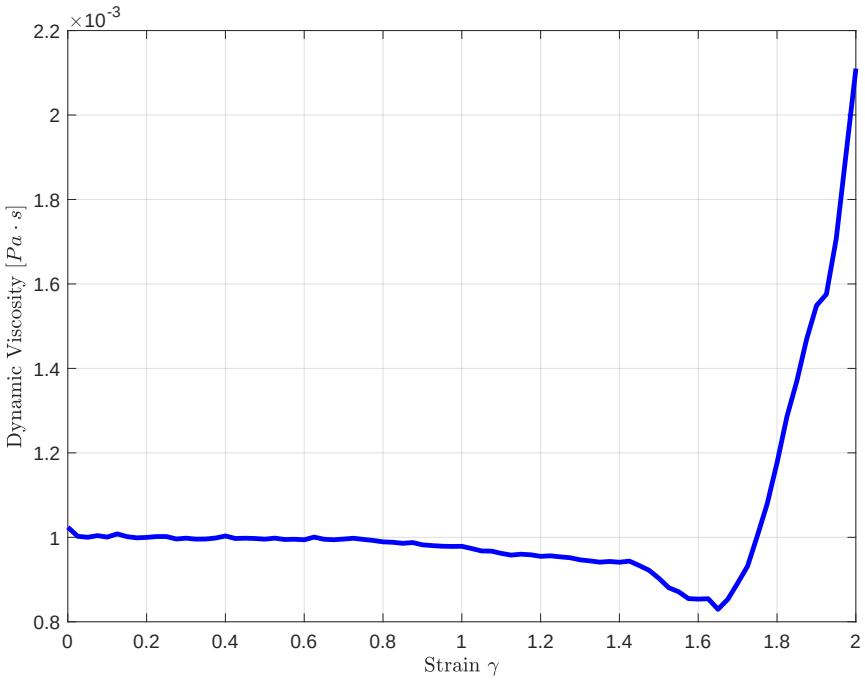

Figure 5.23: *Dynamic viscosity μ versus strain γ for the unit cell*

The change of length in filaments at various locations in the unit cell is shown in Figures 5.24 and 5.25. Some of the actin filaments initially get compressed as they rotate in order to rearrange under the shear flow and then start to enlogate.

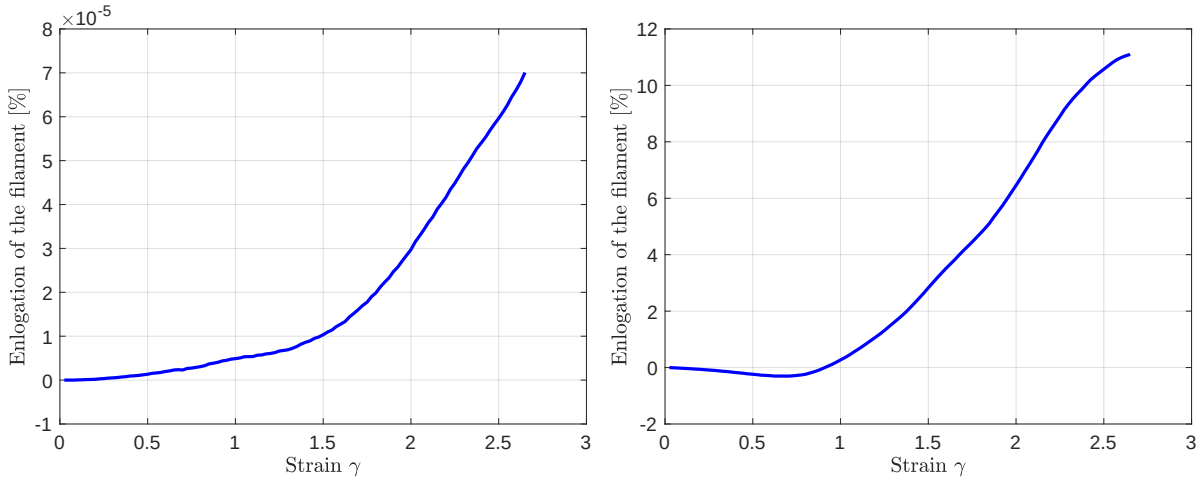

Figure 5.24: *Change of length in filaments versus strain γ at various positions*

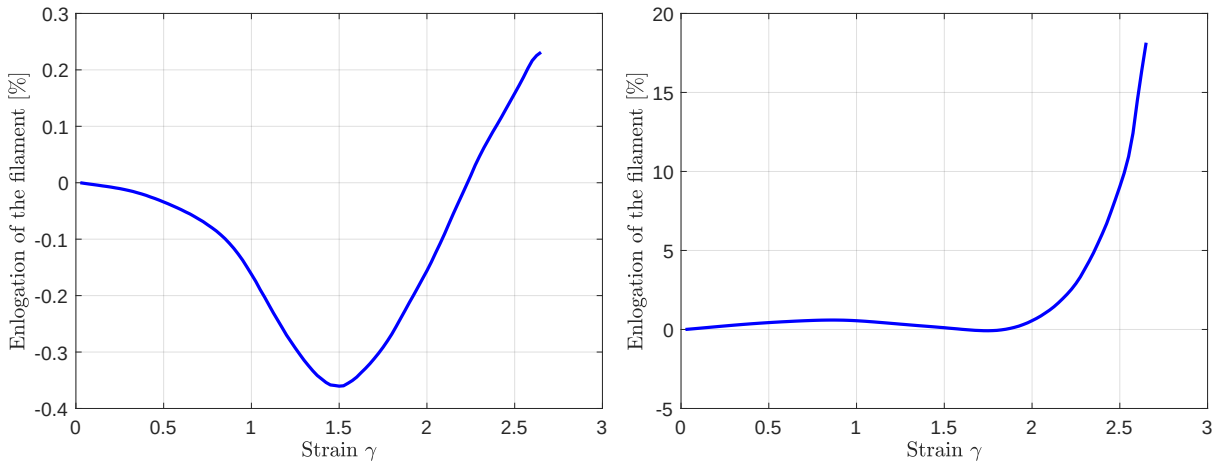

Figure 5.25: *Change of length in filaments versus strain γ at various positions*

The computations were repeated for the same configuration of actin network as in Figure 5.21 but this time with the filaments initially straight instead of undulated.

The results of the homogenized dynamic viscosity μ against the strain γ are shown in Figure 5.26, together with the results of the undulated actin network for comparison. It is clear from the plot that the homogenized dynamic viscosity is almost identical for the two cases, with only a slightly earlier increase in the homogenized dynamic viscosity for the case of straight actin filaments, once the filaments reach a more stable orientation under the shear flow. This observation is as expected since as the filaments started straight instead of undulated, they get to contribute slightly earlier with their stretching stiffness to the increase of the dynamic viscosity of the system.

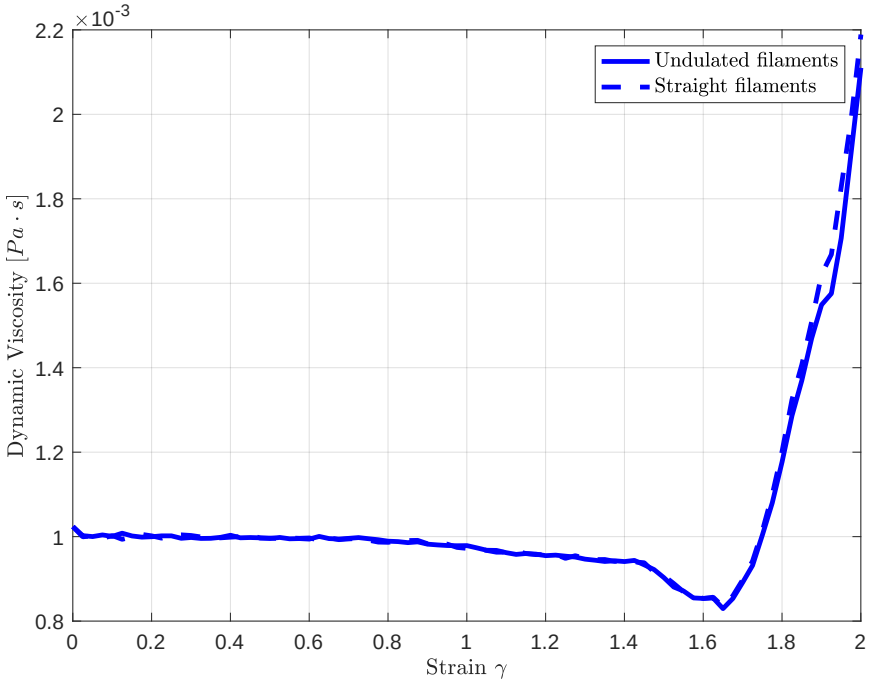

Figure 5.26: *Dynamic viscosity μ versus strain γ for the unit cell for straight and undulated actin filaments*

As stated earlier, the actin filaments in the actin cortex form cross-links by actin-binding proteins, Figure 5.27. The degree of cross-linking in the final network is dependent on the density of cross-linkers, as well as the way filaments interact with each other and the thermal noise. The existence of cross-links and their density are major determinants of cortical mechanics and experimental, as well as theoretical and numerical studies have shown that cross-linked biopolymer networks, when subjected to shear, stiffen at increasing strain. In order to further study the role of the cross-links in the actin cortex, the above computations were repeated for the same network configuration, as in Figure 5.21, but this time without the formation of cross-links between actin filaments that overlap. The results are shown in Figure 5.28, where a slight softening of the system can be observed in contradiction to the stiffening observed when the actin filaments are cross-linked.

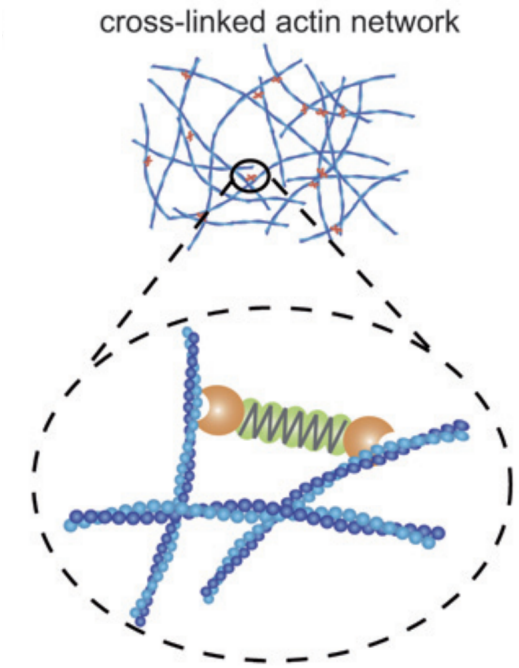

Figure 5.27: *Cross-links formed in the actin cortex [75]*

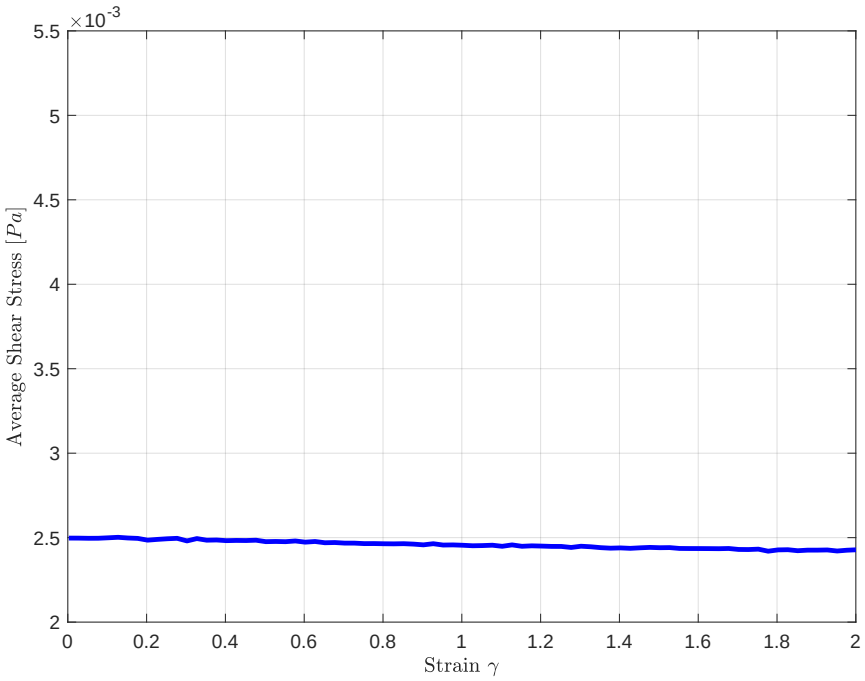

Figure 5.28: *Average stress $\bar{\tau}$ versus strain γ for the unit cell without cross-links*

In order to highlight the importance of the orientation of the actin filaments in the actin cortex, two extreme cases were considered, one configuration where the actin filaments are horizontal and another, where the actin filaments are vertical, forming cross-links when overlap in both cases. For the horizontal configuration, Figure 5.29 (left), the results are plotted in Figure 5.29 (right), where one may observe that the there is absolutely no stiffening in increasing strain as expected. However, for the vertical configuration, Figure 5.30 (left), there is a slight softening at increasing strain as it is depicted in Figure 5.30 (right). Although not plotted here, it is expected to have a stiffening starting appearing at a significantly larger strain, however the stiffening takes much longer to start compared to the case where the initial orientation of the actin filaments is uniformly distributed.

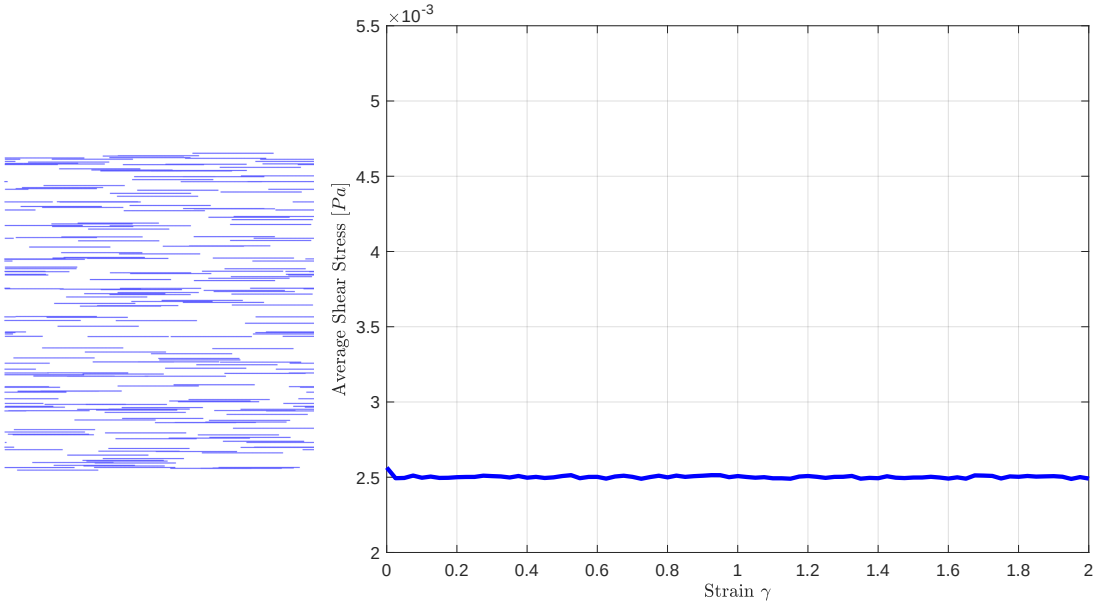

Figure 5.29: *Average stress $\bar{\tau}$ versus strain γ (right) for the unit cell with actin filaments positioned horizontally, and the corresponding configuration of the network (left)*

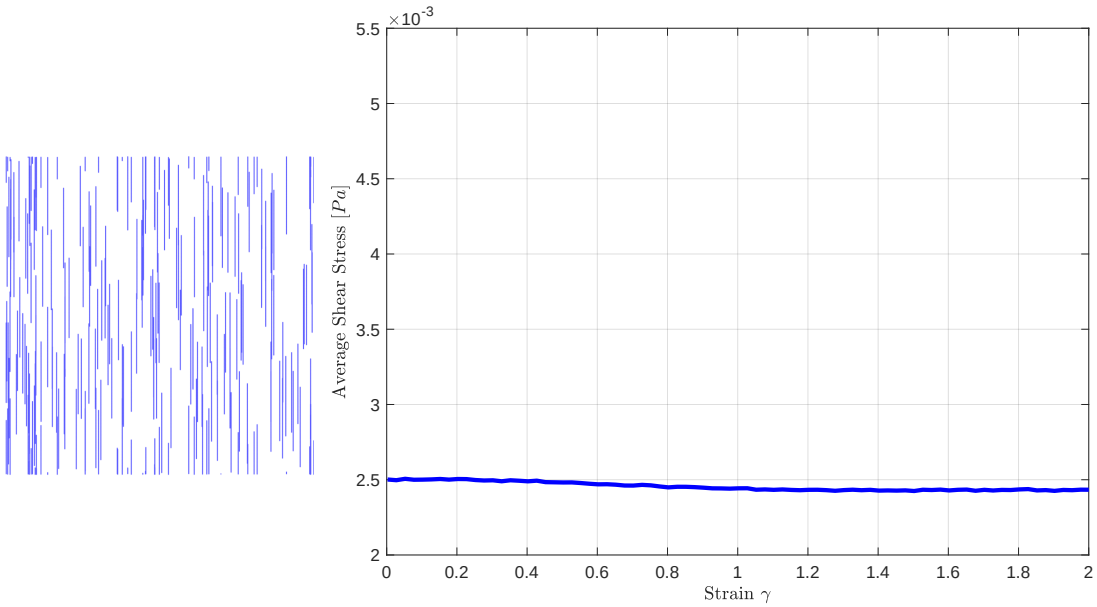

Figure 5.30: *Average stress $\bar{\tau}$ versus strain γ (right) for the unit cell with actin filaments positioned vertically, and the corresponding configuration of the network (left)*

5.3.3 Interactions between protein filaments under thermal fluctuations

Elastic, autonomous active filaments that interact with each other to achieve cooperation underlie many critical functions in biology and have been the subject of several recent theoretical and computational studies in order to investigate the coupling-induced synchronization in systems of active filaments [76–78]. However, the interaction between passive actin filaments under hydrodynamic thermal fluctuations and the corresponding fiber conformity remains to be investigated and it is the focus of this section. The behavior and motion of one filament with respect to other neighboring filaments is the subject of this section so as to get a better understanding of the underlying physical behavior of the filament-filament interaction for passive F-actin filaments under hydrodynamic thermal fluctuations.

Five filaments are considered in this study. They are placed side by side and assumed to be immersed in cytosol, which is a thermally fluctuating flow of low-Reynolds number. The goal is to analyze their deformation and mutual interaction. In this direction, a two-dimensional numerical simulation is carried out. The behavior of five flexible filaments placed freely in a thermally fluctuating fluid domain with

periodic boundary conditions is studied, as depicted in Figure 5.31.

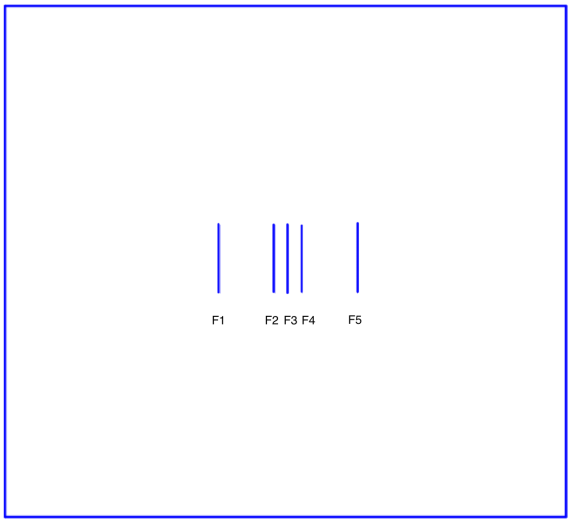

Figure 5.31: *Five flexible filaments placed freely in a thermally fluctuating fluid domain with periodic boundary conditions*

The fluid domain has dynamic viscosity $\mu = 0.001$ Pa·s, density $\rho = 1000$ kg/m^3, temperature $T = 300$ K, and size 10^{-4} m $\times$ 10^{-4} m. Periodic boundary conditions are applied on the fluid domain and it is solved using the Navier-Stokes equations derived in Section 2.2.3. For the computations, a time step $\Delta t = 10^{-6}$ s is used. Each of the five filaments is of length $L = 10$ μm and discretized by 20 linear elements, while the fluid domain is discretized with 64×64 Q2-Q1 (Taylor-Hood) elements. In order to solve for the fluid-structure interaction system, the algorithm described in Section 4.2.4 was employed. The stretching and bending stiffness of the filaments, as well as the rest of parameters, are summarized in Table 5.2.

The spacing between the filaments is considered to be $0.8 * L - 0.2 * L - 0.2 * L - 0.8 * L$, where L is the initial contour length of the filaments. The time-averaged relative change of distance between various combinations of filaments is plotted in Figures 5.32 - 5.34. The distance between two filaments is computed by averaging the distance of five points in total on each of the filaments. Each of the three plots focuses on a different filament and the time-averaged relative change of distance with the nearest and the farthest filament to the filament of focus are plotted. It can be observed that the filaments tend to spread out. The uneven spacing between the filaments seems to have no effect since, as shown in Figures 5.32 - 5.34, the filaments tend to spread out uniformly with the two curves depicted in each of the plots being very close. However, the spreadout trend, which is of order of around 0.80%, is not very significant, at least for the number of time steps that the calculations were

carried out (approximately $6 * 10^6$ time steps).

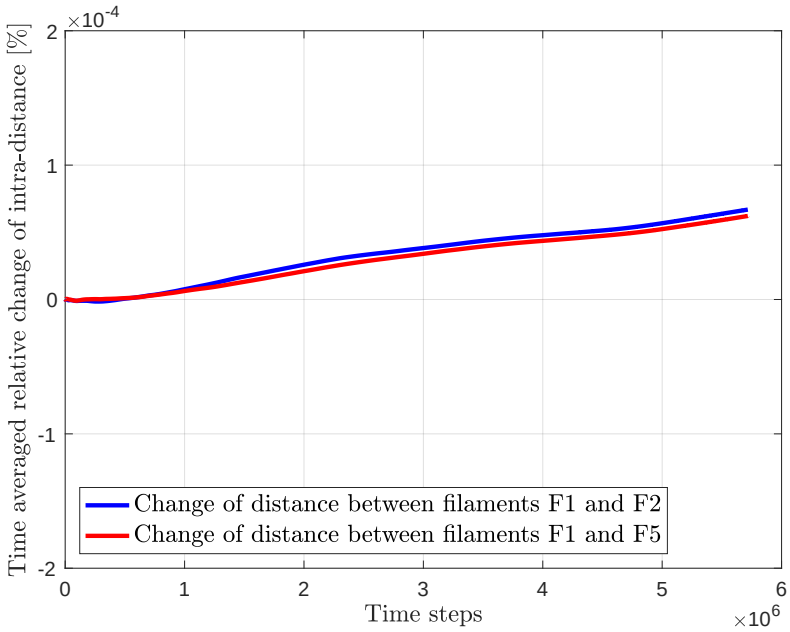

Figure 5.32: *Time-averaged relative change in distance between filament F1 and filaments F2 and F5*

The time-averaged relative change of length $< \Delta L >$, defined as the time-averaged change of the end to end distance of points in a filament, is shown in Figure 5.35. It can be observed that some of the filaments tend to extend and some tend to contract. To further examine if there is any correlations in the observed behavior of $< \Delta L >$, the correlation coefficients among the $< \Delta L >$ of the filaments were calculated. Figure 5.36 plots the $< \Delta L >$ along with the correlation coefficients for the most correlated filaments, which seem to be filaments F2, F3 and F5.

From the obtained results, it seems that the filaments in a thermally fluctuating flow, where a two-way interaction between filaments and fluid is considered, tend to spread out and some of them tend to extend or contract in highly correlated manner. However, further investigation is needed on the topic, which could be part of a future study.

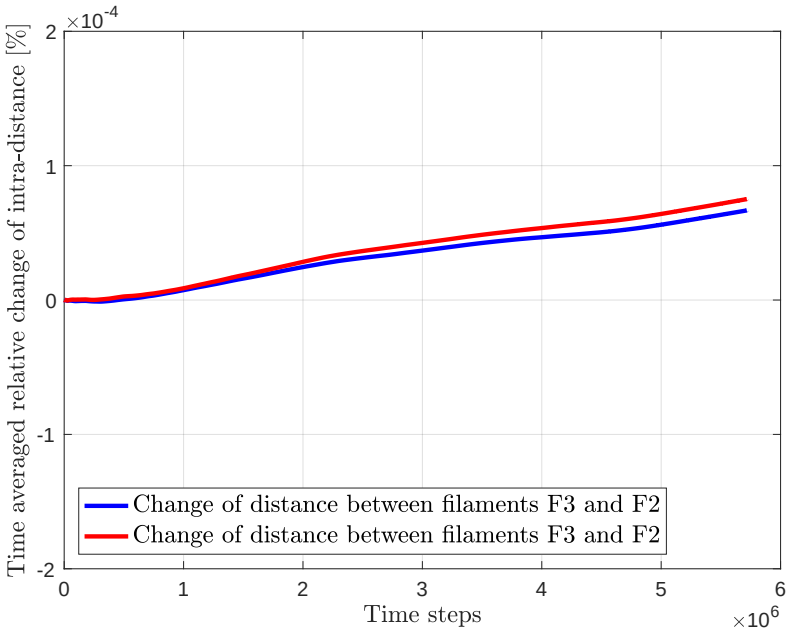

Figure 5.33: *Time-averaged relative change in distance between filament F3 and filaments F2 and F4*

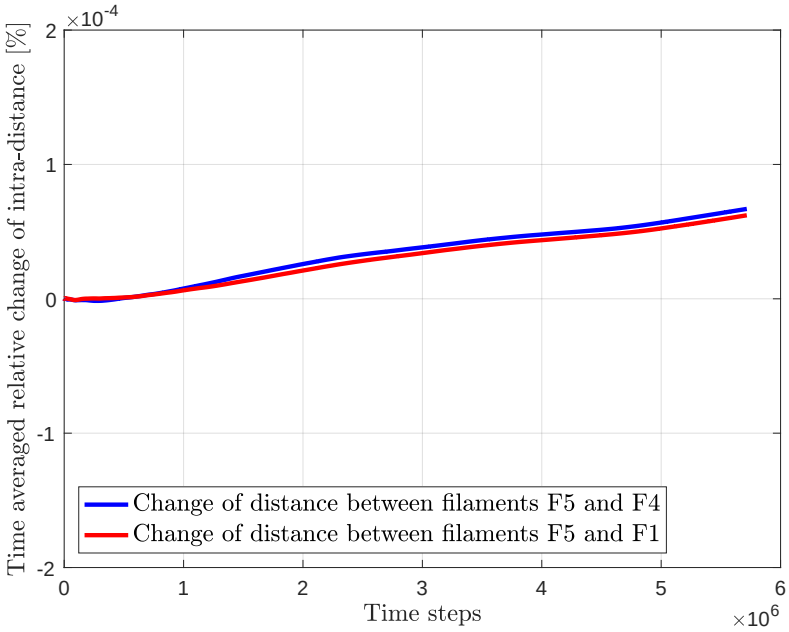

Figure 5.34: *Time-averaged relative change in distance between filament F5 and filaments F1 and F4*

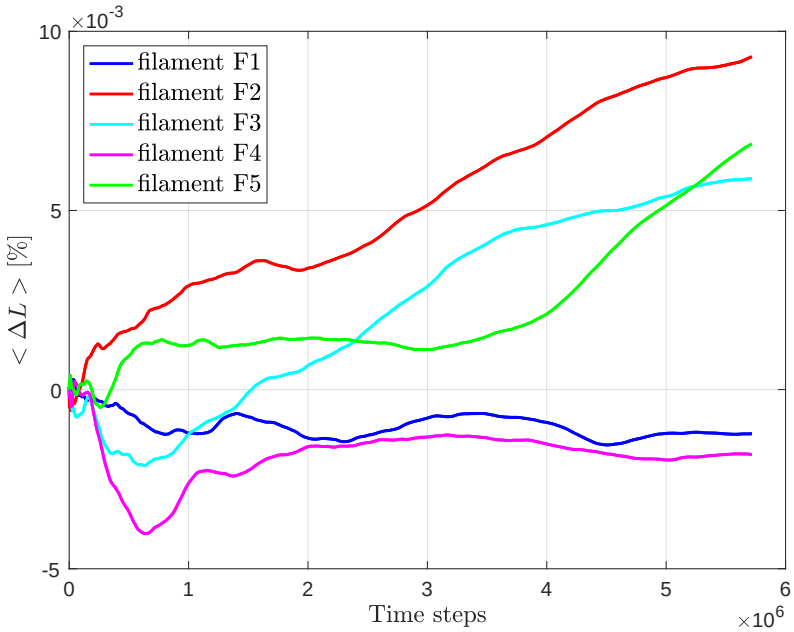

Figure 5.35: *Time-averaged relative change of length of the filaments*

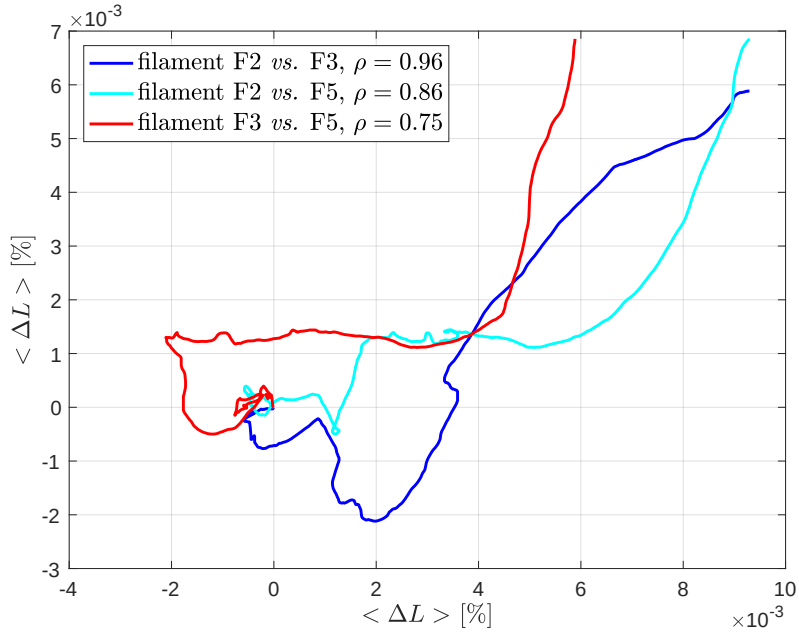

Figure 5.36: *Time-averaged relative change of length and correlation coefficients of filaments F2, F3, and F5*

5.4 Concluding Remarks

In this chapter the methods discussed in Chapter 4 were applied in order to investigate the orbit regime of flexible filaments in shear flow in and the mechanical behavior of the actin cortex. The first part focused on the implementation of a two-dimensional numerical model based on a combination of IBM and CGM in order to capture the hydrodynamic interaction of filaments in viscous shear flow while strictly enforcing the filament inextensibility condition, without restricting the time step required in contrast to the regular IBM. The results of the modified IBM simulations were first validated and then used to develop prediction models based on ANN, in order to predict the two-dimensional orbit classes for flexible filaments placed in shear flow with different parameters.

The second part focused on the mechanical behavior of the actin cortex. The response of a single inextensible filament using the proposed numerical algorithms was studied in order to verify the theoretical values for time-averaged contraction under thermal fluctuations. Furthermore, the mechanical behavior and elasticity of the actin cortex when subjected to shear was investigated, illustrating a stiffening of the cross-linked network with increasing strain under shear flow. Lastly, the behavior and motion of passive F-actin filaments under hydrodynamic thermal fluctuations was studied, showing filaments with the trend to spread out under thermal fluctuations and two-way coupling with the fluid.

Chapter 6

Conclusion

In this dissertation, two numerical algorithms based on the Immersed Boundary Method (IBM) are proposed and implemented for the study of the actin cortex and semiflexible filaments immersed in low-Reynolds flows, where a two-way coupling for the underlying fluid-structure interaction problem is considered. Specifically, a new, modified, version of the IBM that combines the Coarse-Graining Method with IBM and is more computationally efficient than the traditional IBM is developed for modeling inextensible filaments in shear flow at low Reynolds numbers. The method was implemented to study the various two-dimensional orbit regimes of flexible filaments. The results of the proposed method were validated quantitatively and qualitatively with theoretical results and previous studies (numerical and experimental), showing excellent agreement. They were then used to develop a prediction model with Artificial Neural Networks (ANN) to effectively forecast the orbit regime of a filament in shear flow with different parameters. The results from the proposed ANN configuration showed that it can be effectively used to predict the orbit regimes of filaments in shear flow considering a wide range of input parameters.

An extension of the traditional IBM to include a stochastic stress tensor is also proposed for modeling the thermal fluctuations in the cytoplasmic fluid surrounding the actin cortex. The mechanical behavior of a massless, inextensible, and semiflexible filament immersed in a thermally fluctuating fluid was investigated with the proposed numerical scheme. The resulting time-averaged contraction of the filament compares very favorably to the theoretical value for the ensemble average of the same quantity, as obtained from the Worm-like Chain model. On the basis of this analysis, the proposed hybrid algorithm appears to be both robust and accurate, and could offer a reliable means for investigating the combined effect of multiple (and possibly interacting) filaments in low-Reynolds number flows. The mechanical behavior of the actin cortex and its elasticity when subjected to shear flow, without neglecting the presence of thermally fluctuating cytoplasmic fluid, has been investigated, illustrating a stiffening of the cross-linked network with increasing strain under shear flow, as other experimental and numerical studies have shown. By implementing the pro-

posed extension of the IBM, the behavior, interaction, and motion of passive F-actin filaments under hydrodynamic thermal fluctuations was also studied, where a trend of filaments spreading out was observed.

Based on the results and progress of the work of this dissertation, there are several topics of future research to be recommended. The two proposed numerical algorithms can be extended for dealing with three-dimensional domains. Furthermore, they can be further extended to account for two-dimensional immersed boundaries, as in [79]. In the investigation of the mechanical behavior of the actin cortex, the effects of dynamic cross-links should be incorporated in future studies, as well as the presence and effect of motor proteins. Lastly, additional work is required for the study of the behavior and interaction of passive F-actin filaments under hydrodynamic thermal fluctuations so as to further investigate the observed trends of the current study.

Bibliography

[1] Boal, D. H. *Mechanics of the cell*, Cambridge: Cambridge University Press, 2012.

[2] Gardel, M. L., Kasza, K. E., Brangwynne, C. P., Liu, J., and Weitz, D. A. "Mechanical response of cytoskeletal networks", *Methods of Cell Biology*, vol. 89, pp. 4878-519, 2008.

[3] Huber, F., Schnaub, J., Ronicke, S.,Raccuh, P., Muller, K., Futterer, C., and Kas, J. "Emergent complexity of the cytoskeleton: from single filaments to tissue", *Advances in Physics*, vol. 62, no. 1, pp. 1-112, 2013.

[4] File:Actin-cortex.png., Wikimedia Commons, the free media repository, 2020, accessed May, 12 2020.

[5] Lodish, H., Kaiser, C., Krieger, M., Bretscher, A., Ploegh, H., Amon, A., and Scott, M. *Molecular Cell Biology, 7th Ed*, New York: W. H. Freeman and Co., 2013.

[6] Jensen, M. H., Morris, E. J., Goldman, R. D., and Weitz, D. A. "Emergent properties of composite semiflexible biopolymer networks", *BioArchitecture*, vol. 4, no. 5, pp. 138-143, 2014.

[7] Morone, N., Fujiwara, T., Murase, K., Kasai, R. S., Ike, H., Yuasa, S., Usukura, J., and Kusumi, A.. "Three dimensional reconstruction of the membrane skeleton at the plasma membrane interface by electron tomography", *The Journal of Cell Biology*, vol. 174, no. 6, pp. 851-862, 2006.

[8] Ambriz, X., de Lanerolle, P., and Ambrosio, J. R.. "The mechanobiology of the actin cytoskeleton in stem cells during differentiation and Interaction with Biomaterials", *Stem Cells International*, vol. 10, no. 1, pp. 42-47, 2018.

[9] Bausch, A. R. and Kroy K. "A bottom-up approach to cell mechanics", *Nature Physics*, vol. 2, no. 4, pp. 231-238, 2016.

[10] MacKintosh, F. C. and Janmey, P. A. "Actin gels", *Current Opinion in Solid State and Materials Science*, vol. 2, no. 3, pp. 350-357, 1997.

[11] Kratky, O. and Porod, G. "Röntgenuntersuchung gelster gadenmolekle", *Recueil des Travaux Chimiques des Pays-Bas*, vol. 68, no. 12, pp. 1106-1122, 1949.

[12] Bustamante, C., Marko, J., Siggia, E., and Smith, S. "Entropic elasticity of *lambda*-Phage DNA", *Science*, vol. 265, no. 5178, pp. 1599-1600, 1994.

[13] Mitchison, T. J. and Cramer, L.P. "Actin-based cell motility and cell locomotion", *Cell*, vol. 84, no. 3, pp. 371-379, 1996.

[14] Carlier, M. F. and Pantaloni, D. "Control of actin dynamics in cell motility", *Journal of Molecular Biology*, vol. 269, no. 4, pp. 459-467, 1997.

[15] Orr, A. W., Helmke, B. P., Blackman, B. R., and Schwartz, M. A. "Mechanisms of mechanotransduction", *Developmental Cell*, vol. 10, no. 1, pp. 11-20, 2006.

[16] Schwartz, U. S. and Gardel, M. L. "United we stand - integrating the actin cytoskeleton and cell-matrix adhesions in cellular mechanotransduction", *Journal of Cell Science*, vol. 125, no. 13, pp. 3051-3060, 2012.

[17] Harris, A. R., Jreij, P., and Fletcher, D. A.. "Mechanotransduction by the actin cytoskeleton: converting mechanical stimuli into biochemical signals", *Annual Review of Biophysics*, vol. 47, no. 1, pp. 617-31, 2018.

[18] Du Roure, O., Lindner, A., Nazockdast, E., and Shelley, M. "Dynamics of flexible fibers in viscous flows and fluids", *Annual Review of Fluid Mechanics*, vol. 51, no. 1, pp. 539-572, 2019.

[19] Tseng, Y., An, M. K., Osingwe, E., and Wirtz, D. "The bimodal role of filamin in controlling the architecture and mechanics of F-actin networks", *Journal of Biological Chemistry*, vol. 279, no. 3, pp. 1819-1826, 2004.

[20] Storm, C., Pastore, J. J., MacKintosh, F. C., Lubensky, T. C., and Janmey, P. A. "Nonlinear elasticity in biological gels", *Nature*, vol. 435, no. 7039, pp. 191-194, 2005.

[21] Gardel, M. L., Shin, J. H., MacKintosh, F. C., Mahadevan, L., Matsudaira, P., and Weitz, D. A. "Elastic behavior of cross-linked and bundled actin networks", *Science*, vol. 304, no. 5675, pp. 1301-1305, 2004.

[22] Onck, P. R., Koeman, T., van Dillen, T., and van der Giessen, E. "Alternative explanation of stiffening in cross-linked semiflexible networks", *Physical Review Letters*, vol. 95, no. 17, p. 1788102, 2005.

[23] Wilhelm, J. and Frey, E. "Elasticity of stiff polymer networks", *Physical Review Letters*, vol. 91, no. 10, p. 108103, 2003.

[24] Bustamante, C., Bryant, Z., and Smith, S. "Ten years of tension: single-molecule DNA mechanics", *Nature*, vol. 421, no. 6921, pp. 423-427, 2003.

[25] Peters, J. P., Yelgaonkar, S. P., Srivatsan, S. G., Tor, Y., and Maher J. L. "Mechanical properties of DNA-like polymers", *Nucleic Acids Research*, vol. 41, no. 22, pp. 10593-10604, 2013.

[26] Gardel, M. L. "Synthetic polymers with biological rigidity", *Nature*, vol. 493, no. 7434, pp. 618-619, 2013.

[27] Kanchan, M. and Maniyeri, R. "Numerical analysis of the buckling and recuperation dynamics of flexible filament using an immersed boundary framework", *International Journal of Heat and Fluid Flow*, vol. 77, pp. 256-277, 2019.

[28] Jeffery, G. B. "The motion of ellipsoidal particles immersed in a viscous fluid",*Proceedings of the Royal Society A: Mathematical, Physical and Engineering Sciences*, vol. 102, no. 175, pp. 161-179, 1922.

[29] Forgacs, O. L. and Mason, S. G. "Particle motions in sheared suspensions: X. Orbits of flexible threadlike particles", *Journal of Colloid Science*, vol. 14, no. 5, pp. 473-491, 1959.

[30] Tornberg, A. K. and Shelley, M. J. "Simulating the dynamics and interactions of flexible fibers in Stokes flows", *Journal of Computational Physics*, vol. 196, no. 1, pp. 8-40, 2004.

[31] Yamamoto, S. and Matsuoka, T. "A method for dynamic simulation of rigid and flexible fibers in a flow field", *The Journal of Chemical Physics*, vol. 98, no. 1, pp. 644-650, 1993

[32] Peskin, C. S. "The Immersed Boundary Method", *Acta Numerica*, vol. 11, pp. 479-517, 2002.

[33] Stockie, J. M. "Simulating the dynamics of flexible wood pulp fibers in suspension", *Proceedings of the 16th Annual International Symposium on High Performance Computing Systems and Applications, IEEE Computer Society*, Atlanta, p. 154, 2002.

[34] Stockie, J. M. and Green, S. I. "Simulating the motion of flexible pulp fibers using the immersed boundary method", *Journal of Computational Physics*, vol. 147, no. 1, pp. 147-165, 1998.

[35] Wiens, J. K. and Stockie, J. M. "Simulating flexible fiber suspensions using a scalable immersed boundary algorithm", *Computer Methods in Applied Mechanics and Engineering*, vol. 290, pp. 1-18, 2015.

[36] Huang, W.X., Shin, S.J., and Sung, H.J. "Simulation of flexible filaments in a uniform flow by the immersed boundary method", *The Journal of Chemical Physics*, vol. 226, no. 2, pp. 2206-2228, 2007.

[37] Moreau, C., Giraldi, L., and Gadêlha, H. "The asymptotic coarse-graining formulation of slender-rods, bio-filaments and flagella", *Journal of the Royal Society Interface*, vol. 15, no. 144, 2018.

[38] Miyanawala, T. and Jaiman, R. "A hybrid data-driven deep learning technique for fluid-structure interaction", *Proceedings of the ASME 2019 38th International Conference on Ocean, Offshore and Arctic Engineering*, vol. 2, 2019.

[39] Koh, J. B.Y., Shen, X., and Marcos. "Supervised learning to predict sperm sorting by magnetophoresis", *Magnetochemistry* , vol. 4, no. 3, p. 31, 2018.

[40] Fayed, M., Elhadary, M., Ait Abderrahmane, H., and Zakher B.N. "The ability of forecasting flapping frequency of flexible filament by artificial neural network", *Alexandria Engineering Journal*, vol. 58, no. 4, pp. 1367-1374, 2019.

[41] Kanchan, M. and Maniyeri, R. "Numerical simulation and prediction model development of multiple flexible filaments in viscous shear flow using immersed boundary method and artificial neural network techniques", *The Japan Society of Fluid Mechanics and IOP Publishing Ltd*, vol. 52, 2020.

[42] Gurtin, M. E. *An lntroduction to Continuum Mechanicsc*, New York: Acacdemic Press, 1981.

[43] Papadopoulos, P.. "Course Notes", *Introduction to continuum Mechanics, ME185*, University of California, Berkeley, 2020.

[44] Landau, L. D. and Lifshitz, E. M. *Fluid Mechanics, Second Edition: Volume 6 (Course of Theoretical Physics)*, Oxford: Butterworth-Heinemann, 1987.

[45] Mandadapu, K. K., Arkaprabha S., and Papadopoulos, P. "A homogenization method for thermomechanical continua using extensive physical quantities", *Proceedings of the Royal Society A: Mathematical, Physical and Engineering Sciences*, vol. 468, no. 2142, pp. 1696-1715, 2012.

[46] Spakowitz, A. J. and Wang, Z. G. "Free expansion of elastic filaments", *Physical review. E, Statistical, nonlinear, and soft matter physics*, vol. 64, no. 6, pp. 61-80, 2001.

[47] Reif, F.. *Fundamentals of statistical and thermal physics*, New York: McGraw-Hill Book Company, 1965.

[48] Chandler, D. *Introduction to Modern Statistical Mechanics*, New York: Oxford University Press, 1987.

[49] MacKintosh, F. C. "Polymer-Based Models of Cytoskeletal Networks", *Cytoskeletal Mechanics*, pp. 152-169, 2006.

[50] Irving, J. H. and Kirkwood, J. G. "The statistical mechanical theory of transport processes. IV. The equations of hydrodynamics", *J. Chem. Phys.*, vol. 18, pp. 817-829, 1950.

[51] Papadopoulos, P. "Course Notes", *Finite Element Methods in Nonlinear Continua, ME280B*, University of California, Berkeley, 2016.

[52] Singh, A. K. and Bhadauria, B. S. "Finite difference formulae for unequal sub-intervals using Lagrange's interpolation formula", *International Journal of Mathematical Analysis*, vol. 3, no. 17-20, pp. 815-827, 2009.

[53] Pandey, A., Hardt, S., Klar, A., and Tiwari, S. "Brownian dynamics of rigid particles in an incompressible fluctuating fluid by a meshfree method", *Computers & Fluids*, vol. 127, pp. 174-181, 2016.

[54] Usabiaga, F. B., Bell, J. B., Delgado-Buscalioni, R., Donev, A., Fai, T. G., Griffith, B. E., and Peskin, C. S. "Staggered schemes for fluctuating hydrodynamics", *SIAM Journal of Multiscale Modeling and Simulation*, vol. 10, no. 4, pp. 1369-1408, 2012.

[55] Español, P. "Stochastic differential equations for non-linear hydrodynamics", *Physica A-statistical Mechanics and Its Applications*, vol. 248, no. 1-2, pp. 77-96, 1998.

[56] Español, P., Anero, J. G., and Zúñiga, I. "Microscopic derivation of discrete hydrodynamics", *The Journal of Chemical Physics*, vol. 131, no. 24, pp. 1-15, 2009.

[57] Donev, A., Vanden-Eijnden, E. and Garcia, A., Bell, J. "On the accuracy of finite-volume schemes for fluctuating hydrodynamics", *Communiccations in Applied Mathematics and Computational Science*, vol. 5, no. 2, pp.149-197, 2010.

[58] Gray, L. and Hancock, J. "The propulsion of sea-urchin spermatozoa", *Journal of Experimental Biology*, vol. 32, no 4, pp. 802-814, 1955.

[59] Lighthill, J. "Flagellar hydrodynamics", *SIAM Review*, vol. 18, no. 2, pp. 161-230, 1976.

[60] Sahai, A. "Course Notes", *Introducction to Machine Learning, CS298A*, University of California, Berkeley, 2019.

[61] Thulasiraman, K., Swamy, M. N. S. *Graphs: Theory and Algorithms*, Hoboken, NJ: John Wiley and Son, 1992.

[62] Hornik, K. "Approximation capabilities of multilayer feedforward networks", *Neural Networks*, vol.4, no. 2, pp. 251-257, 1991.

[63] Hastie, T., Tibshirani, R., and Friedman, J. H. *The elements of statistical learning: Data mining, inference, and prediction*, New York, Springer, 2001.

[64] Bradley, A., "The use of the area under the ROC curve in the evaluation of machine learning algorithms", *Pattern Recognition*, vol. 30, no. 7, pp. 1145-1159, 1997.

[65] Thoma, M., https://en.wikipedia.org/wiki/File:Roc-draft-xkcd-style.svg, *Wikipedia*, 2018, accessed April, 2 2021.

[66] Arndt, D., Bangerth, W., Davydov, D., Heister, T., Heltai, L., Kronbichler, M., Maier, M., Pelteret, J.-P., Turcksin, B., and Wells, D. "The deal.II finite element library: Design, features, and insights", *Computers & Mathematics with Applications*, vol. 8, pp. 407-422, 2021.

[67] Anczurowski E. and Mason, S. G. "The kinetics of flowing dispersions. II. Equilibrium orientations of rods and discs (experimental)", *Journal of Colloid Science*, vol. 23, no. 4, p. 522-532, 1967.

[68] Stockie, J. M. "Analysis and computation of immersed boundaries, with application to pulp fibers", PhD thesis, Department of Mathematics, University of British Columbia,1997.

[69] Gulli, A., Pal, S. *Deep learning with Keras*, Birmingham: Packt Publishing, 2017.

[70] Pedregosa, F., Varoquaux, G., Gramfort, A., Michel, V., Thirion, B., Grisel, O., Blondel, M., Prettenhofer, P., Weiss, R., Dubourg, V., Vanderplas, J., Passos, A., Cournapeau, D., Brucher, M., Perrot, M., and Duchesnay, E. *et al.* "Scikit-learn: Machine Learning in Python", *The Journal of Machine Learning Research*, vol. 12, no. 85, pp. 2825-2830, 2011.

[71] Brownlee, J. *Deep Learning With Python*, Machine Learning Mastery, 2016.

[72] Website of research group of Professor Dr. Franziska Lautenschläger, http://www.lautenschlaeger.uni-saarland.de/Research.html, Saarland University.

[73] Podolski, J. L. and Steck, T. L. "Length distribution of F-actin in dictyostelium discoideum", *Journal of Biological Chemistry*, vol. 265, no. 3, pp. 1312-1318, 1990.

[74] Gardel, M. L., Kasza, K. E., Brangwynne, . P., Liu, J., and Weitz, D, A. "Mechanical response of cytoskeletal networks", *Methods in Cell Biology*, vol. 89, chapter 19, pp. 487-519, 2008.

[75] Lieleg, O., Claessens, M. M. A. E., and Bausch, A. R. "Structure and dynamics of cross-linked actin networks", *Soft matter*, vol. 6, no. 2, pp. 218-225, 2010.

[76] Fily, Y., Subramanian, P., Schneider, T. M., Chelakkot, R. and Gopinath, A. "Buckling instabilities and spatiotemporal dynamics of active elastic filaments", *The Royal Society Interface*, vol. 17, no. 165, p. 20190794, 2020.

[77] Chelakkot, R., Gopinath, A., Mahadevan, L., and Hagan, M. F. "Flagellar dynamics of a connected chain of active, polar, Brownian particles", *The Royal Society Interface*, vol. 11, no. 92, p. 20130884, 2014.

[78] Isele-Holder, R. E., Jager, J., Saggiorato, G., Elgeti J., and Gompper, G. "Dynamics of self-propelled filaments pushing a load", *Soft Matter*, vol. 12, no. 41, pp. 8495-8505, 2016.

[79] Boffi, D., Heltai, L., and Gastaldi, L. "The finite element immersed boundary method: Model, stability, and numerical results", *Mathematical Models and Methods in Applied Sciences*, vol. 17, no. 10, pp. 1479-1505, 2007.